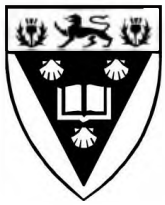

RHODES UNIVERSITY

Where Leaders Learn

A STRATIGRAPHIC, PETROGRAPHIC AND GEOCHEMICAL STUDY OF THE GAMAGARA FORMATION AT THE MAREMANE DOME, NORTHERN CAPE PROVINCE, SOUTH AFRICA

DAVID PATRICK COUSINS

Thesis submitted to the Department of Geology, Rhodes University in fulfilment of the requirements for the degree of

MASTER OF SCIENCE

January 2016

Supervised by Professor Harilaos Tsikos

Abstract

Between 80 and 90 percent of the potential iron ore reserves in the Griqualand West basin in the Northern Cape province of South Africa is situated in the Asbesheuwels Iron-formation immediately below an unconformity that separates it from the Gamagara Formation of the Olifantshoek Supergroup. This extensive regional unconformity marks a lengthy period of non-deposition and erosion which preceded the deposition of the Gamagara Formation. Due to the nature of the intimate relationship between the shales and iron ore body, specifically on the Maremane dome, new insights into the Gamagara Formation were required.

The thesis provides a renewed stratigraphic, petrographic and geochemical study on the Gamagara Formation and relates it to previous studies done on the lateral correlative Mapedi Formation, some 70 km north of the Maremane dome. The use of 10 newly available drill-cores selected from across the Maremane Dome allows for regional correlations to be made in a study which employs petrographic/mineralogical investigations using transmitted/reflected light microscopy, XRD and EPMA, complimented by traditional whole-rock geochemical analysis of majors, traces, rare earth elements and Nd isotopes.

At the base of the Gamagara lie conglomerates representing an alluvial fan deposit, overlying this, shale and quartzite successions represent progradational delta lobes. The deltas are interpreted to be tide-dominated as indicated by a combination of features including: microbial mat growth, intertidal deposition in the delta top, sand bars and flaser laminations in the upward coarsening quartzite units of the delta front. Transgression is indicated by periodic transgressive lag deposits.

A variety of sedimentary structures and textural features are described that can be interpreted as the results of microbial mat colonization on the sediment surface. Although in none of the described features can it irrefutably be proven that they are microbial mat deposits, the observed features are

consistent with such an interpretation and should be considered indicators of possible microbial mat presence in the Gamagara Formation.

Hydrothermal modifications are identified in various units of the Gamagara Formation and seem to occur as separate events. Basal white shales show mobility of Al and slight HFSE enrichments, while overlying red shales record HFSE, K and Fe enrichments. K-metasomatism has been known to occur in the underlying paleoweathering profile of the Transvaal Supergroup (Ongeluk lavas) a unit which is interpreted as the most likely provenance for the mid-to-upper shale lithofacies of the Gamagara Formation. Highly alkaline F-bearing brines had the ability to mobilize titania and fluorapatite, reset Nd isotope systematics and ultimately enriched HFSE concentrations in the red shales of the Gamagara Formation. As the same enrichment is evident in the Mapedi Formation, the event possibly represents unconformity related fluid flow on a regional scale (~140 km). Nd-isotopes record an isotopic disturbance concurrent with the HFSE enrichment and T_{DM} model ages suggest disruption (and enrichment) occurred between 1.73 and 1.86 Ga. Following this, Fe-addition occurred by epigenetic mechanisms similar to those of MVT-type deposits.

Although gaps in the current understanding of the modifications of the Gamagara Formation exist, such events may have far reaching implications for the underlying iron ore bodies and the possibility arises that the genesis and/or epigenetic modification of the ore bodies of the Transvaal Supergroup may be casually linked to the same fluid-migration event/s.

DECLARATION

I declare that this thesis is my own work, and information from other publications is adequately referenced. It is being submitted in fulfilment for the Master of Sciences degree in the Department of Geology, Rhodes University.

DAVID P. COUSINS

.....

ACKNOWLEDGEMENTS

To my supervisor and mentor - Professor Harilaos (Hari) Tsikos, for his continuous guidance, advice and scientific enlightenment. I am truly privileged to have gotten to know Hari on both a professional and personal level. His encouragement has permitted me to think freely and critically and greatly improved my role as a scientist, helping me on my path to future endeavours. Furthermore, without Hari's hard work, dedication and insight into the formation of the Postgraduate Research in Iron and Manganese Ore Resources group (PRIMOR), along with the generous financial support of ASSMANG Ltd., this project and many others (past, present and future) would not be possible. Hari is truly a great leader and exceptional asset to the Geology Department at Rhodes University.

Gratitude is extended to Marius Burger, Sakkie van Niekerk, Brian Nel, Lorraine Semenya and the geotechnical staff at Assmang, Khumani operations as well as to Michael Van Den Heever, Jacques Deacon and the geotechnical staff at Khumba Iron Ore, Sishen operations. Both companies provided incredible support both on-site and in the assistance of countless queries in the months that followed.

To Professor J.S. Marsh (XRF), Thapelo Moloto (EPMA) and Dr Jonathan Britton (XRD) for their laboratory assistance at Rhodes University. The use of Jeol JXA 8230 Superprobe at Rhodes University, sponsored by NRF/NEP grant 40113 (UID74464), is kindly acknowledged.

To Christel Tinguely (ICP-MS) and Dr Petrus Le Roux (MC ICP-MS) for their laboratory assistance at the University of Cape Town. To Dr Cynthia Sanchez-Garrido, for the XRF results obtained from Stellenbosch University following the decommissioning of RU's facility.

To Vuyokazi Nkayi, John Hepple, Andrea King, Andile 'Chris' Pikoli, Thulani Royi, and Nosipho Wakashe for their administrative and technical assistance at Rhodes University.

I am sincerely grateful to my family and to Camilla Kotzé, for the constant, solid and unconditional support provided during the development of this project. Lastly, to my friends/colleagues in the Geology department (a.k.a. the 'teaaaaaaaa' group) for sharing countless beverages, jokes and geological puns during my three years at Rhodes University. These times will never be forgotten and here's to many more in the future.

Table of Contents

1 INTRODUCTION

1.1. General

Minerals and rock types of the Northern Cape were first described by European explorers in the early 1800's and in 1874 the first geological journal publication of the Northern Cape was completed after extensive mapping expeditions were undertaken by G.W Stow (Cairncross & Beukes, 2013). By the 1920's, iron and manganese deposits had received much attention, resulting in the common practice of exploration and mining in the region. Today, following more than 90 years of mining, a sound understanding of the geology is required to further unlock these resources. Stratigraphic and structural relations between the Early Proterozoic Transvaal and Gamagara Sequences along the western margin of the Kaapvaal Craton in Griqualand West (Figure 1.1) were heavily debated since Stow first described the geology of the area (Beukes and Smit, 1987). The stratigraphic placement of such units were important not only for mining and exploration purposes, but also because of the implications the red-bed successions of the Gamagara had on the early evolution of Earths' atmosphere and hydrosphere.

The mid-to-late Paleoproterozoic successions of the Gamagara Formation outcrop along the Langeberg and Korannaberg mountain ranges and Matsap and Gamagara Hills on the Kaapvaal Craton in Griqualand West, Northern Cape Province, South Africa (Van Niekerk, 2006; Figure 1.2). The Gamagara Formation is made up of conglomerates, shales and quartzites deposited upon a regional unconformity, commonly referred to as the Gamagara/Mapedi unconformity (Figure 1.2). This unconformity marks a lengthy period of erosion into the underlying Transvaal Supergroup which today hosts the vast resources of manganese and iron in South Africa. Due to the nature of the intimate relationship between the shales and iron ore body, specifically on the Maremane dome, the Gamagara Formation has become central to this thesis

The Mapedi Formation, a lateral correlative of the Gamagara, occupies a similar lithostratigraphic position, however it lies in a geographically distinct area (Van Schalkwyk and Beukes, 1986; Beukes and Smit, 1987). The link between the two Formations are however poorly understood and the correlations are based largely on field and minor petrographic observations. Recent studies on the Mapedi Formation have revealed flaws in the original models of shale formation (Kalumbu, 2006; Land *et al.*, in review) and a greater understanding of the Gamagara Formation hopes to shed light on post-depositional processes which occurred in Paleoproterozoic crust. Such processes are important, specifically when they would have occurred proximal to large ore bodies essential to South Africa's wealth and prosperity.

This thesis provides new detailed studies of the Gamagara Formation using material from drill-cores obtained across the Maremane dome specifically where the unconformity transects the high-grade iron ore deposits. Stratigraphic, petrographic and geochemical data is collected to: a) produce renewed records of the stratigraphic sub-units of the Gamagara Formation across space; b) constrain the likely provenance characteristics of the sedimentary succession by means of petrographic and geochemical 'finger-printing' on all the individual sub-units; c) unravel the depositional and diagenetic history and further assess previous models of timing and mechanisms for the hematitic nature of the red beds', and; d) provide stratigraphic relations between the Gamagara strata and adjacent lithostratigraphic units in order to deconstruct the Transvaal and Olifantshoek successions where necessary.

1.2. Regional Geology

South Africa's Kaapvaal Craton is host to some of Earths most well-preserved Neoarchean to Palaeoproterozoic cover successions (~ 2.9 to 2.0 Ga). The most complete and least deformed succession is that of the Transvaal Supergroup (Table 1.1), a volcano-sedimentary succession spanning between approximately 2.65 – 2.05 Ga is preserved within three structural basins on the Kaapvaal Craton, namely the Transvaal and Griqualand West basins' in South Africa and the Kanye basin in Botswana (Kirschvink *et al.* 2000; Moore *et al.* 2001; Figure 1.1). The Transvaal basin circumscribes the 2.05 Ga Bushveld Complex in the east while the Griqualand West basin lies on the western margin of the Kaapvaal Craton bordering the Proterozoic Kheis orogenic belt (Figure 1.1) The basins are divided by a basement high known as the Vryburg rise (Figure 1.1; Moore *et al.*, 2001).

The Griqualand West basin is located in the Northern Cape province of South Africa and is defined by the Transvaal and (overlying) Olifantshoek Supergroup (Table 1.1). These Supergroups are divided by an extensive regional unconformity which marks a lengthy period of non-deposition and erosion. Above this major regional unconformity lie red bed shales which make up the basal units of the Olifantshoek Supergroup (Figure 1.2; Moen, 2006). These shale successions, known as the Gamagara and Mapedi Formations are the oldest red beds in the Griqualand West basin (Zimmermann *et al.*, 2008).

Two major deformational events affected the Griqualand West basin. The first period produced east-west directed folding and uplift on the Kaapvaal Craton (Cairncross & Beukes, 2013). This folding-event postdates the extrusion of the Ongeluk basaltic andesites but precedes the deposition of the Gamagara and Mapedi Formations'. The folding produced the Maremane dome (anticline) and associated Dimoten and Ongeluk-Witwater synclines (Figure 1.2; Grobbelaar *et al.*, 1995). The uplift and folding exposed much of the Transvaal Supergroup to erosion which is identified by the regional unconformity separating the Transvaal from the Olifantshoek Supergroup (Grobbelaar *et al.*, 1995).

The second major event included the deformation of the Kheis Belt, a north-south striking metamorphic belt which formed along the western margin of the Kaapvaal Craton (Figure 1.1; Da Silva, 2011). This event produced the Blackridge thrust (Figure 1.2) which duplicates the strata of the Olifantshoek Supergroup in certain areas of the Griqualand West basin (Grobbelaar et al, 1995).

The region hosting the Gamagara/Mapedi Formation has undergone low-grade metamorphism, with temperatures not exceeding ~170°C and pressures of less than 2 Kbar (Holland & Beukes, 1990). The gentle folding, uplift and subsequent erosion in the Griqualand West basin results in the Gamagara/Mapedi Formation to rest on a range of units of the Transvaal Supergroup, from close to its base on the carbonates of the Campbellrand Subgroup, to higher up in the succession on the iron formations of the Hotazel Formation (Figure 1.3).

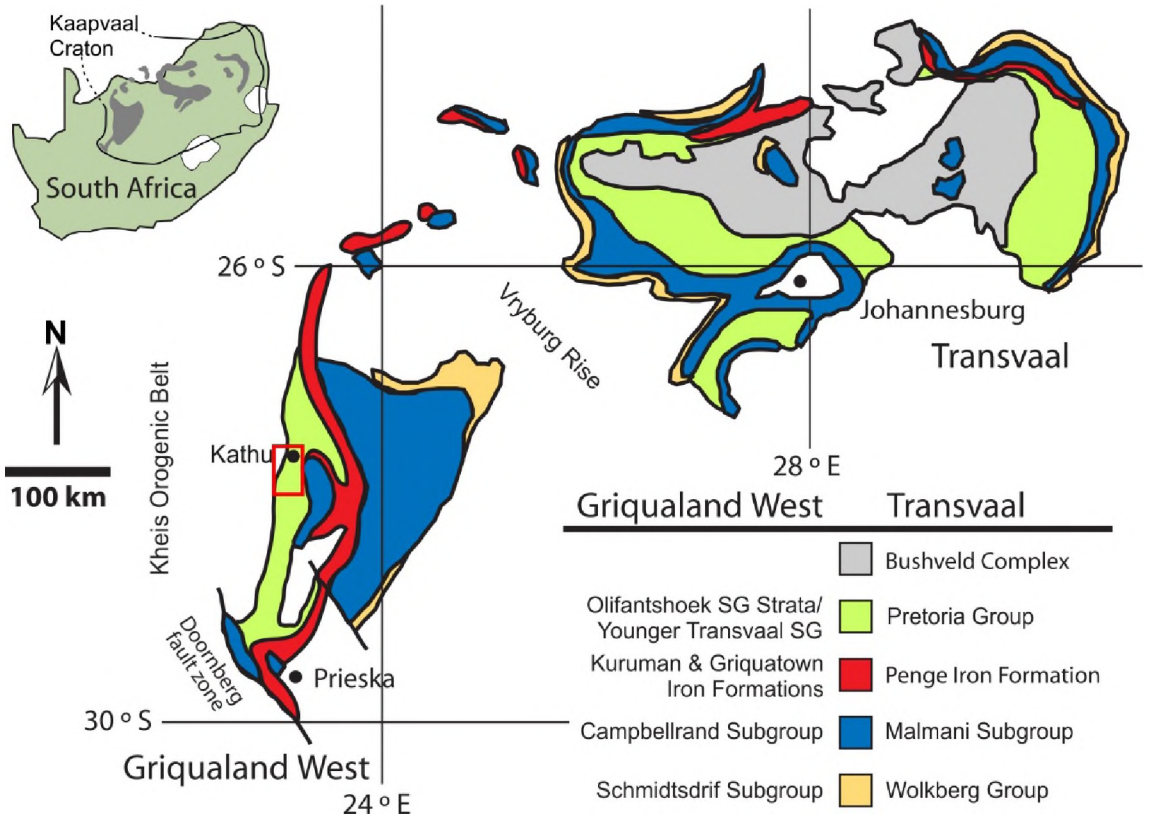

Figure 1.1: Transvaal Supergroup locality map displaying the two biggest basins (Transvaal and Griqualand West) in South Africa. The red box indicates approximate sampling site in the Olifantshoek Supergroup (modified after Sumner & Beukes, 2006).

1.3. Previous work

1.3.1. Stratigraphic Classification

Initial discussions on Griqualand West focussed mainly on the Gamagara Formation and how it became interbedded with Transvaal strata on the Maremane dome in the Sishen and Postmasburg area. Between 1929 and 1964, the recognition of a roughly north-south trending thrust belt which can be traced south of Postmasburg and north of Sishen into the Kalahari manganese field indicated duplication of the strata (Figure 1.2; Nel, 1929; Visser, 1944; Strauss, 1964). Furthermore, field evidence illustrated that the Gamagara strata is distinctly different from the Transvaal Supergroup sequences. Confusion arose in 1967 after deep exploration drilling took place at Sishen, leading a group of researchers to believe that no thrust faults were present and that the Gamagara formed part of the Transvaal Supergroup (De Villiers, 1967). After remapping, surface profiling and deep borehole stratigraphic profiling was done in the 1980's, the major thrust zone hypothesis was again supported (Beukes & Smit, 1987). Consequently, the Gamagara was correlated with the Mapedi Formation at the base of the Olifantshoek Supergroup (Beukes & Smit, 1987). Table 1.1 displays the currently accepted SACS (South African Committee for Stratigraphy) subdivisions for the Griqualand West basin.

Apart from the geological complexities that surround the stratigraphy in the Griqualand West basin, there is also much uncertainty surrounding the ages and lateral correlation with the Transvaal basin. In an attempt to correlate the Griqualand West basin with the Transvaal Basin, Dorland (1999) proposed that the red beds of the Gamagara and Mapedi are lateral equivalents of the Dwaalheuwel Formation in the Transvaal. The suggested correlation is based on the age of the Ongeluk lava at ~2.22 Ga (Table 1.1), an age which falls within error of the Hekpoort lavas in the Transvaal basin (Cornell *et al.*, 1996). This age, however, is in conflict with an age of ~2.394 Ga yielded by the Mooidraai rocks overlying the Hotazel Formation (Table 1.1; Bau *et al.*, 1999). Using this correlation, the Gamagara and Mapedi was placed into the Transvaal Supergroup rather than the younger overlying Olifantshoek Supergroup. Following this, after extensive mapping in the area, Van Niekerk (2006) recognised a prominent regional unconformity at the base of the Hartley Formation and placed the base of the Olifantshoek at this sequence boundary. Van Niekerk (2006) placed the Mapedi, Gamagara and Lucknow Formations into their own stratigraphic subdivision which he labelled the Elim Group of the Transvaal Supergroup. Subsequent detrital zircon age data by Da Silva (2011) found that the relabelled Elim Group is in fact not part of the Transvaal Supergroup and should be placed in the higher lying stratigraphy as previously specified by Beukes and Smit (1987). For the purpose of this thesis, stratigraphic subdivisions will be kept as they are official accepted by SACS as seen in Table 1.1.

Table 1.1: General stratigraphy of the Griqualand West Basin as accepted by SACS at the time of this study (modified after Eriksson *et al.*, 2006; Polteau *et al.*, 2006). Ages from [*1]Cornell *et al.*, 1996; [*2]Polteau *et al.*, 2006; [*3]Bau *et al.*, 1999. Note the discrepancy between the Ongeluk and Mooidraai ages.

Supergroup	Group	Subgroup	Formation	Lithology	Approx. thickness (m)
Olifantshoek	Volop	Brulsand	Vuilnek & Vryboom	Quartzite, conglomerate	no info
			Top Dog	Quartzite, shale	600
			Verwater	Quartzite, hematite nodules, conglomerate	300
		Matsap	Glen Lyon	Quartzite, conglomerate	700
			Ellie's Rust	Quartzite, conglomerate	700
			Fuller	Quartz-wacke, conglomerate	2300
			Hartley & Bogoeberg Dam (1.928 Ga)[*1]	Basalt & tuff, quartzite & conglomerate	760 (SACS)
			Lucknow	Quartzite, shale, dolomite, conglomerate	500
			Iapedi & Gamagara (Doornfontein conglon	Hematite-pebble conglomerate, shale, quartzite, bas	~1000
Transvaal	Postmasburg	Voëlwater	Mooidraai (2.394 Ga)[*3]	Carbonate, chert	300
			Hotazel	BIF's, Mn	250
			Ongeluk (2.22 Ga)[*1]	Andesitic lava	900
			Makganyene	Diamictite	50-100
	Ghaap	Koegas (2.415 Ga)[*2]	Rooinekke	BIF's, dolomite	100
			Naragas	Shales, siltstones	240-600
			Kwakwas	Riebeckitic slate	
			Doradale	BIF	
			Pannetjie	Quartz-wacke, shale	
		Asbesheuwels	riquatown (Manganore Iron Fm) (2.432 Ga)	Clastic-texture BIF's	200-300
			Curuman (Wolhaarkop breccia) (2.557 Ga)[*1]	Microbanded BIF's	150-750
		Campbellrand (2.642 Ga)[*2]	Gamohaan	Carbonate, shale and chert	1500 - 1700
			Kogelbeen		
			Klippan		
			Papkuil		
			Klipfonteinheuwel		
			Fairfield		
			Reivilo		
			Monteville		
		Schmidtsrif		Shale, quartzite, lava, carbonate	10 - 250

1.3.2. The Maremane Dome

The Maremane dome is defined by the carbonate rocks of the Campbellrand Subgroup and iron-formations of the Asbesheuwels Subgroup. It dips gently at less than 10° in an arc to the north, east, and south (Figure 1.2; Van Schalkwyk and Beukes, 1986; Beukes and Smit, 1987). The Beeshoek, King, Bruce and Sishen iron ore deposits are situated on the Maremane dome in ancient karstic collapse structures developed in the carbonates of the Campbellrand (Figure 1.3). These sinkholes developed after an extended period of exposure and continental weathering which preceded the deposition of the shales of the Gamagara Formation.

In the karstic structures, a siliceous chert breccia, informally known as the Wolhaarkop breccia, marks a dissolution surface between the carbonates and the overlying slumped Asbesheuwels iron-formation (IF; Beukes *et al.*, 2003). At the contact with the Wolhaarkop, the distorted Asbesheuwels IF has been informally labelled the Manganore IF and outliers of this couplet define a broken arc along the east-central part of the Maremane dome (Figure 1.2; Van Schalkwyk and Beukes, 1986). The iron ore body

is generally found along the contact between the Manganore IF and overlying Gamagara Formation (Figure 1.3). Detrital ores are thought to be derived from erosion of underlying laminated ores and concentrated in the lower portion of the Gamagara Formation. This unit, informally known as the Doornfontein conglomerates, are often mined as part of the ore-body if they meet grade (Van Schalkwyk and Beukes, 1986; Beukes and Smit, 1987; Gutzmer and Beukes, 1998; Beukes *et al.*, 2003). Above the Doornfontein conglomerate lie thick accumulations of Al-rich shales, overlain by transgressive quartzites interbedded with red, white, black and green shales. The Doornfontein conglomerates and latter mentioned units make up the Gamagara Formation.

1.3.3. Ore Genesis Models

All high-grade iron ore deposits hosted in banded iron formation (BIF) form by the secondary enrichment of iron in the host rock. Such enrichment can take place in the supergene environment, through hydrothermal activity or by a combination of the two processes (Beukes *et al.*, 2003). In all types of deposits it would appear if the main factor of enrichment is though removal of silica (chert) from the BIF host rock, replacement of silica by iron-oxide minerals (such as hematite and/or magnetite) or a combination of the two processes. It is difficult to distinguish between the different genetic types of BIF hosted iron ores due to mineralogical and geochemical similarities in all types (Gutzmer *et al.*, 2008). It has been suggested that one of the simplest ways to distinguish between the various genetic types is through their broad geological setting (Beukes *et al.*, 2003).

The formation of high-grade iron ore on the Maremane dome has been attributed to the processes of supergene enrichment of the Asbesheuwels iron-formation by numerous authors (Van schalkwyk & Beukes, 1986; Beukes *et al.*, 2003; Gutzmer *et al.*, 2008). The high-grade ores are unconformably overlain by the aforementioned Doornfontein conglomerates which, when forming part of the ore body, contain hard laminated ore pebbles suggested to be derived from the underlying ores of the Manganore IF. Supergene ores are, however, typically very friable to soft saprolitic in character, leading to questions surrounding the provenance of the hard, well-rounded ore pebbles in the conglomerates (Van Deventer, 2009). Typically, the genesis of hard iron ores involve processes where hydrothermal fluids upgrade BIF and examples of such conglomeratic ore are present in India, where ore pebbles are derived from underlying hard hydrothermal ore bodies (Van Deventer, 2009). Hydrothermal fluid-rock interactions have been suggested to play a major role in the genesis of iron and manganese deposits in the Hotazel Formation of the Griqualand West basin (Tsikos *et al.*, 2003). Further support of hydrothermal activity in the region are found in the highly altered unconformity bound shales of the

Mapedi Formation, where mobilization of high field strength elements are evident (Land *et al.*, in review).

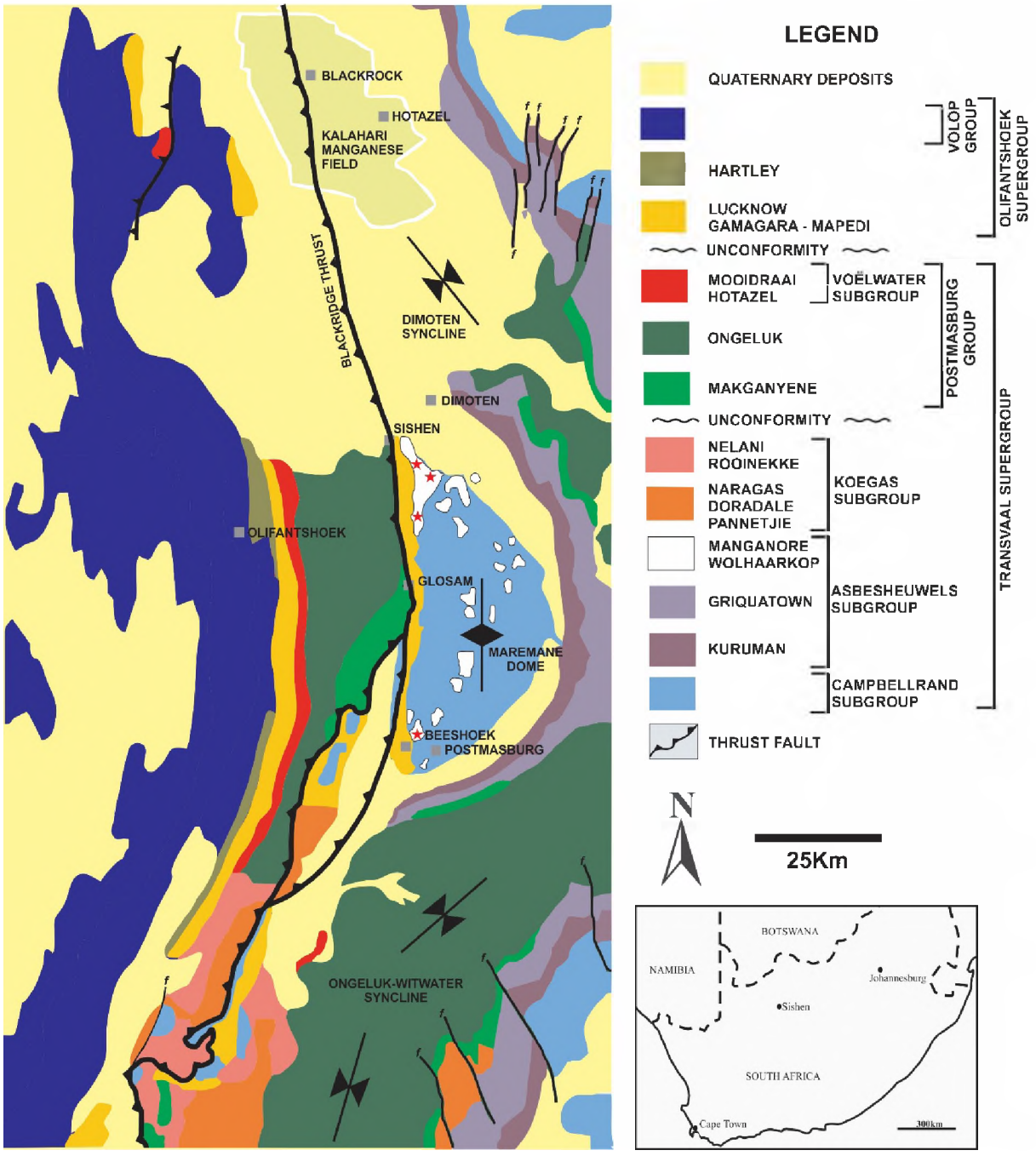

Figure 1.2: Geological map showing the stratigraphic setting of the Transvaal Supergroup and overlying Olifantshoek Supergroup in Griqualand West. Note the structural duplication of the Gamagara-Mapedi and Lucknow formations due to the westerly dipping thrust faults. The red stars indicate approximate sampling sites. Sishen co-ordinates lie 27°44'16"S 23°00'00"E (modified after Assmang, 2005).

1.3.4. Gamagara Formation

The type locality for the Gamagara Formation is on the Maremane dome where it is exposed in the ancient karstic sinkholes (Figure 1.3). Through exploration diamond drill core and pit-face mapping at Sishen completed in the 1980's, a composite stratigraphic model of the Gamagara Formation was developed by Van Schalkwyk and Beukes (1986). The sequence was informally labelled into separate Members reflecting the different lithofacies as follows:

a) **The Doornfontein Conglomerate Member**: It marks the base of the Gamagara Formation and is lenticular along strike. Where it is well developed, it consists of stacked upward-fining conglomerate → gritstone → shale sedimentary cycles. Iron pebbles decrease upwards in the sequence so that upper conglomerates consist of poorly sorted, angular to rounded chert and BIF pebbles. Interbedding of shales with the gritstones and conglomerates are typically reddish brown and sporadically contain hematite pisoliths. The shale units associated with iron-rich conglomerate and gritstones near the base of the Doornfontein may also be hematite-rich, forming part of the ore body. Interbedded red, white and black coloured shales overlie the conglomerates with impersistent thicknesses and lithologies along strike due to thinning and pinching over palaeohighs along the Gamagara unconformity. Highly aluminous white shale beds are developed along contacts between red and black shales.

b) **The Sishen Shale Member**: A red and cream-coloured shale overlie the Doornfontein and grade upwards into lenticular siltstones and shales. These are overlain by wavy and flaser-bedded siltstone and eventually into a dark purple, fine grained ferruginous quartzite. Rounded hematite ore, iron-formation and sand grains are present in the quartzite. The ferruginous quartzite is overlain with sharp contact by a thin (few centimetres thick) persistent gritstone, containing-well rounded granules of hematite, iron-formation, chert, and quartz and caps an upward-coarsening sedimentary sequence. A second upward-coarsening sedimentary sequence overlies the gritstone with sharp contact and another red and cream banded shale unit is developed grading upwards into the next unit.

c) **The Marthaspoort Quartzite Member**: The Sishen shale grades upwards through wavy and flaser-bedded quartzites and shales into a medium-to-coarse-grained, light purple and white quartzite. A gritty coarse-grained quartzite often overlies this on a scoured surface along which a small-pebble conglomerate, containing iron ore and iron-formation pebbles, may be developed.

d) **Paling Shale Member**: A sharp contact separates the Marthaspoort Member with red, cream and green coloured shales.

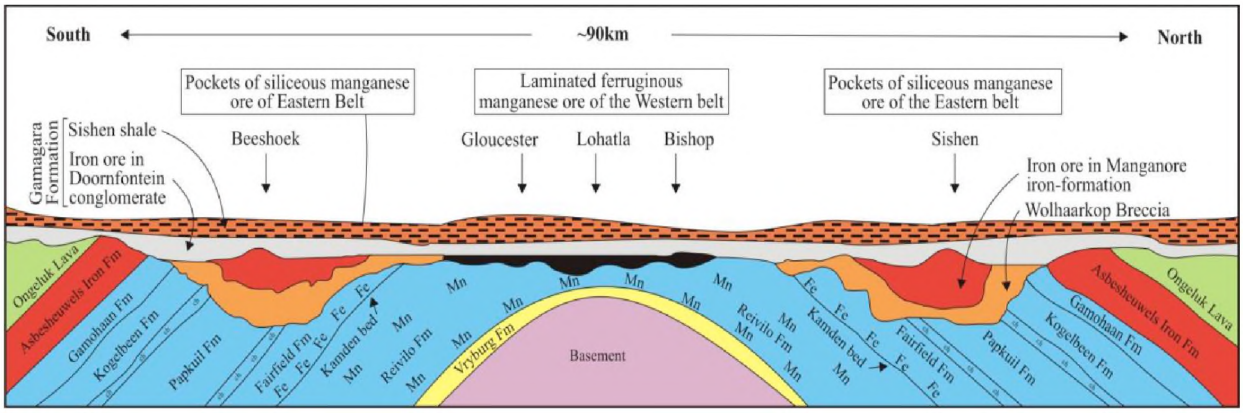

Figure 1.3: North-South cross-section through the Maremane dome (see Figure 1.2). Karstic solution collapse structures, such as those seen at Sishen and Beeshoek host deposits of high-grade iron ore. In the north and south the sampled cores transect the Gamagara Formation and lower lying iron ore in the Sishen and Beeshoek collapse structures respectively. The unconformity transects a variety of rock types due to the folded and tilted nature of the Transvaal Supergroup (modified after Da Silva, 2011).

1.3.5. Mapedi Formation

It was convincingly demonstrated by Beukes and Smit (1987) that the Mapedi Formation, which occurs off the Maremane dome, is a lateral correlative of the Gamagara Formation. The main evidence lies in the strikingly similar petrographic, stratigraphic and sedimentological nature of the Mapedi Formation to that of the Gamagara. This evidence indicates that these two formations were deposited as a single rock unit and are duplicated by the low-angle westerly dipping thrust faults (Beukes & Smit, 1987). Some differences occur in the basal sections, where the Mapedi Formations' basal conglomerate is not as thick as that which is found in the Gamagara Formation (Schalkwyk, 2005). Basal portions of the Mapedi do not display highly aluminous and ferruginous successions of lateritic sediments as those found in the basal parts of the Gamagara (Schalkwyk, 2005).

1.3.6. Provenance

It is well noted in the literature that the Postmasburg Group of the Transvaal Supergroup hosts lateritic paleosols developed in the andesitic lavas of the Ongeluk Formation (Beukes & Smit, 1987; Gutzmer & Beukes, 1998; Beukes *et al.*, 2002; Yamaguchi & Ohmoto, 2006; Land *et al.*, in review). These are locally called the "Drakenstein Paleosol" and "Wolhaarkop Paleosol" which have been widely recognised in the geologic record of the Kaapvaal Craton (Holland & Beukes, 1990; Wiggering &

Beukes, 1990). These paleo-weathering profiles have been suggested to represent the provenance of the Gamagara and Mapedi Formations (Yamaguchi & Ohmoto, 2006; Shivute, 2006; Kalumbu, 2006). The lateritic paleosols are characterised by fine grained hematite, iron-rich chlorite and abundant sericite. The quantity of sericite results in a large excess of K_2O relative to the concentration of Al_2O_3 that could have been weathered from the suggested Ongeluk lavas (Wiggering & Beukes, 1990). This excess potassium is suggested to be derived from basin water, groundwater circulation or metamorphic fluids during the deposition of the overlying red beds (Wiggering & Beukes, 1990).

Yamaguchi and Ohmoto (2006) use Al_2O_3/TiO_2 ratios and the Chemical Index of Alteration (CIA) to determine that the red shales are detrital accumulations of lateritic soils that were produced from moderate to intense chemical weathering of intermediate to felsic source, pointing to the Ongeluk as the likely parent rock. Kalumbu (2006), looking to correlate the Mapedi with the Gamagara, noted a similar trend in High Field Strength Elements (HFSE) in the lower halves of both red shale intercepts. This is interpreted as being derived from a common source and suggested that the highly oxidized zone of the laterite horizon in the Ongeluk Formation is the likely source (Kalumbu, 2006).

1.3.7. Colour variations

Colour variations in the shale beds (red to pale-green to white) have been suggested to be due to either leaching of Fe^{2+}-bearing silicates or the reductive dissolution of Fe^{3+}-oxide minerals by organic acids, resulting in diagenetic alteration from red shales to pale-green and white shales (Yamaguchi & Ohmoto, 2006; Shivute, 2006). Yamaguchi & Ohmoto (2006) along with Kulumbu (2006) infer that the main pigmenting agent in the red shales, hematite, was formed during the lateritic weathering of the Ongeluk, rather than by later oxidation or weathering of pre-existing ferrous minerals in the shales. Land (2010), on the other hand, observed hematite zones cross-cutting primary bedding features suggesting that the presence of oxidising fluids caused the oxidation of Fe^{2+}-bearing minerals to Fe^{3+}-bearing (hematite). Furthermore, these fluids may have been responsible for the HFSE enrichment evident in basal sections of the shales (Land, 2010).

1.3.8. Metasomatic Influences

Land *et al.* (in review) interprets the HFSE enrichments (namely Ti, Nb, Zr and Y) in the basal sections to be anomalous and notes that the simple mechanism of chemical weathering of the Ongeluk cannot account for the data observed. Using techniques obtained by Fralick (2003), Land *et al.* (in review) plotted immobile elements (Zr/TiO_2 vs Nb/Y) for the shales of the Mapedi Formation which indicates the source cannot be that of basaltic andesites, suggesting that either the Ongeluk is not the true parent rock, or that the Mapedi shales record a hydrothermal signature.

It is reported in literature that under certain conditions HFSE can become mobile (Jiang *et al.*, 2005; González-Álvarez & Kerrich, 2010). Using this information Land *et al.* (in review) suggested that the carbonates from the underlying Transvaal Supergroup may have buffered diagenetic fluids, forming high pH solutions. These solutions in turn may have dissolved fluorine from the carbonates of the Campbellrand Subgroup or the Mooidraai Formation, resulting in a fluorine-rich oxidising brine, capable of transporting high concentrations of HFSE in solution. Furthermore, petrographic analyses of both primary rutile crystals and rutile crystals growing at the expense of Ilmenite is evident (Land *et al.*, in review). The aforementioned alkaline oxidising fluids are considered to be the driving reaction of ilmenite breakdown and subsequent rutile growth (Land *et al.*, in review). The fluids would also be capable of introducing titanium into the system to form new rutile grains, explaining the enriched concentrations of TiO_2 and Nb in the Mapedi shales (Land *et al.*, in review). Although the source of the fluids is not clear, they appear to be structurally controlled by higher lying quartzite beds and thus mostly affect the geochemistry of the basal sections of the Mapedi Formation (Land *et al.*, in review).

2 SAMPLING AND METHODS

A total of 146 samples from ten cores drilled through the Gamagara stratigraphy were selected for this study (Table 2.1). Forty of these came from two cores on the southern margin of the Maremane dome (Beeshoek; Figure 2.1). The remaining 106 samples were obtained from eight cores drilled roughly along a north-to-south trend on the northern margin of the dome (King, Bruce and Sishen; Figure 2.1). Samples were selected in order to best represent the sedimentological and overall stratigraphic changes within the Gamagara Formation. Previous studies of the Mapedi Formations allow comparison with drill cores collected in the Kalahari Manganese Field (KMF) where the unconformity transects the Hotazel Formation. With these additional studies, the author is able to compare and discuss the shale formation on a regional scale (i.e. 140km along an approximate north-south strike; Figure 2.2).

Table 2.1: Sampling sites and core co-ordinates. Core N99 is from a previous study and only used for comparative purposes (Land et al., in review).

Core Number	Site	Co-ordinates	
		Latitude	Logitude
PO1/48	Beeshoek	28°20'11.51"S	23° 1'9.11"E
IO2/85	Beeshoek	28°19'58.83"S	23° 0'48.66"E
ALK3/22	King Farm	27°53'45.38"S	22°58'46.72"E
WK4/25	King Farm	27°52'7.27"S	22°59'47.01"E
QK4/89	King Farm	27°51'45.30"S	22°59'54.33"E
HR4/98	Bruce Farm	27°46'22.24"S	23° 0'29.05"E
SA2072E	Sishen	27°43'3.61"S	22°58'11.79"E
SA2093E	Sishen	27°43'1.39"S	22°58'6.69"E
SA2491E	Sishen	27°43'38.51"S	22°58'3.17"E
GA1522E	Sishen	27°44'57.25"S	22°58'41.89"E
N99	Black Rock	27° 7'39.91"S	22°50'16.28"E

Core samples of 10 to 15 cm were collected to minimize effects of compositional inhomogeneity related to millimetre scale laminations of the shales. Highly representative samples were selected from the 146 samples obtained to carry out further investigation using the techniques that follow. Petrographic investigations were carried out on thin sections under transmitted and reflected light microscopy, and were complimented by backscattered electron (BSE) and wavelength dispersive (WDS) maps using the electron probe micro-analyser (EPMA). Where necessary select mineral chemistry was also determined

using the EPMA. Whole-rock mineralogical compositions were determined using X-ray diffraction (XRD) and their major and trace chemical compositions were obtained by X-ray fluorescence (XRF) spectrometry. Rare Earth Element (REE) and Nd isotope analyses were performed on a quadrupole inductively coupled plasma mass spectrometer (ICP-MS) and a multicollector ICP-MS respectively. Analytical procedures for each technique employed are reported prior to the presentation of results.

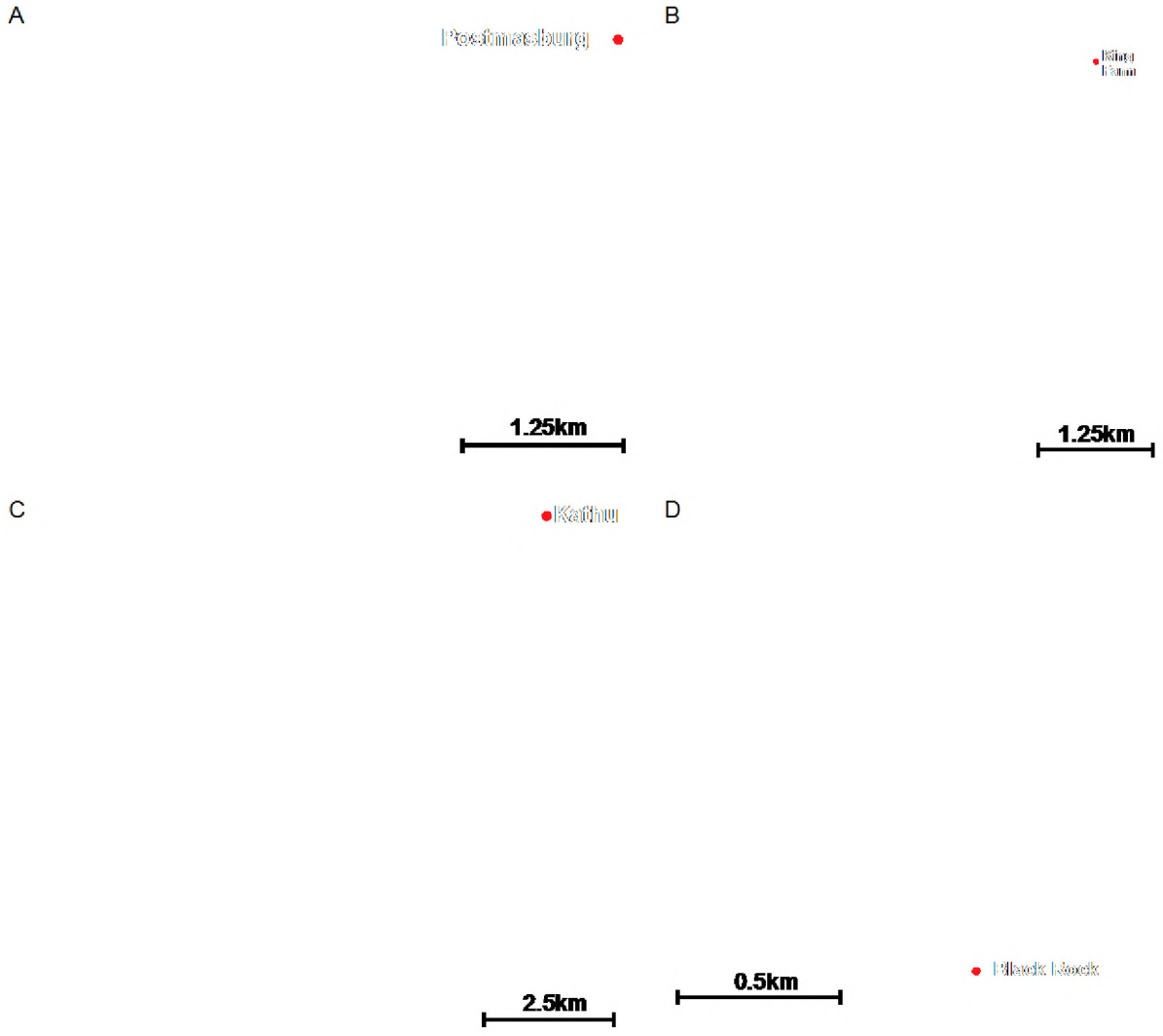

Figure 2.1: Sample sites and spatial distribution of the cores. The cores cover 140km strike from Beeshoek in the south to Black Rock in the north (a) Two Beeshoek cores located at the southern margin of the Maremane dome. Centre of image co-ordinates: 28°19'58.55"S 23°00'49.94"E (b) Three King Farm cores located 20 km south of Kathu. Centre of image co-ordinates: 27°52'36.74"S 22°59'42.66"E (c) Five cores, one located on Bruce Farm (HR4/98) and four located at Sishen on the northern edge of the Maremane dome. Centre of image co-ordinates: 27°44'27.17"S 23°00'19.10"E. (d) Core N99 sampled by Land *et al.* (in review) for comparative purposes. Centre of image co-ordinates: 27°07'50.53"S 22°50'15.83"E. Images modified from Google Earth.

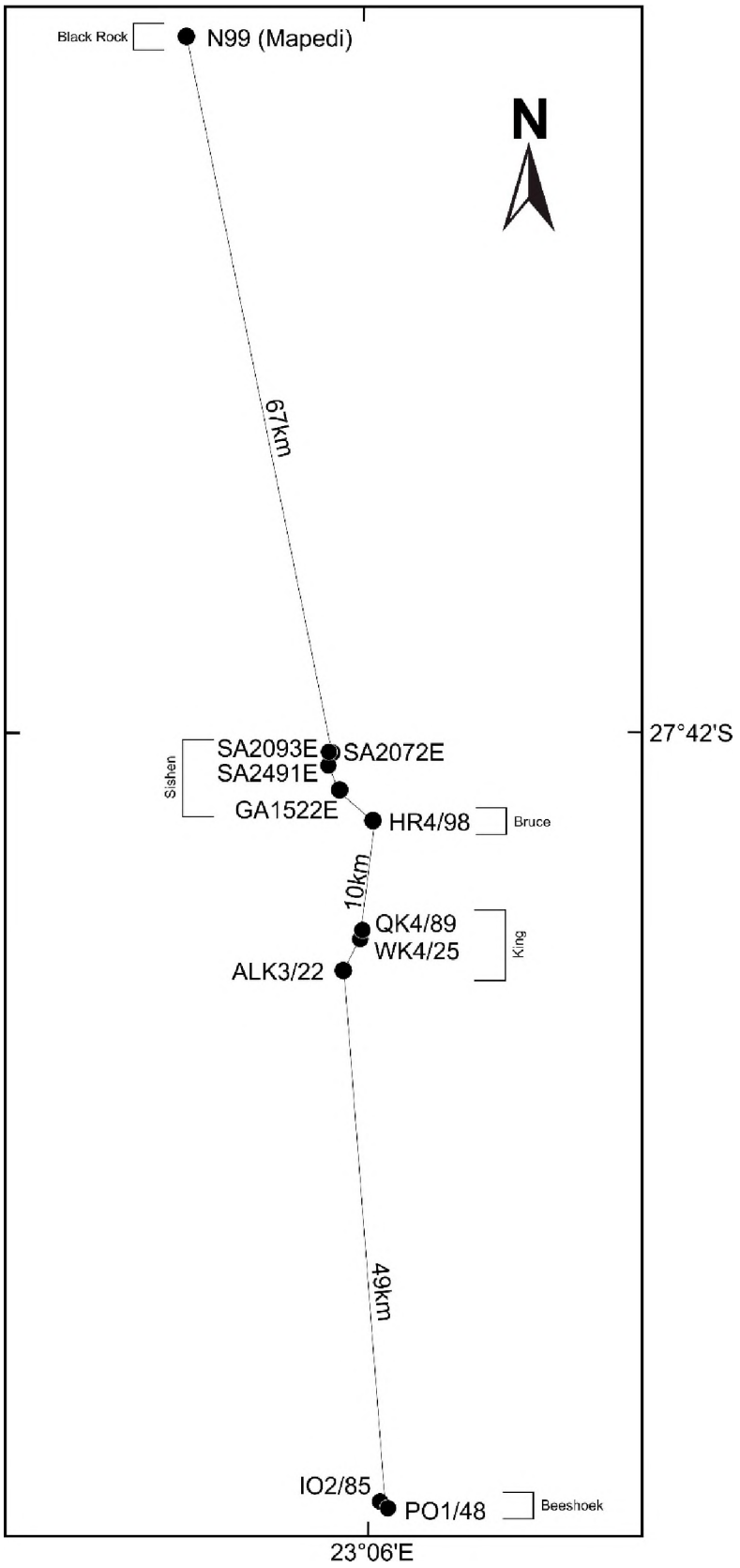

Figure 2.2: Spatial distribution of the 10 sampled cores and the Mapedi Core (N99; Land *et al.*, in review)

3 LITHOSTRATIGRAPHY

Schematic logs for the ten drill-cores containing the Gamagara Formation, including stratigraphic depths for representative samples used in this study are presented in this chapter (Figure 3.2, Figure 3.3, Figure 3.4 and Figure 3.5). The descriptions in each log were compiled from observations made during this study.

3.1. Logs

Based on the farms from which they were drilled, the logs have been divided into four sites, namely Beeshoek, King, Bruce and Sishen. Shale colour variations which occur in the various lithofacies have been marked accordingly (see legend for all schematic logs in Figure 3.1). Units which are ferruginous have been marked with a purple background. Portions of the stratigraphy underlying the shales of the Gamagara are included in the schematic logs in order to determine the nature of the contacts. Iron ore bodies referred to in-text and in the logs are the lithofacies underlying the Gamagara Formation which are strongly ferruginous (>70% by observation). The full extent of the 'ore bodies' have not been explored as it is not in the scope of this thesis. Furthermore, no geochemistry was done on these units in order to determine iron content. The label 'ore body' is therefore only a descriptive term, determined by mesoscopic observations of the drill-core.

Stratigraphic and structural evidence in the Griqualand West basin found that major thrust faults displace the Transvaal and Olifantshoek strata near the western margin of the Kaapvaal Craton (Beukes and Smit, 1987). Complex tectonic patterns can emerge in the shales of the Gamagara and geology can become complicated in areas where shearing and duplication is widespread. Shear zones have been marked by means of white and black diagonal lines (depending on the background colour in each log). Zones in which there has been poor core recovery (i.e. highly fragmented or missing core) often return with shearing noticeable in the shale laminae and is interpreted to be brittle deformation as a result of fracturing and frictional sliding over a width which may be determined by competency contrasts.

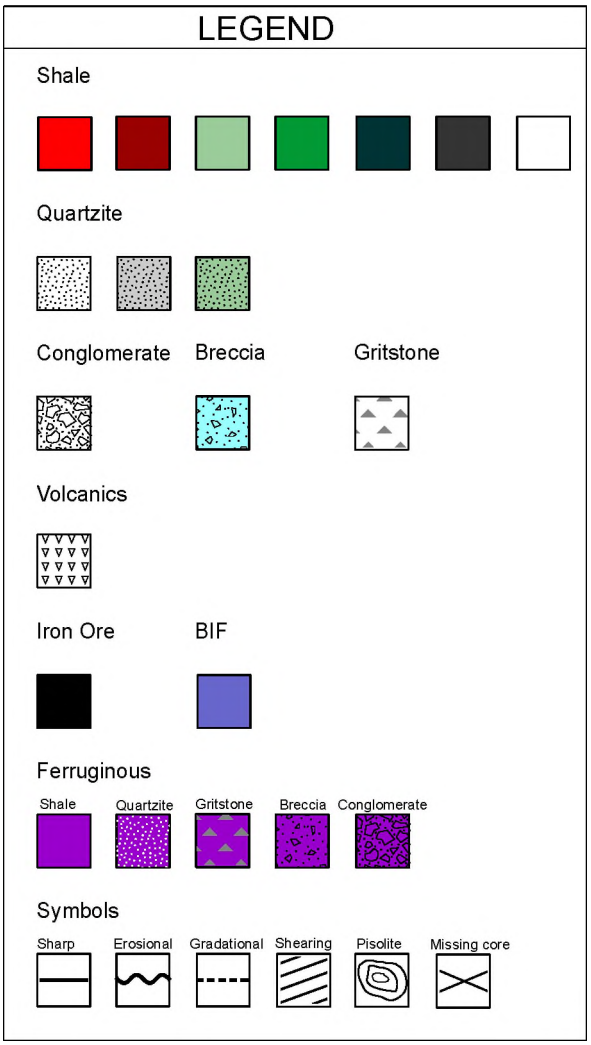

Figure 3.1: Key for schematic logs which follow.

3.1.1. Beeshoek

Core IO2/85

One hundred and forty eight metres of core IO2/85 was logged (318m→170m) to capture the Gamagara Formation and its relationship with the underlying units (Figure 3.2 A). At the base of the core, interbedded banded iron-formation (BIF), chert breccia (Wolhaarkop) and a relatively thin (ca. 40 cm) red shale with white laminae is found. The breccia cuts the BIF and shale with sharp erosive contact. A body of thinly laminated iron-ore overlies this unit with sharp contact. The ore body is sharply overlain by a ferruginous conglomerate in a red mud matrix. The conglomerate upward fines into a matrix supported gritstone before ending abruptly to an overlying purple ferruginous shale unit with silt

laminae (upward fining). This is overlain by sharp contact with brick red shale exhibiting white laminae that terminates sharply against a pure white quartzite (upward coarsening). The quartzite is sharply overlain by dark red shale with white laminae. The shale ends abruptly and white quartzite returns, this time with thin infrequent millimetre-to-centimetre scale red shale beds. A coarse-grained, gritty quartzite caps the top 60 cm of this quartzite unit and ends with a sharp contact (upward coarsening). A similar looking dark red shale with white laminae overlies the quartzite which, over the following 83 metres of core, gradual colour changes take place. The laminae of these dark red shales gradually become green and the red colouration fades becoming pale green then dark green and back into pale green. As the green colour fades in the shale, subtle red colours return but green laminae continue through. Gradually, green shales return and frequent quartzite laminae return until a coarse-grained pale green to white quartzite appears (upward coarsening). Pale green shale overlies this with sharp contact and over the next 30 metres, a similar cycle of green shales gradually fading into and out of red shales continues until the top of the log.

Core PO1/48

One hundred and seventy five metres of core PO1/48 was logged (377m→202m) to capture the Gamagara Formation and its relationship with the underlying units (Figure 3.2 B). At the base of this core, chert breccia in a dark purple ferruginous matrix is interbedded with BIF. Gradually, the entire sequence becomes dark purple to grey as it becomes fully ferruginised, making up a thinly laminated and brecciated ore body. Red shales appear sporadically interbedded with ferruginous thinly laminated ore. The ore body is sharply overlain by a ferruginous conglomerate in a red mud matrix. The conglomerate upward fines into a matrix supported gritstone before ending abruptly to an overlying white shale (upward fining). The white shale gradually becomes a dark purple ferruginous shale with silt laminae before gradually changing into a brick red shale with white laminae. The red shales are terminated by a sharp (erosive) contact by a 5 cm gritstone with angular ferruginous granules in a white quartzite matrix followed by pure white quartzite (upward coarsening). The quartzite is overlain by 1.5 metres of dark red shale with green laminae and cm-scale quartzite beds which gradually switches back into white quartzite with irregular cm-scale dark red shale beds. A coarse-grained, gritty quartzite caps the top 1 metre of this quartzite unit and ends with sharp contact (upward coarsening). A similar dark red shale with white laminae overlies the quartzite which, over the following 29 metres of core, switches from pale green to red to dark green shales. Over the next 83 metres of core, two shear zones are identified. In the first shear zone repetition within the green shales occurs. In the second shear zone a black shale appears for ~7.5 metres until the shear zone ends with sharp contact and repetition of the green shales continue until the top of the log.

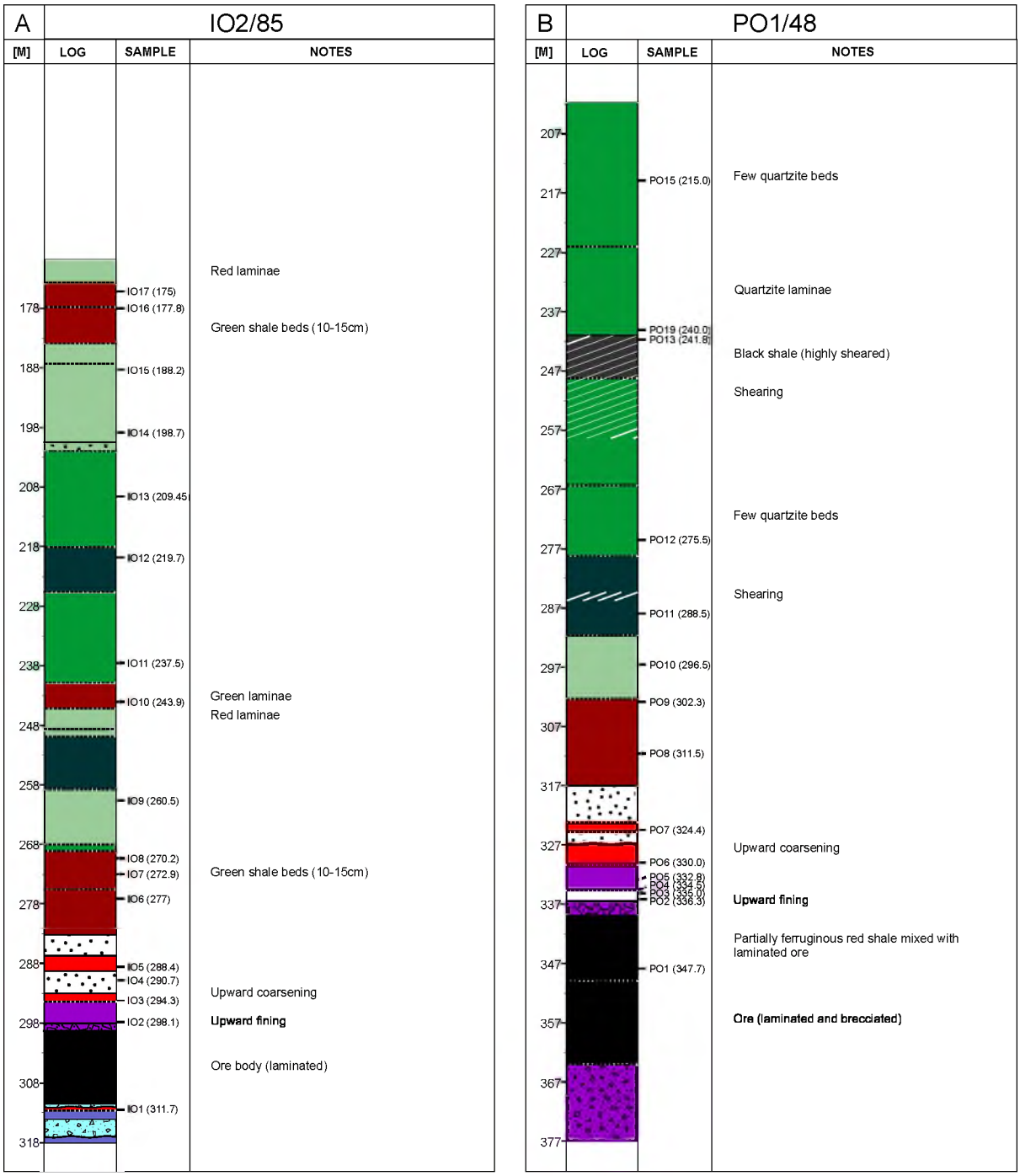

Figure 3.2: Schematic stratigraphic logs of the Gamagara Formation at Beeshoek displaying sample locations on a true vertical scale. Cores include IO2/85 and PO1/48.

3.1.2. King

Core ALK3/22

One hundred and ninety seven metres of core ALK3/22 was logged (396m→199m) to capture the Gamagara Formation and its relationship with the underlying units (Figure 3.3 A). The ore body at the base of the core is mostly brecciated, alternating between BIF and chert clasts. Highly fragmented ore is found at a sharp contact with overlying chert breccia. The chert breccia is bright yellow in colour and is interbedded with a ferruginous chert breccia. This unit is capped by 40 cm of brick red shale with highly sheared yellow laminae. This unit has been interpreted as a shear zone and has possibly undergone secondary limonitic alteration by meteoric fluid flow which exploits the shear and imparts the yellow colouration. The brick red shale is sharply overlain by a dark purple ferruginous conglomerate and is terminated by sharp contact with a white shale which gradationally becomes black. The black shale coarsens upwards into a coarse-grained, gritty shale, until capped by a 60 cm ferruginous gritstone (upward fining). The gritstone is sharply overlain by a brownish-red shale with white laminae which upward coarsens as the laminae become quartzitic. Quartzite laminae thicken until a grey quartzite dominates with sporadic 3 to 5 cm brown shale beds. The shale beds disappear and the grey quartzite continues, gradually grading into a pure white quartzite (upward coarsening). The white quartzite terminates with sharp contact and over the following 82 metres of core green shale and dark red shale continue. The shale laminae gradually coarsen until a pale green quartzite caps the top 6 metres of the log (upward coarsening).

Core WK4/25

One hundred and forty three metres of core WK4/25 was logged (146m→3m) to capture the Gamagara Formation and its relationship with the underlying units (Figure 3.3 B). The base of the core contains a chert breccia which gradually becomes a brecciated and laminated ore body. The ore is sharply terminated by overlying brick red shales with white laminae. The red shales begins fragmented with sheared laminae and is possibly thrust emplaced. The red shales continues until the laminae become increasingly quartzitic which continues until a grey quartzite dominates and red shales become infrequent laminae in the quartzite package. The grey quartzite is capped by 10 cm of a coarse-grained, gritty quartzite (upward coarsening). A package of red shale with white laminae and alternating cm-scale quartzite beds overlies the gritty quartzite with sharp contact and gradually transitions into pure grey quartzite which changes into a white quartzite (upward coarsening). Green shales overlie the

quartzite with sharp contact and over the following 44.5 metres, the core gradually alternates between green, red, and dark green shales. A sharp contact separates the dark green shales with a zone of highly weathered yellow shale. As the top portion is so near to the modern surface, meteoric waters is likely to be the cause of alteration in these yellow shales.

Core QK4/89

One hundred and twenty four metres of core QK4/89 was logged (138m→14m) to capture the Gamagara Formation and its relationship with the underlying units (Figure 3.3 C). The base of the core contains chert breccia interbedded with BIF which gradually changes into laminated and brecciated ore capped by 1.4 metres of ferruginous pebble conglomerate in a red hematite matrix. This cap gradually changes into ferruginous red shale (upward fining) with fine-grained quartzite laminae which upward coarsens into a coarse-grained, gritty ferruginous quartzite. The ferruginous cap terminates sharply and is overlain by brick red shale with white laminae. The red shales continue until the laminae become increasingly quartzitic. This continues until a grey quartzite dominates and red shales become infrequent laminae in the quartzite package. The grey quartzite is capped by 20 cm of a coarse-grained, gritty quartzite (upward coarsening). A package of red shale with white laminae and alternating cm-scale quartzite beds overlies the gritty quartzite with sharp contact and gradually transitions into a grey quartzite which changes into a pure white quartzite (upward coarsening). Green shale with frequent red laminae overlies the quartzite with sharp contact and over the following 20 metres of core, red shales gradually alternate with cm-scale green shale beds. The final 16 metres of core contains the highly weathered yellow shale as observed in core WK4/25.

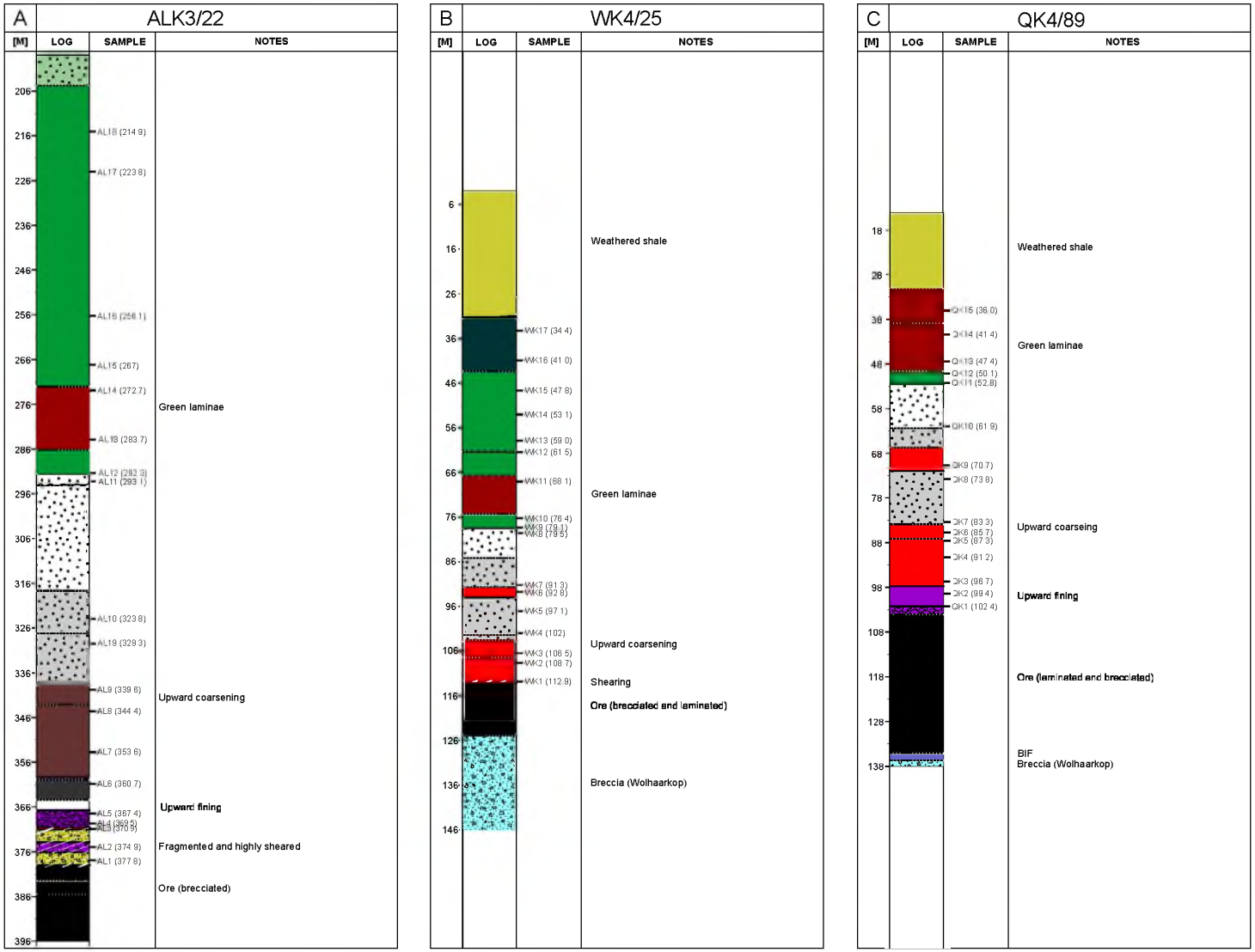

Figure 3.3: Schematic stratigraphic logs of the Gamagara Formation at King displaying sample locations on a true vertical scale. Cores include ALK3/22, WK4/24 and QK4/89.

3.1.3. Bruce

Core HR4/98

One hundred and ninety five metres of core HR4/98 was logged (224m→29m) to capture the Gamagara Formation and its relationship with the underlying units (Figure 3.4). The base of the core contains brecciated BIF clasts in a ferruginous matrix grading into a thinly laminated ore body. The conglomerate upward fines into a purple to dark red ferruginous shale. With sharp contact, a dull red with white, highly sheared laminae overlie the ferruginous shale and terminates sharply back into ferruginous shale. The ferruginous shale gradually becomes lighter in colouration with the introduction of highly sheared white laminae which terminates sharply into a relatively thin (1.5 metre) ferruginous shale bed. The ferruginous shale bed is sharply overlain by approximately 100 metres of black shale containing frequent white aluminous shale beds. The laminae and thin (~2 cm) beds in the black shale are convolute and contorted throughout the sequence. In the top 5 metres of core, only thin laminae are present in the black shale until gradually a ferruginous dark red shale remains. The ferruginous shale upward coarsens with the introduction of quartzite laminae and progressively transitions into a white quartzite interbedded with red shale (upward coarsening). The unit is capped by a highly fragmented red shale with sheared laminae. With sharp contact a ferruginous conglomerate, very similar to the aforementioned conglomerate at the base of the log continues to the end of the log.

3.1.4. Sishen

Core GA1522E

One hundred and thirteen metres of core GA1522E was logged (234m→121m) to capture the Gamagara Formation and its relationship with the underlying units (Figure 3.5A). The base of the core contains brecciated BIF clasts in a ferruginous shale matrix. The contact with the overlying ferruginous dark red to purple shale is unknown due to missing core. The ferruginous shale is interbedded with minor brecciated ore beds (~20-40 cm length). Ore breccia clasts become visible and gradually decrease as the unit upward fines into a ferruginous dark red gritstone which fades into a gritty green shale with pisoliths developed in it. The green shale gradually changes to a white shale and terminates sharply against a black shale which gradually fades back into a white shale. The white shale gradually changes into a purple ferruginous quartzite until capped by a gritstone (upward coarsening). This zone is sharply

overlain by a red shale with white laminae which contains thin (~3 cm) poorly-sorted pebble conglomerate beds. This red shale gradually coarsens upwards with increasing quartzite laminae before changing to a white quartzite with infrequent red shale laminae until a pure white quartzite remains. The quartzite is capped by 25 cm of coarse-grained, gritty quartzite (upward coarsening). The coarse-grained quartzite is sharply overlain by a red shale with quartzite laminae and is terminated sharply by overlying amygdaloidal lavas. A 1 metre contact areole exists between the red shales and lavas.

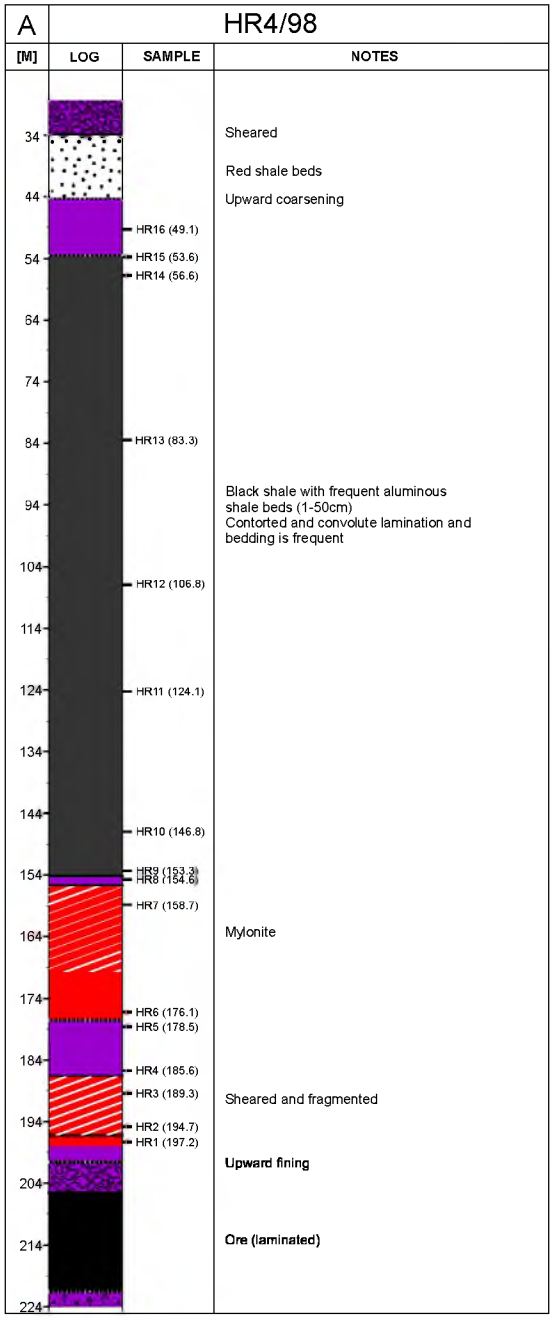

Figure 3.4: Schematic stratigraphic logs of the Gamagara Formation at Bruce displaying sample locations on a true vertical scale. Core HR4/98.

Core SA2491E

Eighty three metres of core SA2491E was logged (275m→192m) to capture the Gamagara Formation and its relationship with the underlying units (Figure 3.5B). The base of the core contains thinly laminated ore overlain by a BIF and hematite pebble conglomerate in a dark purple ferruginous matrix. The conglomerate grades into a thinly laminated fine-grained ferruginous quartzite which upward coarsens into gritstone developed in a ferruginous matrix. The gritstone terminates sharply and is overlain by a highly fragmented red shale with sheared white laminae. The shale upward coarsens by increasing quartzite laminae until a grey quartzite is developed. This quartzite gradually becomes white and is capped by a coarse-grained gritty white quartzite (upward coarsening) overlain sharply by a brick red shale with white laminae. This red shale is sharply cut by a mylonitised red shale interbedded with infrequent contorted green shale beds which upward coarsens by increase in quartzite laminae. Amygdaloidal lavas sharply overlie the shales with a 1 metre contact areole separating the units.

Core SA2072E

One hundred and twenty four metres of core SA2072E was logged (238m→114m) to capture the Gamagara Formation and its relationship with the underlying units (Figure 3.5C). The base of the core contains thickly laminated BIF overlain by laminated ore. The contact is sharply cross-cut by an intrusive dyke or sill. The top of the ore body becomes fragmented making the contact with the overlying dark purple ferruginous shale unclear. Much of the core is missing due to poor core recovery but a metre of highly fragmented red shale with white laminae appears briefly in the missing section. Above this lies a ferruginous conglomerate overlain by a highly fragmented upward coarsening red shale with increasing quartzite laminae. As quartzite laminae begins to increase, fragmentation lessens until it stops with an overlying white quartzite. Shear lines mark the thrusted units in the log. The quartzite upward coarsens into a pure white quartzite before upward fining as shale laminae increase. A sharp contact with overlying red shales terminate the quartzite and a contorted mylonitised red shale with white laminae and beds (5-10 cm thick) continues. Amygdaloidal lavas sharply overlie the shales with a 0.5 metre contact areole separating the units.

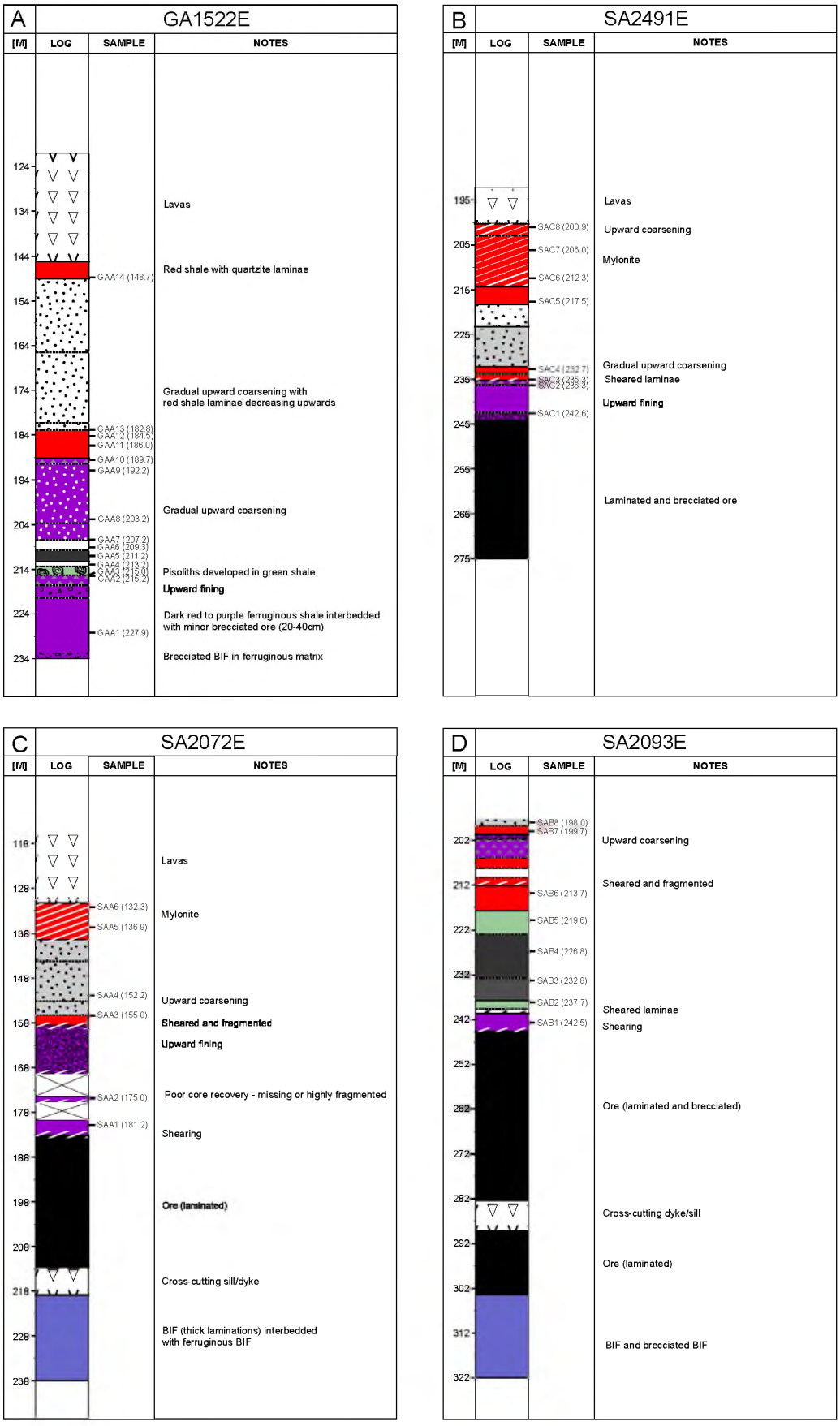

Figure 3.5: Schematic stratigraphic logs of the Gamagara Formation at Sishen displaying sample locations on a true vertical scale. Cores include GA1522E, SA2491E, SA2072E and SA2093E.

Core SA2093E

One hundred and twenty five metres of core SA2093E was logged (322m→197m) to capture the Gamagara Formation and its relationship with the underlying units (Figure 3.5D). The base of the core contains laminated BIF interbedded with brecciated BIF and is overlain by thinly laminated ore. The ore body is cross-cut by an intrusive dyke or sill. A zone of fragmented dark purple ferruginous shale overlies the ore with sharp contact. A zone of white to pale green shale, highly fragmented at the base, overlie the ferruginous shale with sharp contact. A sharp contact terminates the green shales and dark grey to black shales continues which gradually fade into green shales before fading into pale red shales with yellow laminae. Above this with sharp contact lie interbedded white and red shales which gradually upward coarsen, becoming gritty with a dark red ferruginous matrix until a one metre mature hematite pebble conglomerate caps the unit. The conglomerate is overlain with sharp contact by a red and white banded shale unit which gradually coarsens upwards by increasing quartzite laminae until a grey quartzite with shale laminae marks the end of the core.

3.2. Summary of Lithostratigraphy

Variations occur in stratigraphic sequences encountered in the drill-cores because of the nature of the angular unconformity between the Transvaal and Gamagara strata. Facies variations in the basal units of the Gamagara Formation are most likely due to paleotopographic irregularities on the underlying erosion surface. The presence of a low angle thrust fault, transecting strata in both the under-and overriding tectonic plates can further complicate matters.

3.2.1. Anomalous Core HR4/98

The most anomalous core sampled here is that which lies on Bruce Farm (HR4/48). The presence of the convolute and contorted bedding of the 100m thick black shale lithofacies suggests that slumping may have occurred (Figure 3.4 and Figure 3.6). These structures may form where the sediment is deposited on a slight slope (Nichols, 2009). In a study on the structure and geometry of the Sishen iron ore deposit, Van Schalkwyk and Beukes (1986) report slumping into basin-like structures on the eastern boundary of the Sishen south pit area. Core HR4/98 fall in close proximity to the Sishen south pit and also falls to the east of all Sishen cores (Figure 2.2). Such structures may have been responsible for the thickness of the black shales (compared to all other cores) as well as the deformation seen in core

HR4/98. Evidence of shearing above and below the black shales in core HR4/98 further complicates the stratigraphic correlation of this core to the other sampled cores and as such it has been left out of the final correlation sequence in Figure 3.7.

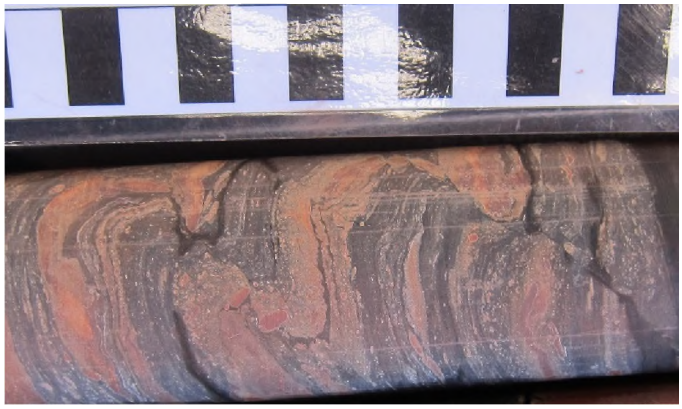

Figure 3.6: Convolute lamination and bedding in the black shales of core HR4/98 on Bruce Farm. In a slumped sequence, the folds in the layering tend to be asymmetric, with the nose of the anticline pointing downslope. Way up direction is right to left, centimetre scale bar attached.

3.2.2. Correlations

Schematic logs for the nine remaining drill cores containing the Gamagara Formation is presented in Figure 3.7. For ease of reference, names of the specific units are kept according to the previous work done on the Gamagara Formation (see section 1.3.4). Apparent lateral correlations between cores are based on lithostratigraphic markers and, from the basal units moving up stratigraphy occur as follows:

(a) The Transvaal/Olifantshoek unconformity separates the iron ore body with the Gamagara Formation. Where shearing is present at the iron ore interface, portions of the stratigraphy may be missing and correlation occurs accordingly (i.e. cores WK4/25, SA2072E and SA2093E).

(b) As the Doornfontein Member is highly variable across cores, the next lithostratigraphic marker occurs at the base of the red shales of the Sishen Member.

(c) The interface between the Marthaspoort quartzite and the Paling shale member marks the final correlation for the cores at Beeshoek and King. At Sishen, the sampled cores do not include the Paling shale member, instead lavas overlie red shales of the Sishen Member (i.e. cores GA1522E, SA2491E and SA2072E) and have been correlated accordingly (using QK4/89 as a proxy).

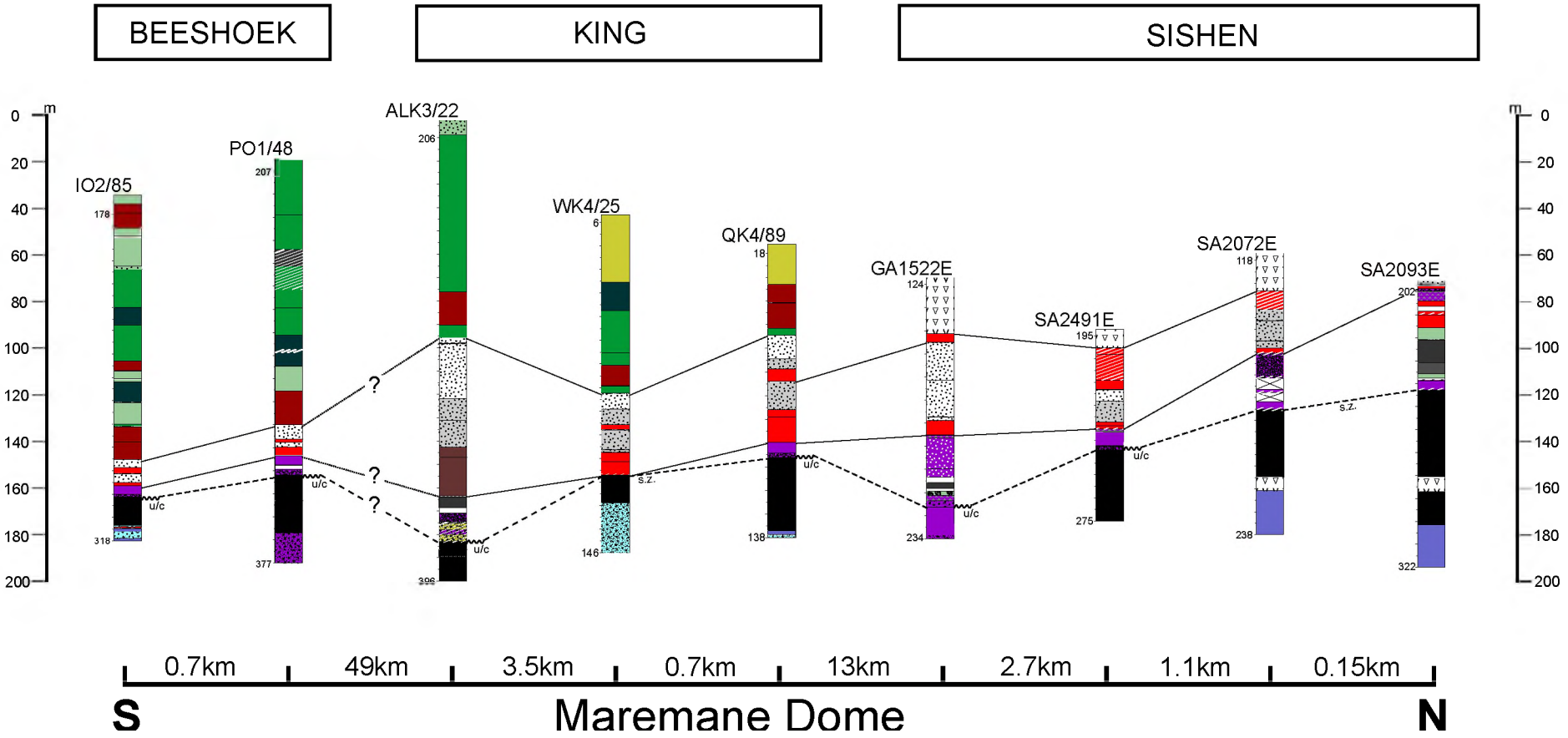

Figure 3.7: Correlation of the schematic stratigraphic logs of the Gamagara Formation on the Maremane Dome (S-N strike of ~71km). Dashed lines follow the unconformity which separates the Transvaal Supergroup from the Gamagara Formation (Olifantshoek Supergroup). Broken lines with question marks indicate uncertainty between Beeshoek and King mine as no data was obtained in the 49km stretch between these cores. u/c refers to the unconformity, s.z. refers to a shear zone.

The correlations of the Gamagara stratigraphy took into consideration the proximities of each core, highly comparable macroscopic characteristics and geochemical characteristics which are displayed later in this thesis. The thickness of the Doornfontein, Sishen and Marthaspoort Members (most notably the quartzites) are highly variable between Beeshoek and King/Sishen which lie on opposite ends of the Maremane dome (49km apart) and is possibly due to the basin geometry in the primary depositional environment.

3.2.3. Lavas

Lavas overlying the red shales of the Sishen Member were identified in three of the cores located at the Sishen Farm (GA1522E, SA24981E, SA2072E; Figure 3.5). These lavas have always been interpreted as thrust emplaced Ongeluk lavas as they were observed to always occur above a zone of mylonitised shales (Van Schalkwyk and Beukes, 1986; Schütte, 1992). This mylonite zone was recognised below amygdaloidal lavas in cores SA2491E and SA2072E, however, the mylonite was completely absent in core GA1522E. Contact metamorphism up to ca. 0.5m is clearly evident in all three cores and suggests these lavas are not thrust emplaced, but rather represents a period of mafic volcanism occurring after the outflow of the Ongeluk lava. Furthermore, Van Niekerk (2006) also recognised that the volcanic units present in the Gamagara were clearly interbedded with the sedimentary strata and rejected claims of thrust emplacement.

4. MINERALOGY AND PETROGRAPHY

Petrographic and mineralogical studies were conducted on selected representative samples from the ten drill cores. To maintain simplicity the samples were divided into their member groups as per Van Schalkwyk and Beukes' (1986) model in section 1.3.4. Results are displayed starting with the base of the Gamagara and continue up the sequence. All photographs of the samples are orientated in the way-up direction unless otherwise stated. Photomicrographs were examined under plain polarised light (PPL), cross-polarised light (XPL) and reflected light (RL). Centimetre scale bars are attached to the core photographs.

4.1. Mineralogy

4.1.1. Analytical Procedures

Average modal mineralogy was determined semi-quantitatively by use of XRD analyses on 17 samples performed using a Bruker D8 Discover XRD, equipped with a Lynx Eye detector, housed in the Department of Chemistry at Rhodes University. Approximately 1g of the crushed sample was prepared on a glass slide and inserted into the aluminium cavity mount. The instrument uses Cu-Kα radiation (1.5405 Å, nickel filter) and is operated at 20mA and 40kV. The scanning was completed from 5° to 55° (2θ) with speeds of 1° per minute. The X-ray diffraction data was treated using the Eva (evaluation curve fitting) software with baseline corrections performed on each diffraction pattern.

Qualitative phase identifications and semi-quantitative determinations were completed using Crystal Impact's Match 2 software (Windows 8.1) using the crystallographic open database file (rev 140301), all available from http://www.crystalimpact.com/match/. A collation of the spectra obtained for each sample is available in Appendix C. Because of the difficulties involved in petrographic analysis of fine grained sediments, the semi-quantitative data was further refined by bulk rock geochemistry and, where available, WDS element maps in order to produce the data shown in Figure 4.1.

4.1.2. Results

The major minerals identified via XRD include quartz, clays and micas (phengite, illite muscovite, biotite, kaolinite, pyrophyllite and chlorite), oxides (hematite, ilmenite, TiO_2 minerals - rutile, anatase, brookite - and diaspore), phosphates (apatite) and sulphides (pyrite).

Aluminous shales are usually white in colour and contain pyrophyllite, kaolinite and diaspore. The high clay/mica content observed in the aluminous shale unit is the result of high quantities of muscovite/illite/phengite in two of the three samples analysed and thus may reflect sampling bias as high quartz content is observed in petrographic observations. The black shales which usually occur interbedded with the aluminous shales also contain pyrophyllite and diaspore along with pyrite. Although not analysed, these shales are assumed to contain accumulates of organic carbon which forms part of the pelagic sediment and imparts the black colouration. Above the black and aluminous shales, hematite content increases on entering the iron-rich shales and quartzites of the Sishen Member. Hematite content then decreases with the increase of quartz and clay/mica in the red shales above. The red shales of the Sishen Member contain the highest levels of Ti-bearing minerals (titania and ilmenite) in the sequence. Quartz content increases with the decrease in clay/mud in the Marthaspoort member. The sample used for the Marthaspoort was in the transitional zone (shale to quartzite) and had frequent thin mud laminae (Figure 4.6a). The green shales in the Paling Member pick up moderate amounts of chlorite, a mineral which gives these shales their distinct green colouration.

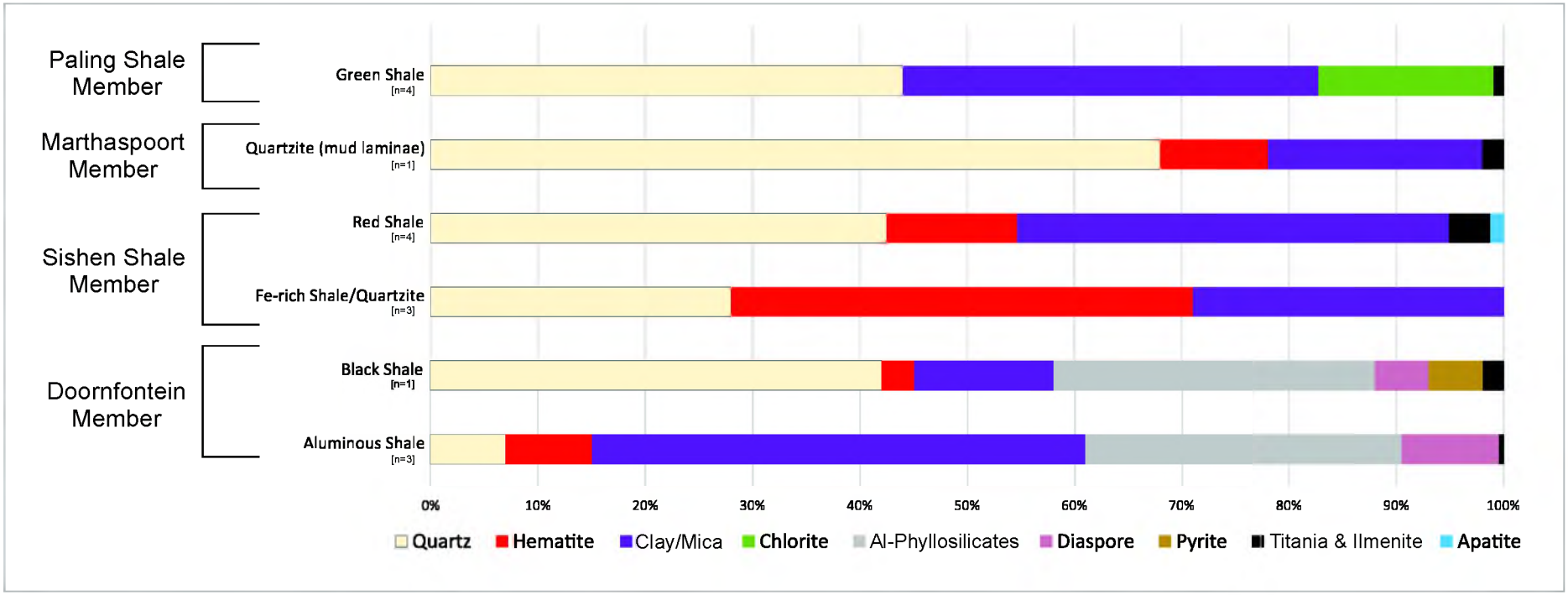

Figure 4.1: Modal mineralogy of the Gamagara Formation derived from semi-quantitative analyses and petrographic observations. Clay/Mica includes phengite, illite, muscovite and biotite. Al-phyllosilicates include kaolinite and pyrophyllite. Diaspore was only observed in the aluminous and black shales. Chlorite (Fe-rich) was kept separate to show its abundance in the green shales. Titania minerals include rutile, anatase and brookite.

4.2. Mesoscopic Observations

4.2.1. The Doornfontein Member

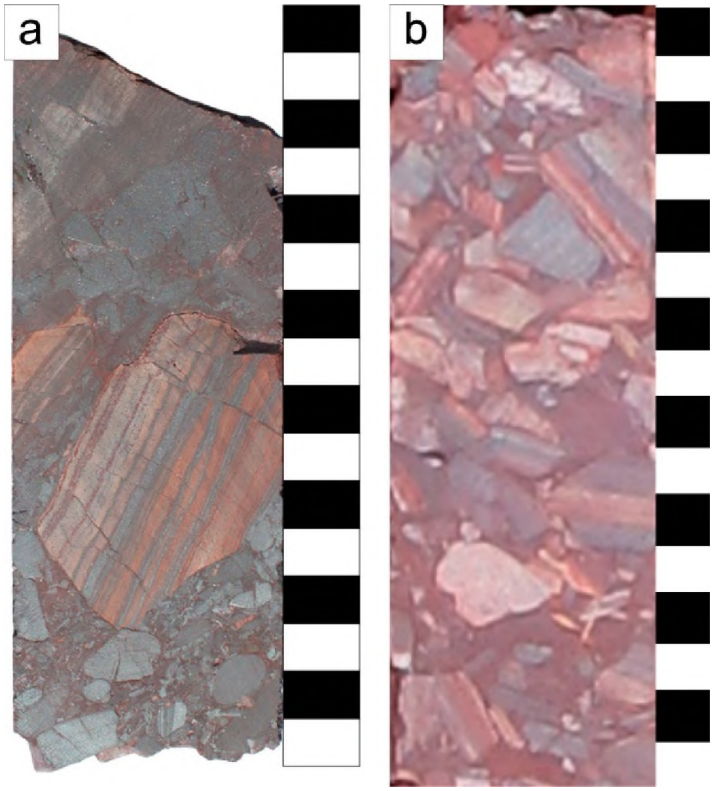

Figure 4.2: Conglomerates of the Doornfontein Member. (a) Core sample situated close to the unconformity resting on the ore body while (b) was found further up in the sequence. Note the differences in ferruginisation between the two end members of the Doornfontein conglomerate. Centimetre scale bars attached.

Conglomerates

The conglomerates consists of pebbles of hematite and clasts of chert and BIF in a hematite rich muddy and granular matrix (Figure 4.2). The hematite pebbles vary in size and are generally well-to-sub-rounded. The BIF and chert clasts may have a large size variance with sub-angular to sub-rounded shape. The conglomerate is generally poorly sorted with reports of BIF clasts reaching sizes of up to 20 cm (Van Schalkwyk, 1984). The hematite pebbles may be massive, but often show crude BIF laminations and are likely to be of BIF origin. The rounding of the hematite pebbles indicates they are from more distal sources than that of the more angular BIF and chert clasts. Moving up stratigraphy, further from the ore body, ore pebbles begin to decrease and the matrix becomes less hematite rich as seen by the clast and colour contrasts in Figure 4.2(a) and (b). The basal portions of

Doornfontein Member (i.e. conglomerates, gritstones and shales) may contain enough iron to form part of the ore body itself.

Shales

The Doornfontein member upward fines by the progressive decrease in clasts and pebbles, becoming a matrix supported gritstone until grading into a hematite-rich red mudstone (base of Figure 4.3a). Although this was only observed in one of the ten examined cores, layers of spherical to subspherical pisoliths may develop in the shale layers and range in size from ~2 to 12 millimetres (Figure 4.3a). White aluminous and black pyritic shales generally overlie the conglomerates in the upward fining sequence (Figure 4.3b) An intimate relationship always occurs between white and black shale units as seen in Figure 4.3b,c,d. The black shale displays thin wavy laminae made up of fine grained sand size quartz, chert, pyrophyllite and diaspore between thicker zones (1 – 2 cm) of pyrite in a black clay matrix (carbonaceous). Lenticular laminae and lithic fragments (up to 4mm in size) are common features of the black shales. White shales are often associated with lenticular beds and what looks to be very fine-grained sand size quartz and chert, wrapping around wavy black laminae in which alumina-rich lenses of pyrophyllite, muscovite and diaspore may occur (Figure 4.3c). In core HR4/98, where a thick pile (~100 m) of slumped black shales have accumulated, evidence of bleaching occurs, leaving behind thick cream coloured beds (up to 40 cm) in which cross-cutting veins may be observed. (Figure 4.3d).

4.2.2. The Sishen Member

Ferruginous Unit

Ferruginous shales/quartzites either overlie the interbedded black and white shales, or they may directly overlie the conglomerates of the Doornfontein Member. Depending on the iron content of the ferruginous unit, they either have a dark red colouration (usually as dark red ferruginous shales underlying the red and white banded shales with sharp contact) or a grey to dark purple colouration (usually as ferruginous quartzites). The latter is discussed here and displayed in Figure 4.4a. The fine-grained iron rich quartzite is locally known on the mine as the 'flagstone' quartzite. At hand scale, it consists mainly of hematite, quartz and chert grains cemented in a hematite matrix. The grain habits are difficult to see in hand specimen and are discussed in microscopic observations. The most obvious sedimentary structure found in the ferruginous quartzites are horizontal planar cross-beds with low angle erosion surfaces (Figure 4.4a). This unit is usually capped by a thin (<15 cm thick) well-developed gritstone containing sub-angular to sub-rounded granules of chert, quartz, hematite and BIF in a hematite-rich clay matrix (Figure 4.4b). However, in one of the cores, the gritstone grades into a mature

pebble conglomerate (~1m thick) containing well rounded BIF, hematite and chert pebbles in a gritty hematite rich matrix (Figure 4.4c).

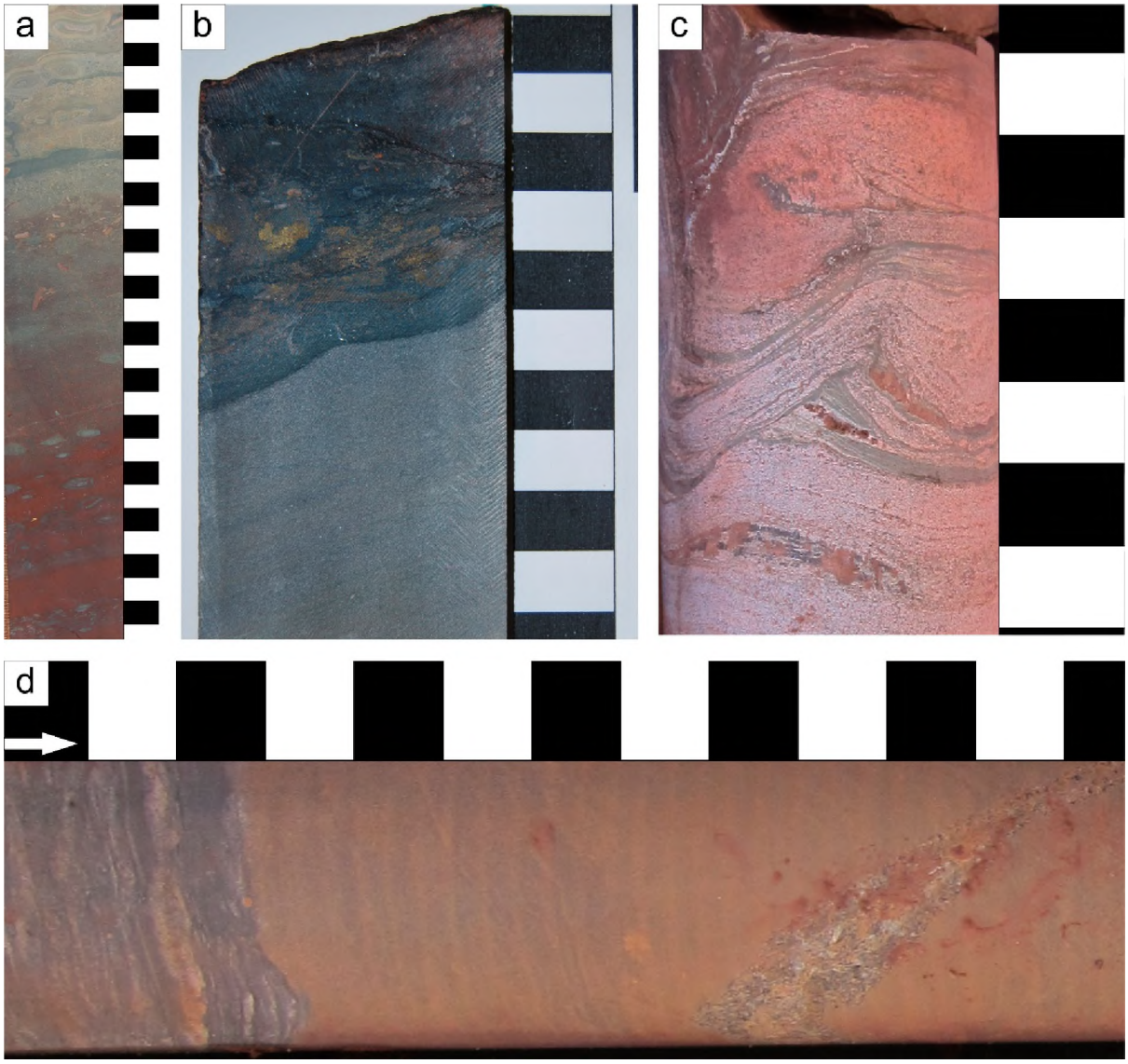

Figure 4.3: Shales located above the conglomerate of the Doornfontein Member. (a) Upward fining red shales fading into green shales hosting green pisoids of varying size. (b) White shales interbedded with black carbonaceous shales. Note the gold coloured pyrite zones and sporadic large lithic fragments hosted in the black shale. (c) Wavy to crinkly black laminae and alumina-rich lenses interbedded with lenticular beds of chert in the aluminous shale unit. (d) Black shale bleached into a cream-coloured alumina-rich shale. A vein sharply cross-cuts the cream coloured bed. Note the intensity of bleaching increases approaching the vein. Arrow indicates way-up direction. Centimetre scale bars attached.

Red Shale Unit

Red shales with millimetre to centimetre scale white to cream bands overlie the ferruginous unit of the Sishen Member and are locally known on the mine as the 'tech' shales. The lithofacies forms a reverse graded laminated unit with alternating red mud and white silt laminae, in which successive silt laminae show a progressive upward increase both in thickness and in grain size until sandy laminae dominate (Figure 4.5a→c). The basal beds of this unit display a mudstone with isolated, cross laminated ripples (see lenticular laminae in Figure 4.5a and white beds in Figure 4.5b. Isolated U-shaped cm-scale depressions are observed sporadically up the sequence and result from a combination of fluid scour and the erosive action of coarser grains within the flow (Figure 4.5b). Flaser lamination characterised by isolated thin drapes of mud amongst the cross-laminae of sand size quartz grains begin to dominate at the top of the sequence (Figure 4.5c). This upward coarsening sequence is capped by the Marthaspoort Quartzite Member.

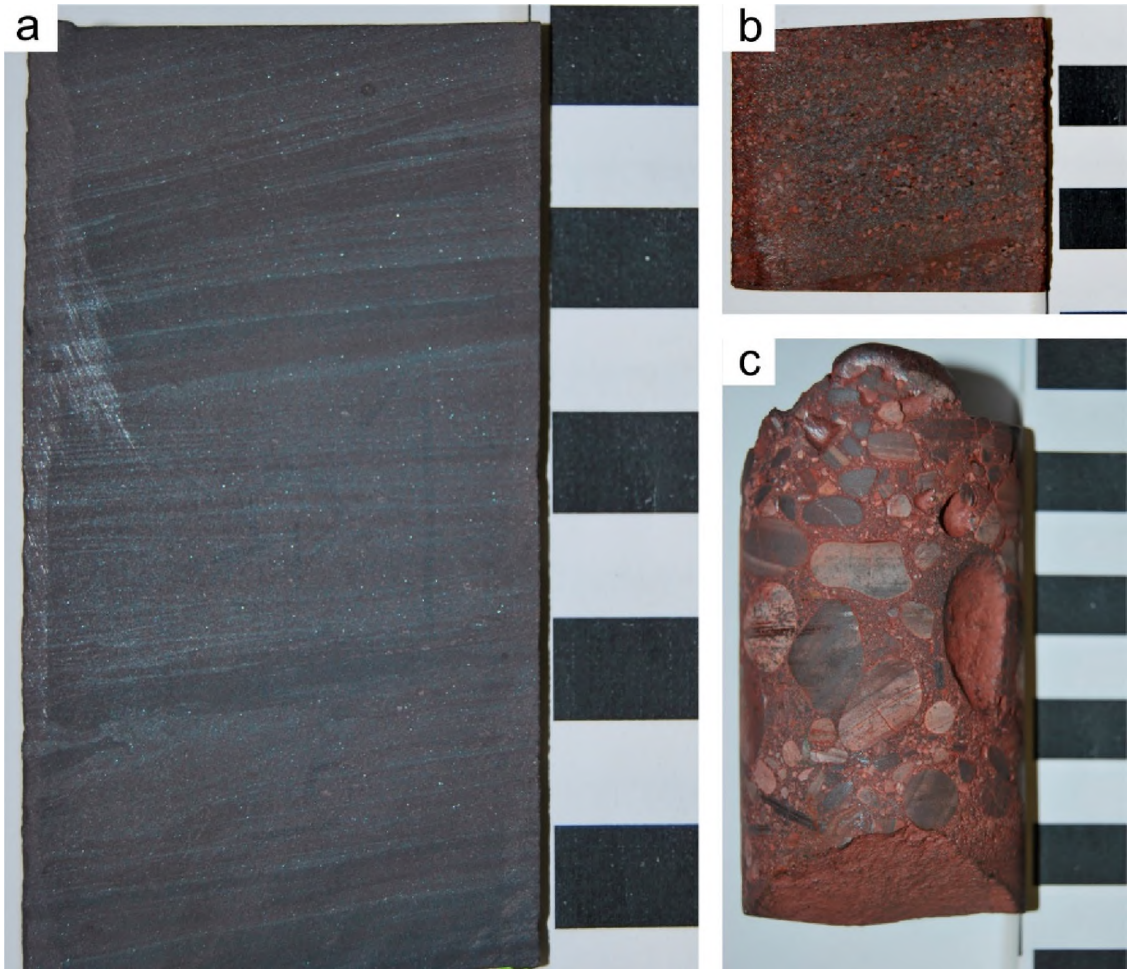

Figure 4.4: The ferruginous units of the Sishen Shale Member as they progressively coarsen upwards from a→c. (a) Hematite-rich quartzite; (b) Gritstone in a hematite matrix; (c) Mature pebble conglomerate formed at top metre of a ferruginous shale unit which may be confused with the Doornfontein conglomerate (core SA2093E). Centimetre scale bars attached.

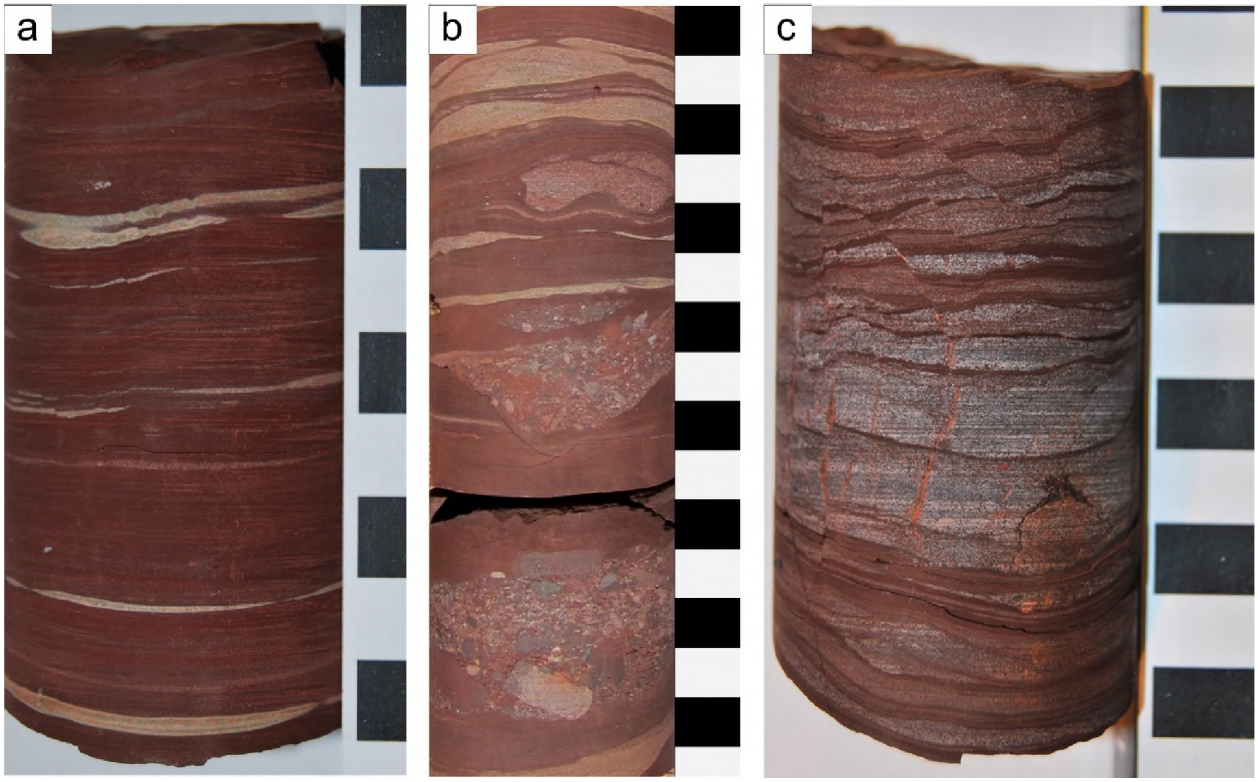

Figure 4.5: Representative samples of the red and white banded shales of the Sishen Member. Upward coarsening is displayed as the silt-to-sand laminae progressively thicken and grain size increases from (a)→(c). Centimetre scale bars attached.

4.2.3. The Marthaspoort Member

The thin flaser laminated mud in the uppermost Sishen shales becomes infrequent amongst a grey to light-purple quartzite (Figure 4.6a). Alternating fine and medium-grained quartz forms cross-laminae observed in the lighter and darker layers of this unit (Figure 4.6a). Progressively, the thin muddy flaser laminations lessen until a pure white quartzite remains (Figure 4.6b). This quartzite is essentially a low-grade metamorphosed ortho-quartz arenite, containing rounded quartz grains cemented by silica. Sedimentary structures are difficult to see in hand specimens of the white quartzite. The quartzite is overlain, usually on a scoured surface by a reverse-graded, gritty-to-coarse-grained quartzite which usually forms the uppermost 50 cm of the Marthaspoort Member (Figure 4.6c). This unit is sharply overlain by the Paling shale Member.

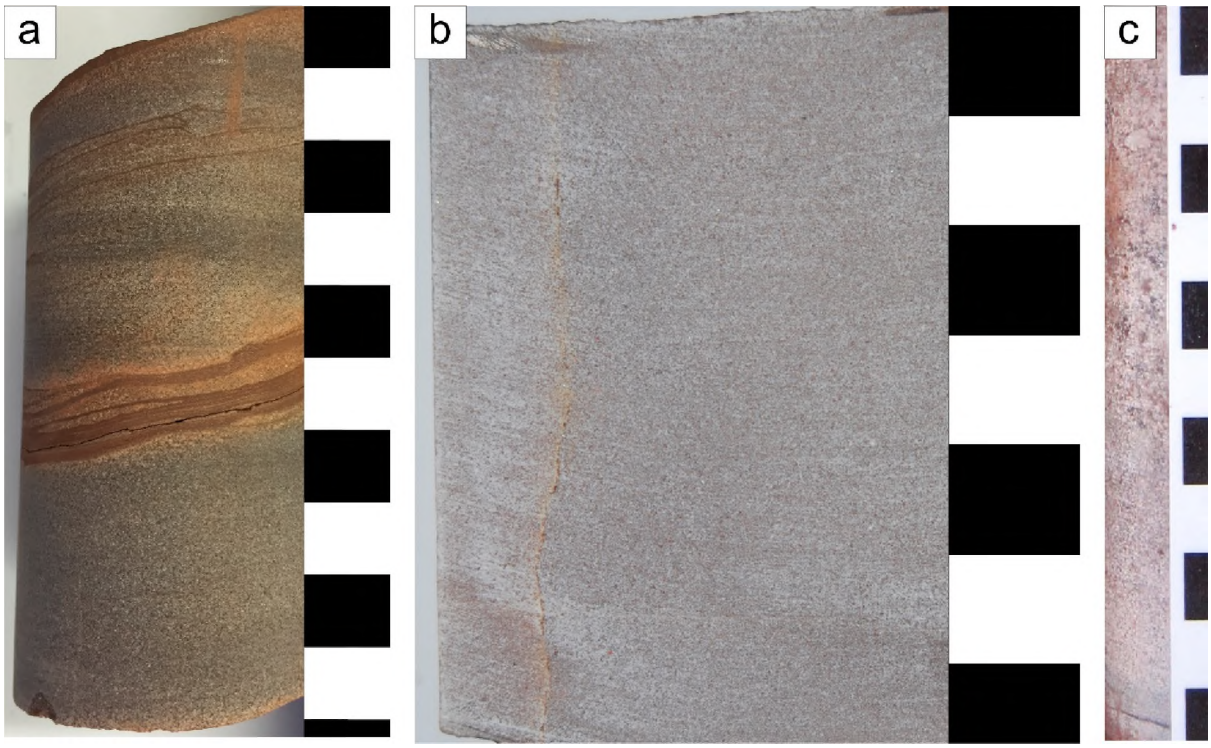

Figure 4.6: The Marthaspoort quartzites as they progressively coarsen upwards from (a)→(c). (a) The grey to light purple quartzite contains infrequent thin drapes of mud. The light purple colouration in this quartzite is from thin hematite coatings surrounding the quartz grains. (b) Pure white quartzites are capped by a reverse graded coarse-grained gritty white quartzite in (c).

4.2.4. The Paling Member

The Paling Shale Member consists of green and red shale beds with horizontal wavy laminations (Figure 4.7). The red shales of the Paling member are easily differentiated by the red shale of the Sishen Member as they are consistently darker in colour (reddish-brown) and are always associated with green shales. The red shales often contain green lenticular wavy laminae (Figure 4.7b) although the inverse of this colouration may also occur. Colours in the paling shale member gradually fade from green to red as seen in Figure 4.7c

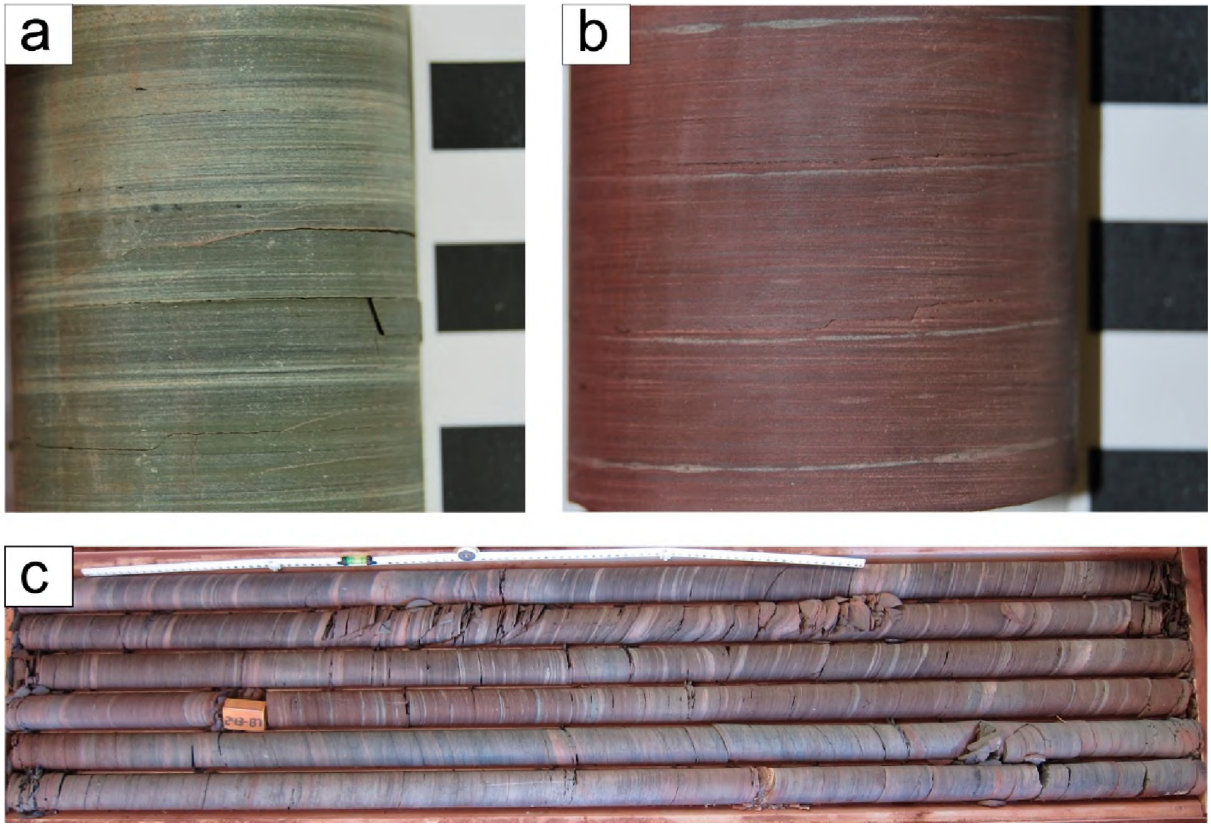

Figure 4.7: The two varieties of the Paling Shale Member. (a) Green shale with thin mud-silt couplets. (b) Red shale with few lenticular green laminae. (c) Core box (1.5m length) displays the fading colouration of the Paling shales.

4.3. Microscopic Observations

4.3.1. The Doornfontein Member

Conglomerates

A thin section of an iron rich conglomerate was examined under reflected light (Figure 4.8). Angular to sub-rounded BIF, chert and hematite pebbles dominate this conglomerate with most grains being entirely ferruginous. Angular to rounded hematite grains look to be comprised of microplatey hematite in varying degrees (Figure 4.8a). Microplatey hematite is also seen in secondary veins which cross-cut BIF pebbles (Figure 4.8b). Such secondary processes are likely to occur in the lower lying iron-formations prior to transport and deposition of the clasts (note the textures terminating at grain boundaries).

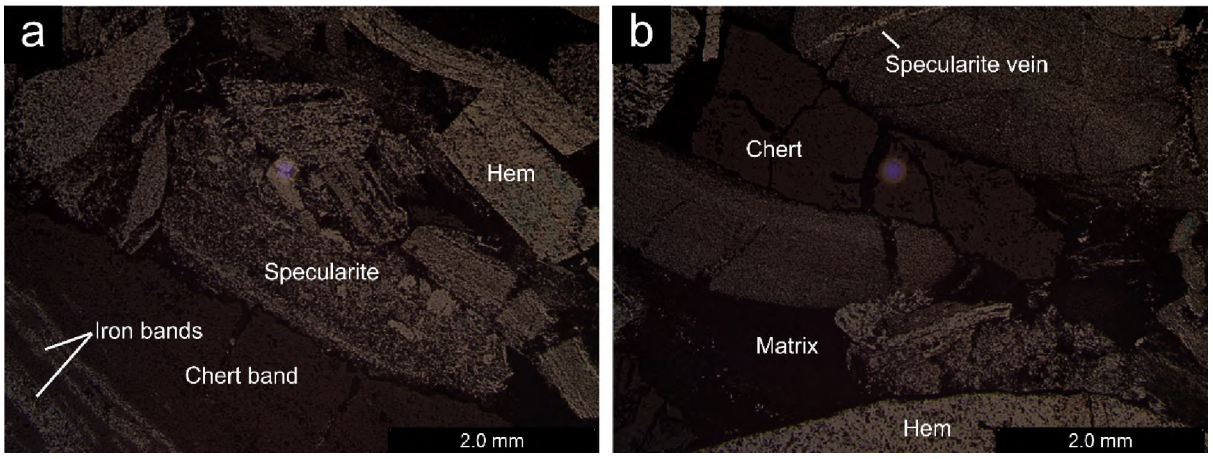

Figure 4.8: Reflected light photomicrographs of a conglomerate in the Doornfontein Member. (a) Rectangular hematite clasts (complete replacement) and a rounded oblong pebble partially replaced by microplatey hematite (specularite). Primary iron and chert bands are also seen in a rectangular BIF clasts. (b) Specularite veins cross cut well-rounded (BIF) pebbles. Rectangular chert clasts are possibly removed from a BIF precursor.

Shales

Thin sections of black shales (Figure 4.9a,b,c) and white aluminous shales (Figure 4.9d) were examined under transmitted and reflected light. The black shales display wavy silt-to-fine-sand laminae containing rounded to sub-angular quartz, chert, pyrophyllite and diaspore grains as well as large rounded chert granules (Figure 4.9a,c). Between these laminae sub-to-euhedral pyrite and rounded pyrite framboids are abundant (Figure 4.9b). Rounded granular chert fragments are sporadically contained in the wavy laminae and to a lesser extent seen isolated in the dark clay matrix. In black shales, lenses (~0.2 mm thick) of pyrophyllite and diaspore are found in close association with wavy black laminae. Pyrophyllite and diaspore is observed rimming quartz and chert grains and can completely replace them (circles in Figure 4.9c). The white aluminous shales contain abundant granular chert with larger rounded granular chert fragments between wavy black laminae. The granular chert fragments are replaced by euhedral grains of muscovite, pyrophyllite and diaspore similar to the replacement found in the black shales, however, on a much larger scale (Figure 4.9d). The texture of the chert granules look strikingly similar to the chert mesobands found in the lower lying iron-formation units, alternatively, they may be reworked granules from the interbedded aluminous shales as abundant granular chert exists in this lithofacies.

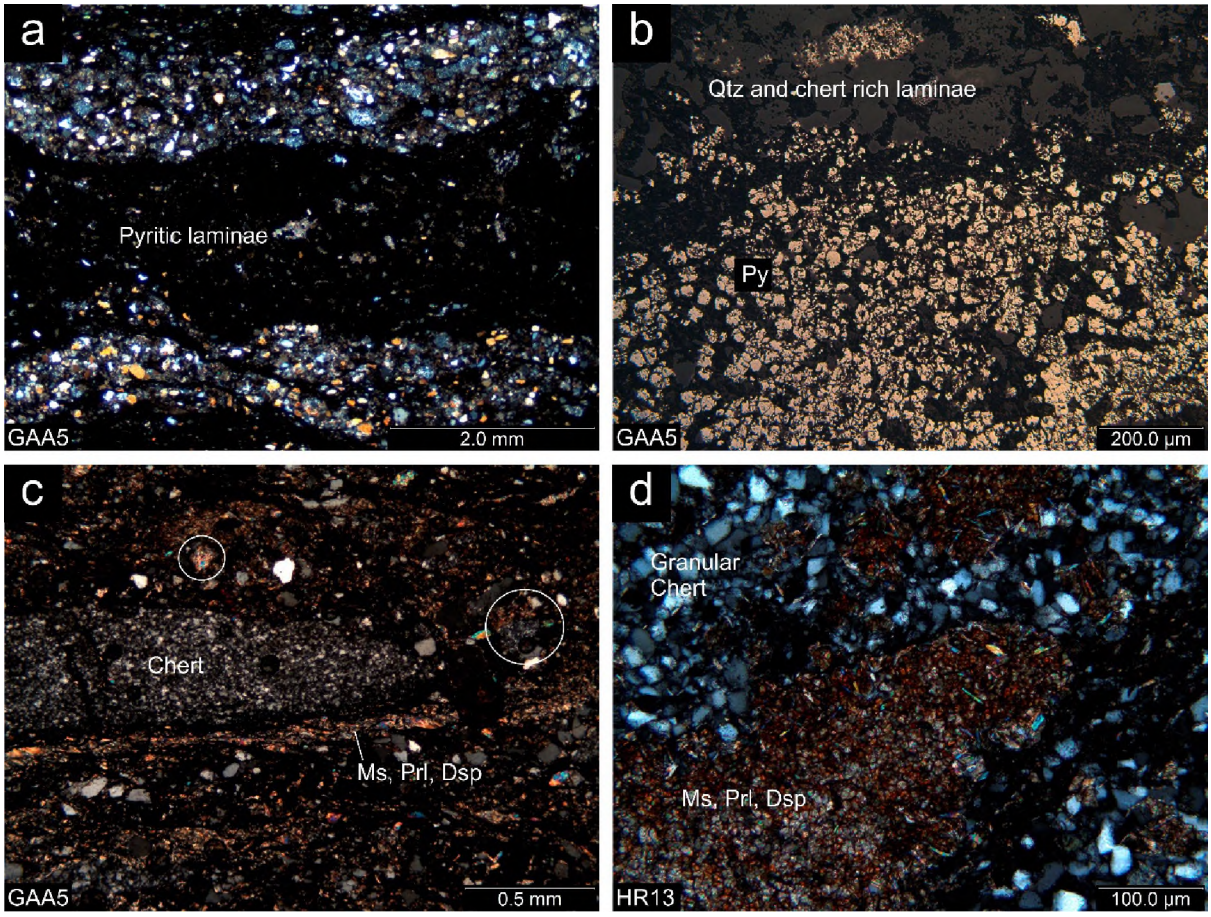

Figure 4.9: Black and white shales of the Doornfontein Member. (a) XPL photomicrograph of a black shale displaying the pyrite laminae between thin wavy silt/sand laminae. (b) Close up reflected light photomicrograph of framboidal and euhedral pyrite grains (Py) in the pyritic laminae seen in (a). (c) A large chert granule in the black shale above a thin lens rich in muscovite (Ms), pyrophyllite (Prl) and diaspore (Dsp). (d) XPL photomicrograph of an aluminous clast surrounded by granular chert in the contorted black shales of core HR4/98. The clast is rich in randomly orientated minerals of muscovite (Ms), pyrophyllite (Prl) and diaspore (Dsp) and displays second to third order interference.

4.3.2. The Sishen Member

Ferruginous Unit

Ferruginous quartzites display low-angle erosion surfaces possibly indicating channel erosion and fill by prograding units (Figure 4.10a). Quartz-rich and hematite-rich lenticular laminae are commonly flanked by wavy iron-rich clays. Sand laminae contain rounded quartz and chert and angular to sub-rounded hematite crystals (Figure 4.10b). Large lithic sand grains (up to 1mm) of chert mesobands identical to those seen in the underlying shale units are found in the sand laminae of the ferruginous quartzites (Figure 4.10d). Relationships between quartz and hematite become intricate under high magnification of the hematite laminae (Figure 4.10c,e,f). Cross-cutting relations, intergrowths and

symplectite textures are observed between hematite and quartz suggesting secondary influences were involved in the creation of the ferruginous unit.

Red Shale Unit

White bands in the red shales of the Sishen Member are typically made of silt to fine-grained sand (Figure 4.11a&b), however, white clay with its own silty to sandy laminae may also feature in the white bands. Hematite fronts are observed replacing the white clay bands, observed by their characteristic red colouration cross-cutting and intruding into it (Figure 4.11c). Primary sedimentary features such as lenticular sand laminae are preserved post ferruginisation (Figure 4.11d). Hematite crystals (opaque in thin section) are observed in the sandy laminae of red zones while none are evident in the sandy laminae of the white bands (compare Figure 4.11e with f). Soft sediment deformation features indicate the deposition of sand on wet mud in a white band (Figure 4.11f).

4.3.3. The Marthaspoort Member

The thin section sampled for the Marthaspoort quartzite was obtained from an upward coarsening red shales from the Sishen Member. The specific cite was in a grey to light purple quartzites with mud laminae as seen in Figure 4.5c. This quartzite is impure and includes well-rounded opaque hematite grains amongst well rounded quartz (Figure 4.12a). Closer to the flaser mud drapes, well-rounded quartz and larger well-rounded lithic granular chert fragments rest in a hematite-rich muddy matrix (Figure 4.12b). These chert fragments are possibly derived from the lower lying aluminous unit, in which abundant granular chert occurs.

4.3.4. The Paling Member

This facies mainly consists of clayey shale with variable amounts of quartz silt. Graded silt-mud and sand-mud lamination dominates the Paling shales (Figure 4.13). Silt occurs as thin (1-2 mm) continuous to discontinuous wavy laminations (Figure 4.13a,b,c). Upper and lower boundaries of the silt laminae are usually sharp but silt/mud couplets are also observed. Thin lenses (~1mm thick) of well-rounded medium-grained sand also occur (Figure 4.13c). Two varieties of quartz grains were identified in the Paling shales (Figure 4.13d).

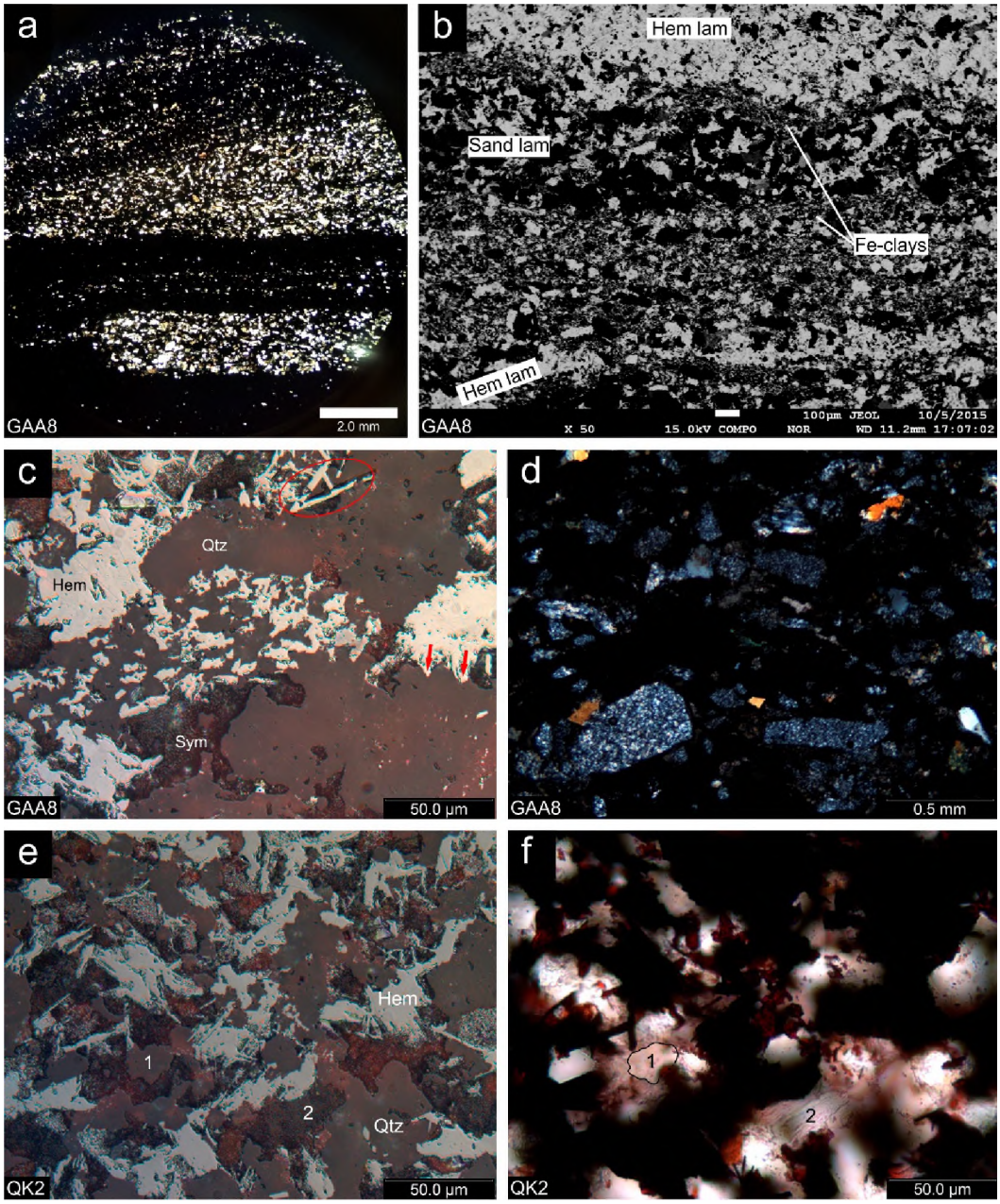

Figure 4.10: Photomicrographs of the ferruginous units of the Sishen Member. (a) PPL photomicrograph of the primary sedimentary structures seen by quartz grains (white in image). (b) BSE photomicrograph of the ferruginous quartzite with white hematite (Hem), sand and clay laminae. Quartz (Qtz) and chert grains are black in this image. (c) High magnification (50x) RL photomicrograph of sandy laminae in a ferruginous quartzite with lobes of quartz and hematite intergrowths in the centre of the image. Note microplatey hematite (specularite) cross cuts a quartz grain (red circle). Outgrowths of hematite indicated by red arrows lobe into the quartz and alter its roundness. Note the symplectite textures (Sym) in areas where quartz and hematite do not directly border one another. (d) Rounded chert mesobands derived either from the underlying iron-formations or reworked granular chert from the lower lying aluminous shales (e) RL and (f) PPL high magnification photomicrographs displaying the same area of a silt laminae in a ferruginous shale. (e) Note a (primary) sub-rounded quartz grain (1) is surrounded by a symplectite texture. Abundant microplatey hematite and quartz-hematite intergrowths occur similarly as in the ferruginous quartzite in (c). (f) A black outline marks the same quartz grain (1), in PPL the grain in surrounded by recrystallized quartz with abundant dusty hematite. Zone 2 of (e) and (f) shows the symplectite texture between quartz and hematite grains.

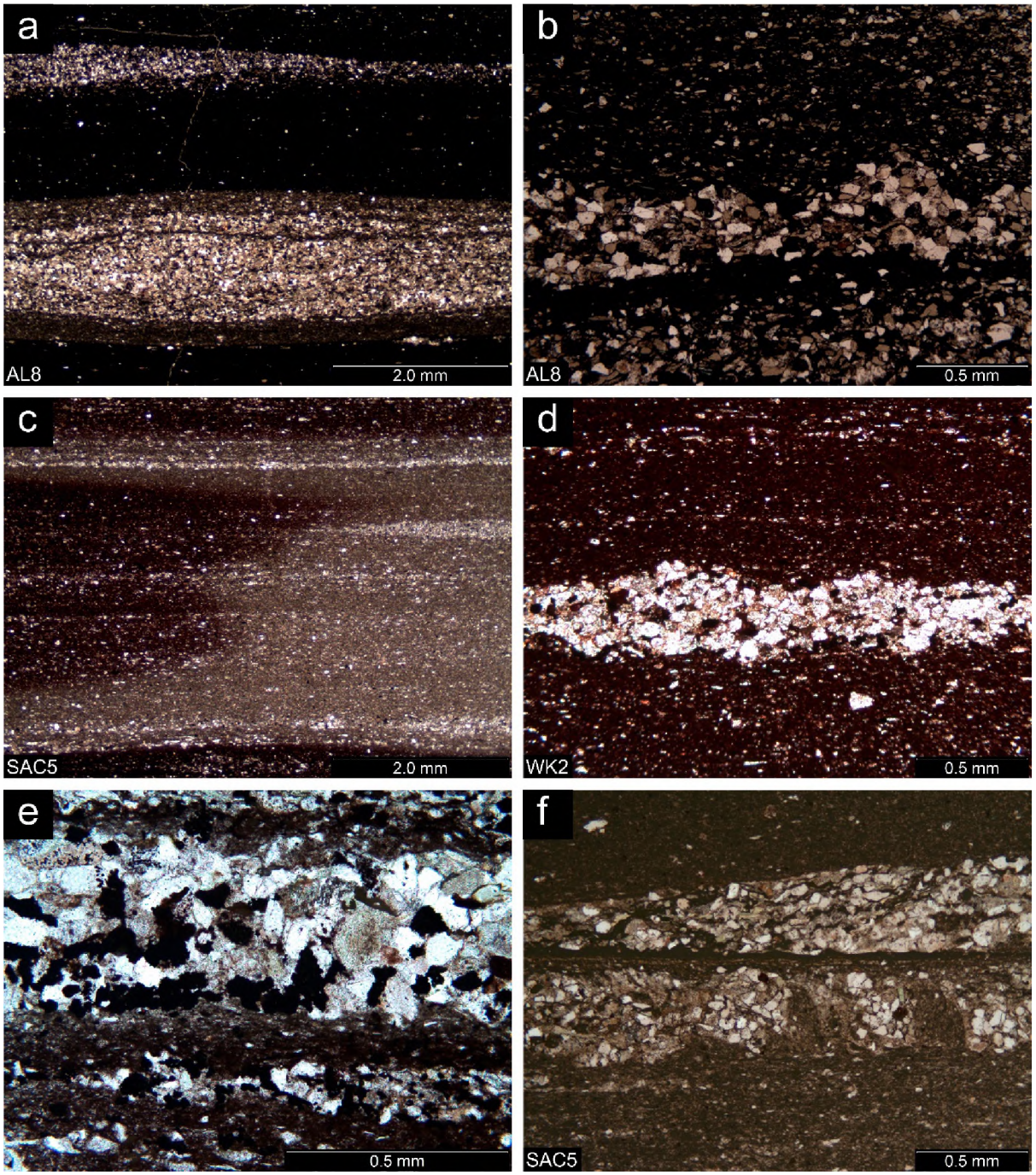

Figure 4.11: Photomicrographs of red and white banded shales of the Sishen Shale Member. (a) PPL image of primary sedimentary features including silty lenticular laminae and silt-mud couplets in a white band of the red shale. Thin dark wavy anastomising laminae are also evident in the white silt layer (b) Two sets, one on top of the other of palimsest ripples preserved in a sand laminae. The base of the upper bed lies on a crinckly-wavy clay surface. Note the silt grains wrapping around the top bed of ripples, eventually smooth out and becoming parallel to the clay layers above. (c) A hematite front cross-cuts a white clay band. (d) Wavy discontinuos lenticular lamination preserved in the hematite front which cross-cuts the white band in (c) Note the wavy-crinkly base of this lenticular laminae. (e) Abundance of opagues in the fine sand laminae of a red band. Note the wavy-crinkly clay laminae flanking the fine-grained sand laminae (f) Load and flame structures at the base of a fine sand lamiae in a white band.

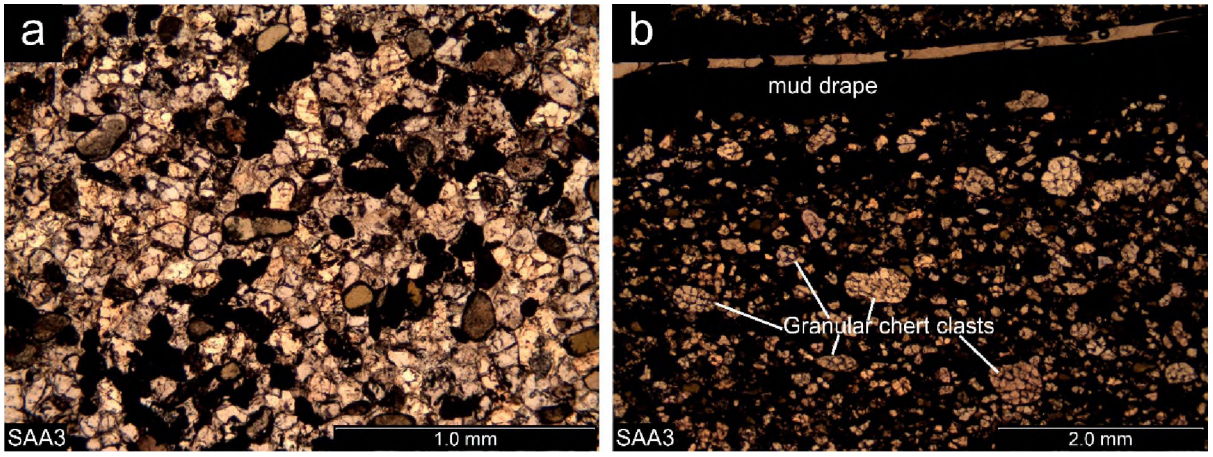

Figure 4.12: Photomicrographs of a grey to light purple quartzite of the Marthaspoort Member. (a) PPL photomicrograph of the grey quartzite showing well rounded quartz and opaque minerals cemented by chert. The quartz is coated by a thin hematite rim which, along with other iron oxides, adds to the light purple hue of these quartzites. (b) PPL photomicrograph of a zone proximal to a flaser mud drape with well-rounded quartz and larger well-rounded lithic fragments of granular chert in a muddy matrix. Note how the sample has cleaved along the less competent mud drape.

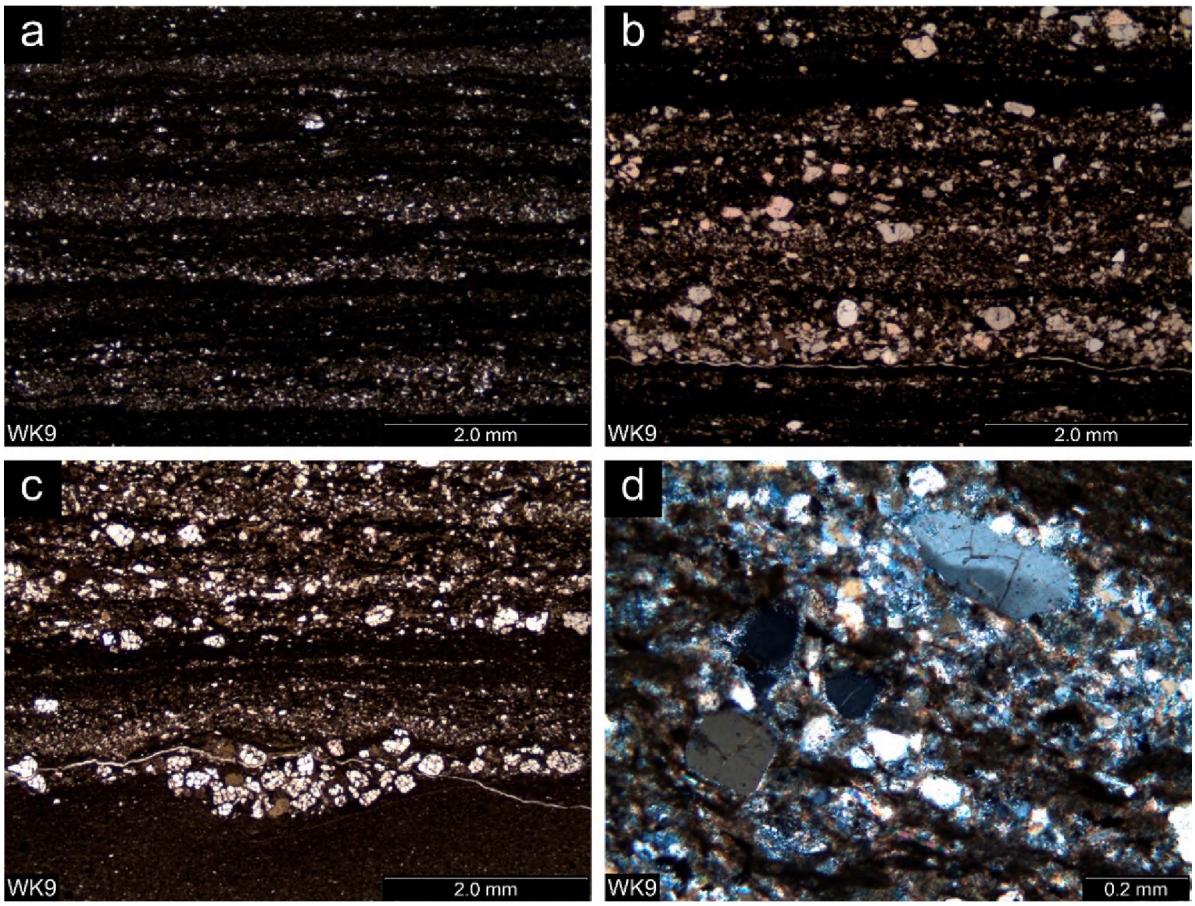

Figure 4.13: Photomicrographs of a green shale from the paling shale member. (a) PPL photomicrograph of continous to discontinous wavy-crinkly lamination comprising individual silt to sand lenses within a fine grained wavy mud unit. (b) PPL photomicrograph of the laminae shows silt and fine-grained quartz. (c) Isolated U-shaped gutter cast due to scour and fill from courser grains within the flow. Perpendicular 'cracks' seen in the larger quartz grains in this section were confirmed to be

due to poor grinding techniques during thin section preparation. (d) XPL photomicrograph confirms two varieties of quartz grains present - those with uniform extinction and those with undulose extinction.

4.4. Mineralogic and Petrographic Summary

Following extensive petrographic examination of 22 representative thin sections the author noted irregular features - most commonly the presence of wavy-crinkly laminae in every shale lithofacies. Schieber (1999) noted that the Proterozoic is the best place to start looking for microbial mat deposits in sandstones and mudstones as its biosphere was dominated by microorganisms. Most of all published microbial mat deposits (stromatolites), albeit in carbonates, come from the Proterozoic as bioturbation and grazing would have had a negative impact on the preserved biomat record in the Phanerozoic.

To this end, and with reference to publications on the topic (Schieber, 1986, 1989, 1998, 1999, 2004; Eriksson *et al.*, 2007) photomicrographs of the Gamagara Formation were examined to understand whether any of the features that serve as microbial mat indicators are present. It must be said that positive identification of a fossil microbial mat requires one to find microbial filaments in life position, a near impossible task in many instances due to the unfavourable preservation of organic matter, however, laminated sediments record the 'trace' that reflects the interaction of the mat community with the environment (Schieber, 1999).

4.4.1. Microbial Mats of the Gamagara Formation

A combination of features highly suggestive of microbial mat influence was recognised in almost all of the shale lithofacies of the Gamagara Formation. An overview of microbial mat features in ancient mudstones are depicted in detail in Appendix E (Eriksson *et al.*, 2007). Features listed and discussed below are extracted from Eriksson *et al.* (2007) and figures numbers will list where such characteristics are present in the shales of the Gamagara.

Wavy-crinkly laminae: Caution must be exercised as wavy laminae can be artefacts of differential compaction around silt lenses and although not a certain indicator of microbial mats, the presence only alerts one to the possibility. Wavy-crinkly laminae are distinctively different from the parallel laminae that form in a mudstone from suspension settling during physical sedimentation processes. Refer to Figure 4.9a,b,c; Figure 4.10a,b; Figure 4.11a,b,d,e; Figure 4.13a,b,c.

Palimpsest ripples: Preservation of successive sets of ripples in sandy sediments, with crests of each set being relatively sharp and un-reworked. Non-amalgamation of two rippled sandstone beds suggests the presence of a mat or biofilm providing organically-mediated sand stabilization, protecting earlier ripples from reworking. Refer to Figure 4.11b,d; Figure 4.14b.

Loaded Ripples: The rippled sandy surface is marked by loading features related to a thin veneer of overlying sand. Loaded ripples form in the absence of algal mats which would provide flexibility and cohesiveness of the lower bed. Such features were absent in the examined thin sections.

Bed-smoothing: Colonisation of irregular sediment surfaces by mats can result in bed-smoothing. In non-mat mudstones, compactional effects above comparable relief are generally detectable for a greater distance upward from the underlying surface irregularity. Refer to Figure 4.11b; Figure 4.13c; Figure 4.14b.

Soft sediment loading: Difference in the behaviour of shales under conditions of soft sediment loading also provides evidence for bed-surface stabilization by a mat cover. As an example, where silt layers have been deposited on mat-bound mudstone surfaces, only minor load features result, whereas miniature ball-and-pillow structures tend to form on non-mat mudstones. Compare Figure 4.11d/Figure 4.13c (microbial mats are interpreted to be present below loading) against Figure 4.11f (microbial mats absent).

Domal buildups: In contrast to the wavy-crinkly carbonaceous laminae discussed above, domal buildups of variable amplitude and spacing have been observed in nearshore mudstones. The inherent rapid weathering of mudstones has likely hampered recognition and preservation of a variety of other, similar occurrences in the rock record. Refer to Figure 6.2a – Domal buildups occur on top of the thin clay laminae.

Overfolded mat layers and 'roll-up' structures: Mat-bound mud layers display 'within layer' cohesiveness when eroded and transported as well as a different rheological quality when compared to 'normal' mud layers. Common structures includes anastomosing laminae and grain rafting (grains rafted in by floating mat fragments). Refer to Figure 4.11a; Figure 4.14a,d.

Torn mats and mat fragments: Commonly display frayed edges, sometimes called the 'blotting paper effect' in modern mats. Refer to Figure 4.14c.

Pyritic laminae: When anaerobic decay of organic matter occurs beneath a growing mat, favourable conditions occur for precipitation of 'anoxic' minerals like pyrite. Within marine settings, hydrogen sulphide commonly forms beneath the mat, and pyrite will crystallize. Depending on the amount of iron available in the environment, manifestations in the rock record may range from carbonaceous material

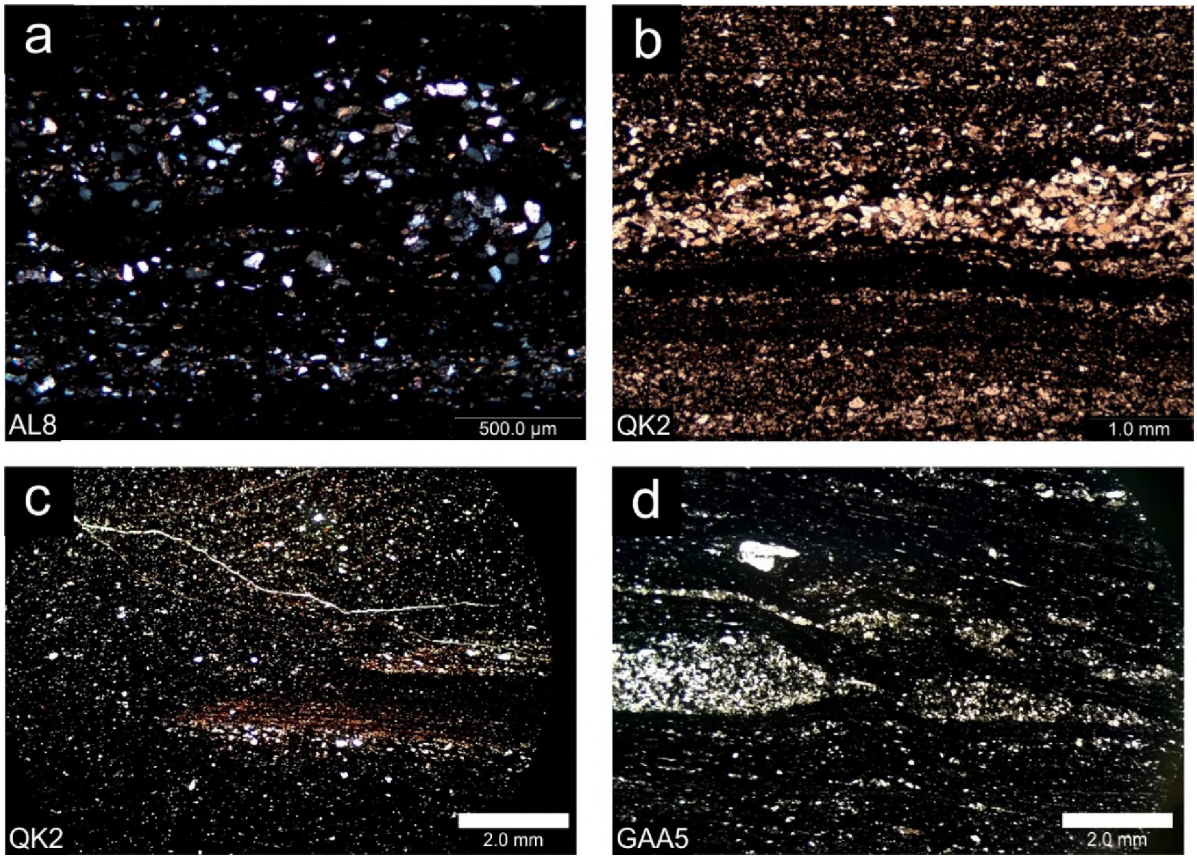

Figure 4.14: Addition images for microbial mat features as discussed above include (a) grain rafting, (b) palimpsest ripples and bed smoothing, (c) torn mat fragments and (d) anastomosing laminae with overfolded mat layers.

dusted with pyrite grains to strongly pyritic laminae that essentially mimic the wavy-crinkly mat lamination. During early diagenesis, pyrite overgrowth and cementation of the original fine-grained pyrite may occur. Refer to Figure 4.9a,b.

In none of the above examples of possible microbial mat occurrences have microfossils been found that were orientated or organised in such a way indicative of organosedimentary interaction and therefore, strictly speaking, one cannot assign a microbial mat origin to them (Schieber, 1998). Nonetheless, the large number of features that indirectly point to microbial mat development, mostly reported from modern microbial mats, are available (Schieber, 1998). Differences in relative abundance of various features between lithofacies are likely a consequence of changes in depositional settings and environmental parameters (i.e. water depth, sedimentation rate, sand/silt/clay ratio and size of the water bodies).

4.4.2. Fe-addition

The sudden increase in hematite in the Fe-rich shales/quartzites of the Sishen Member is interesting. This unit is found to contain up to 65 wt. % Fe_2O_3 and may form part of the iron ore body where it meets grade. It has previously been described as syn-sedimentary with speculation of Fe addition from supergene and/or metamorphic influences (Schalkwyk, 2005). In this thesis secondary Fe input is identified in both the ferruginous unit (Figure 4.10c,e) as well as in cross-cutting bands in the overlying Sishen red shales (Figure 4.11c). For this reason, further investigation was carried out during geochemical analysis and is reported in **section** 5.5.3.

4.4.3. Titania Anomaly

On comparing shales of the Gamagara to post-Archaean Australian shales (PAAS; Taylor and McLennan, 1985), previous studies noted enriched levels of TiO_2 in bulk rock geochemical data sets (Van Schalkwyk and Beukes, 1986; Yamaguchi and Ohmoto, 2006; Kalumbu, 2006; Land et al, in review). The XRD data set in this study included four samples of red and white banded shales in order to determine the units' modal mineralogy. It was found that the approximate averages for rutile/brookite/anatase (herein referred to as titania) and ilmenite are 2.85% and 1% by volume respectively (Figure 4.1). In order to investigate the modes of occurrence, EPMA analyses complimented by reflected light microscopy was carried out. Focus was placed on the red shales of the Sishen Member using samples where the highest levels of titania (TiO_2) and ilmenite ($FeTiO_3$) existed (see section 4.5).

4.5. Mineral Chemistry

4.5.1. Analytical Procedures

EPMA data acquisition was performed at Rhodes University, Department of Geology, on a Jeol JXA 8230 Superprobe, equipped with four WD spectrometers. Analytical conditions employed for quantitative analyses was as follows: 15kV acceleration voltage, probe current 20 nA, spot beam size ~1 micron, counting times of 10 seconds on peak and 5 seconds on background with the exception of chromium (20 seconds on peak, 10 seconds on background). The standards used for quantification of oxides were: kyanite (Si), chrome-diopside (Ca), periclase (Mg), spinel (Al), cubic zirconia (Zr), lithium niobate (Nb), rhodonite (Mn), chromium oxide (Cr), hematite (Fe), plagioclase (Na), vanadium (V), and rutile (Ti). The standards were used for quantification of apatites were: dolomite (Ca and Mg), monazite (P), cubic zirconia (Zr), magnesium fluoride (F), rhodonite (Mn), biotite (K), hematite (Fe),stronitum titanate (Sr), albite (Na), and tugtupite (Cl). The ZAF matrix correction method was used for quantification. Analytical conditions employed for the qualitative analyses and elemental maps was as follows: acceleration voltage 15 kV, probe current 20 nA, 0 μm probe diameter, dwell time of 10ms, and stage scan mode.

4.5.2. Titania

Referring to Figure 4.15 – Figure 4.17, four different modes of occurrence of titania were identified as follows: (T1) Angular to rounded grains (detrital; 10-20μm) which contain an internal framework texture (fibrous or patchy); (T2) small blebs (generally ≤5μm) usually in a network structure; (T3) Angular to rounded grains with no texture (generally 5-20μm); and (T4) crystals that replace quartz grains (10-30μm).

T1 Framework grains: Grains which give a mixed Fe-Ti signal in the element maps display framework textures shown by variations in backscatter electron intensity. These may be in the form of patchy (Figure 4.15) or a more ordered trellis-like structure (Figure 4.17). Trellis-like structures may be preservation of original igneous textures, in this instance titanomagnetite (Pe-piper, 2005). In both examples of the framework grains there is evidence for titania crystallizing as local alteration products of Fe-Ti-bearing minerals (primarily ilmenite).

Table 4.1: Electron microprobe analyses (wt. %) of titania replaced quartz grain (refer to Figure 4.16b for points)

Point	1	2	3
SiO_2	31.88	35.55	0.39
CaO	0.10	0.10	0.27
MgO	0.02	0.01	0.03
Al_2O_3	0.70	0.36	0.11
ZrO_2	0.68	0.71	0.76
Nb_2O_5	0.37	0.52	0.31
MnO	b.d.	0.04	0.05
Cr_2O_3	b.d.	b.d.	0.00
FeO	0.36	0.38	0.28
TiO_2	63.94	60.29	97.07
V_2O_3	b.d.	b.d.	b.d.
Total	**98.05**	**97.95**	**99.27**

b.d: below detection limits

Network T2 grains: Referring to Figure 4.15, networked titania blebs are suggested to form by the complete dissolution of Fe in T1 framework grains. This may occur by further leaching of hematite and co-precipitation of titania, eventually leaving behind the network of blebs (grey in BSE image), some of which are still connected to minor amounts of remnant hematite (white in BSE). These blebs act like fluids and almost always 'flow' to fill intergranular pore spaces parallel to planes along which phyllosilicates and micas occur. Note the Fe map highlights such planes as hematite coats the phyllosilicates which ultimately imparts the red colouration to the shale. Interestingly, zircon is also found to occur similarly to the T2 habit in Figure 4.15.

Small subhedral to euhedral T3 grains: Grains with pure Ti signals (partly cut off grain at the bottom of the Figure 4.15) show no compositional variations in backscatter electron intensity, are suggested to be primary detrital rutile grains. Some of the smaller crystals ($\leq$5µm) may have a euhedral habit, however, higher magnification and better imaging resolution is required to determine whether they are in fact recrystallized grains of titania, possibly growing in pore spaces, or if they are simply the fragments of a larger grain broken up during transport.

T4 Titania replacing quartz: Referring to Figure 4.16 and Table 4.1 - titania overgrowths occur on an original detrital quartz crystal. The textures shown in RL and BSE look patchy, similar to the T1 framework grains. Note the brightest zone in the BSE image indicate zones with highest Ti content occur around the rims of the grain. This is confirmed by Table 4.1 (point 3 at the rim with 97% TiO_2 and 0.39% SiO_2). The data also shows the control titania has on HFSE's such as Nb and Zr.

4.5.3. Fluorapatite

In all instances, authigenic titania occurs close to or together with authigenic fluorapatite (Figure 4.15 and Table 4.2). In the case where titania forms along cleavage planes (T2 textures) fluorapatite was found to coexist along the same planes. The presence of such a mineral may have important implications on the fluids that carried the HFSEs in the Sishen red shales and emphasis will be placed on this unit in the following sections.

Table 4.2: Electron microprobe analyses (wt.%) of fluorapatite ($Ca_5[PO_4]_3F$) found in close proximity to titania minerals.

Point	QK3_1	QK3_2	QK3_3	QK3_4
CaO	56.904	55.635	55.803	55.996
Na_2O	0.000	0.000	0.000	0.000
MnO	0.000	0.000	0.000	0.071
FeO	0.298	0.318	0.304	0.260
K_2O	0.081	0.061	0.051	0.061
ZrO_2	0.000	0.021	0.047	0.000
MgO	0.026	0.051	0.053	0.060
SrO	0.246	0.293	0.281	0.529
P_2O_5	41.203	41.223	41.529	40.661
Cl	0.032	0.000	0.041	0.057
F	3.563	3.782	2.863	2.563
Total	**102.353**	**101.384**	**100.972**	**100.258**
Formula units (13 O,OH,Cl,F)				
Ca	5.121	5.032	5.067	5.140
Na	-	-	-	-
Mn	-	-	-	0.005
Fe	0.021	0.022	0.022	0.019
K	0.009	0.007	0.006	0.007
Zr	-	0.002	0.004	-
Mg	0.007	0.013	0.013	0.015
Sr	0.024	0.029	0.028	0.053
P	2.930	2.946	2.980	2.949
Cl	0.005	-	0.006	0.008
F	0.946	1.010	0.767	0.694
OH	0.049	-	0.227	0.297

b.d.: below detection limits

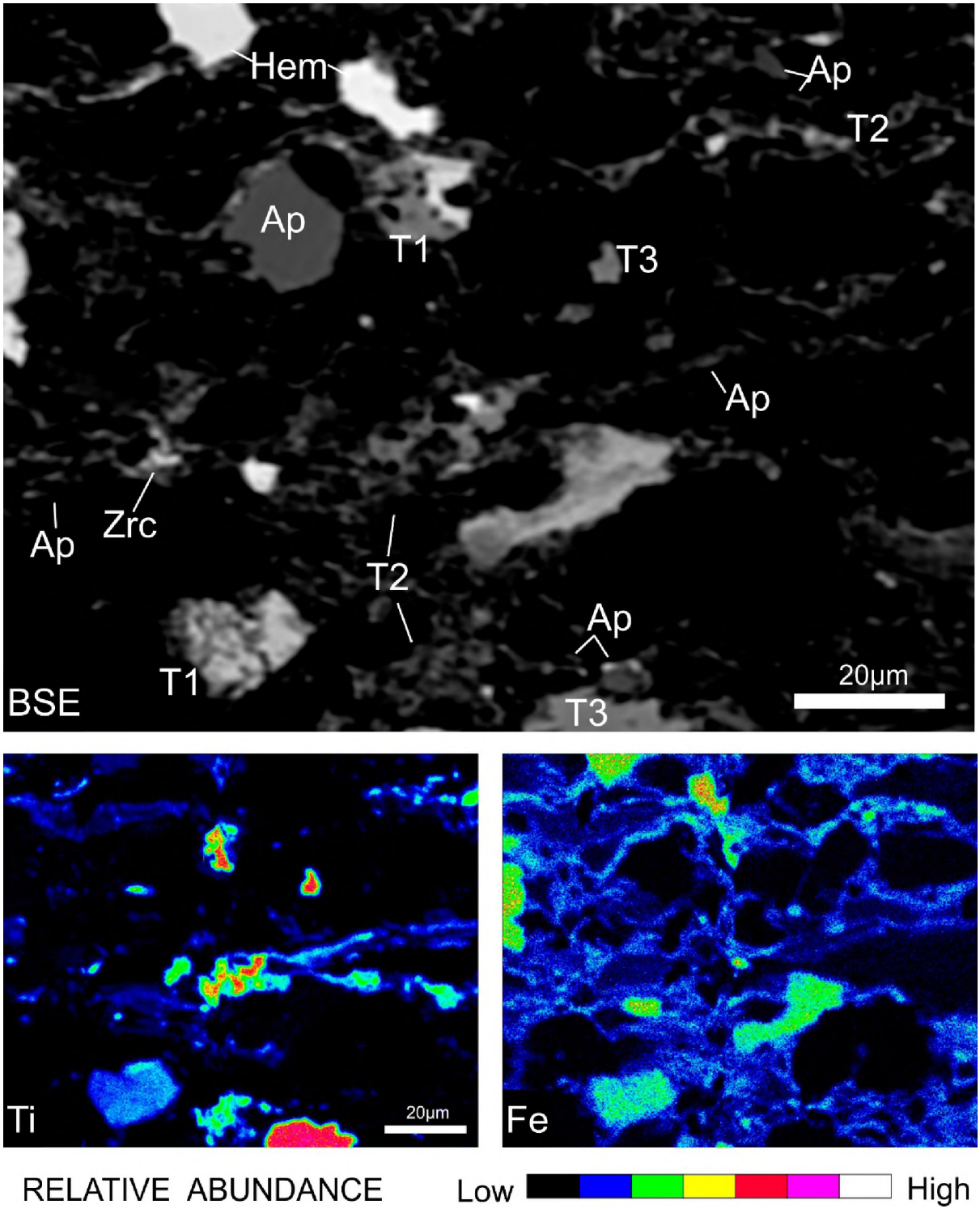

Figure 4.15: BSE photomicrograph and corresponding EPMA element maps showing chemical variation in Ti and Fe content. Surrounding minerals in BSE image are black because an exaggerated contrast was used. T1-T3 point to the various titania minerals as explained in-text. *In situ* hematite exsolution and authigenic titania precipitation occurs at the expense of ilmenite in T1 minerals with patchy texture (note the Fe and Ti contents). Ap=Fluorapatite; Hem=Hematite; Zrc=Zircon.

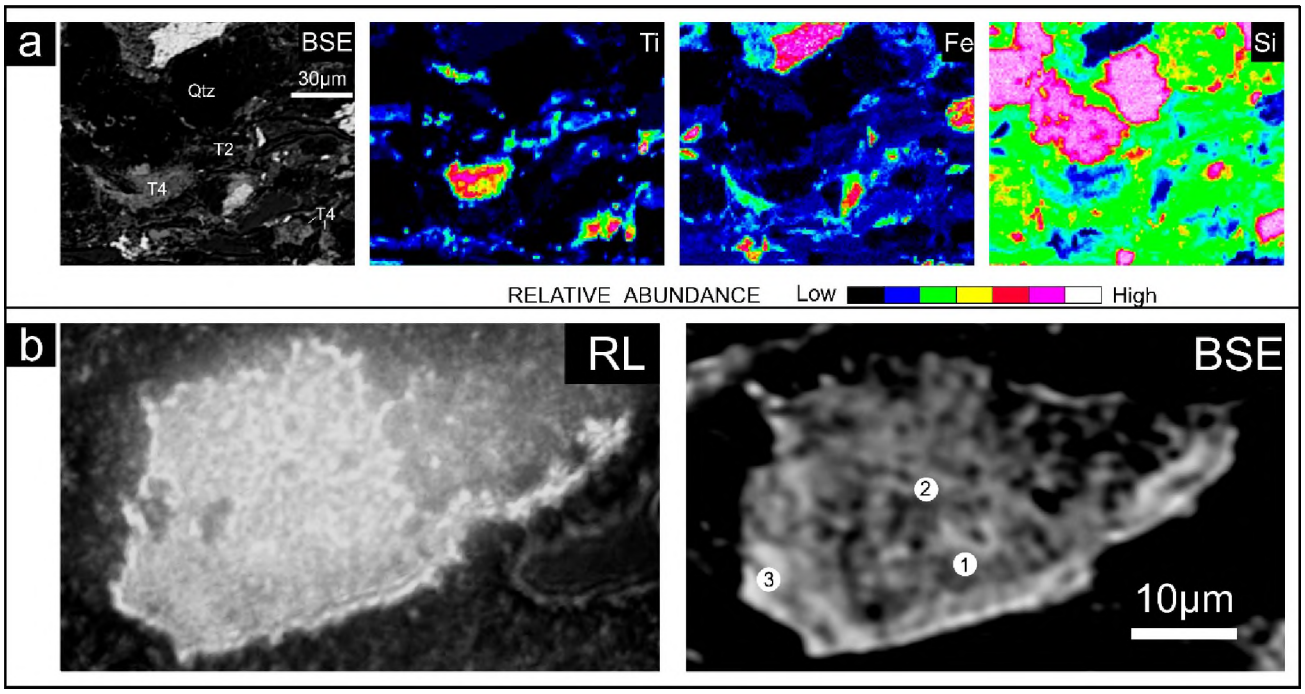

Figure 4.16: BSE photomicrograph and EPMA element maps showing chemical variation in Ti, Fe and Si content along with high magnification images of the replaced quartz grain. (a) Three T4 grain are present in this sample. Note the abundance of Ti and Si and the complete lack of Fe in the T4 grains. T2 grains are also present in the sample proximal to the large T4 grain. (b) High magnification RL and BSE photomicrograph of titania replacing quartz. This mineral was investigated after it was noticed in a large area element maps shown in Appendix D.

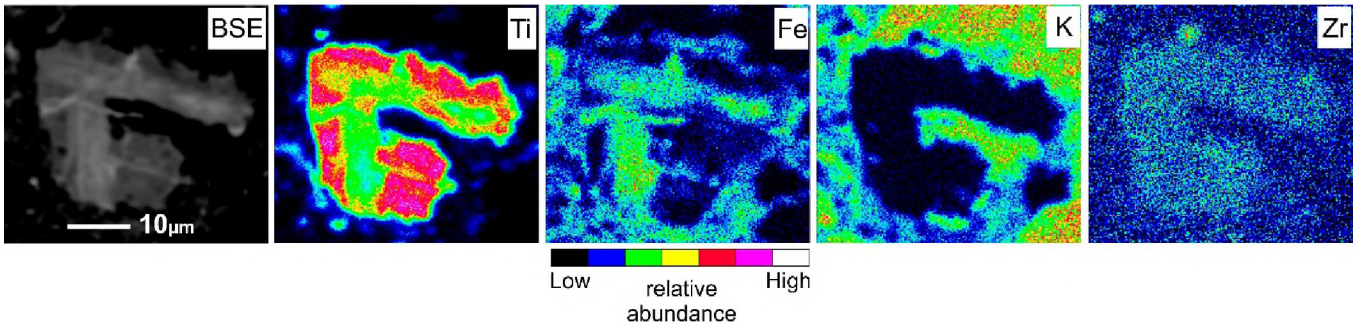

Figure 4.17: BSE photomicrograph and complimentary EPMA element maps showing chemical variation in Ti, Fe, K and Zr content in a framework grain. This grain presumably developed from a titanomagnetite precursor, in which ilmenite exsolution occurred. Upon burial diagenesis and mobilization of TiO_2, grain margins were replaced with titania.

5. WHOLE-ROCK GEOCHEMISTRY

5.1. Analytical Procedures

5.1.1. Major and Trace Elements

Major and trace element oxides were obtained using XRF at two laboratories following the decommissioning of the XRF at Rhodes University in January 2015. Samples obtained from Beeshoek, King and Bruce mines were analysed on a Philips PW 1480 XFR spectrometer housed in the Department of Geology, Rhodes University. Whole-rock analytical data for ten major element oxides and sixteen trace elements were determined using the methods outlined by Norrish and Hutton (1969). Major element (except Na_2O) analyses were obtained from fused lanthanum-bearing lithium borate glass disks whereas the trace element and Na_2O analyses were obtained from pressed powder pellets. Sampled obtained from Sishen were analysed on a Panalytical Axios XRF spectrometer housed in the Department of Geological Sciences at the University of Cape Town, South Africa. Routine analysis of Fe, Mn, Ti, Ca, K, S, P, Si, Al, Mg and Na were determined using fused disks prepared with lithium borate flux. Trace element concentrations were measured on pressed powder briquettes and intensity data were corrected for mass absorption/enhancement and spectral interferences with international rock standards used for calibration. Tabulated results can be found in Appendix A.

5.1.2. Rare Earth Elements

A geochemically representative subset of 37 samples were analysed across the Gamagara Formations' stratigraphy for REE data. The analyses were performed on a Thermo-Fisher X-Series II quadrupole ICP-MS, housed in the Department of Geological Sciences, University of Cape Town, South Africa. 50 mg of sample powder were dissolved in a 4:1 HF/HNO_3 acid mixture in sealed Savilex beakers and placed on a hotplate for 48 hours at 50-60°C. Once fully digested, beakers were opened and samples evaporated to incipient dryness. Following this, two treatments of 2 mL concentrated HNO_3 with total evaporation on the hotplate were completed. Quantitative element measurements in solution mode were performed via calibration using internal multi-element synthetic certified standard solutions (samples were diluted 5000-fold in 5% HNO_3 solution containing 10 ppb Re, Rh, In and Bi). Precision, accuracy and detection limits were determined through the analysis of USGS rock standard BHV02-a, as well as procedural blanks, processed with every sample batch. Reported Ce, Eu or Pr anomalies are calculated using the geometric mean as recommended by Taylor and McLennan (1985). Tabulated results can be found in Appendix B.

5.1.3. Nd Isotopes

Eight samples, including 5 from the Sishen Members' red shales and 3 from the Paling Members' green shales were analysed for Nd isotope ratios. These samples were obtained across three drill cores (ALK3/22, WK4/25 and QK4/89) located on King Farm. A further two samples from the Mapedi Formation were also analysed for comparative purposes (drill core N99 obtained from the study of Land *et al.*, in review). Neodymium isotope analyses were performed on a Nu Instruments NuPlasma HR in the MC-ICP-MS facility, housed in the Department of Geological Sciences, University of Cape Town, South Africa. Powdered samples were digested in a mixture of concentrated HF and HNO_3 for 48 hours at 140°C in closed Teflon beakers, subsequently dried down and converted to nitrate complexes. The Nd fractions were isolated using Eichrom Ln.Spec resin after Míková & Denková, 2007. Nd isotopes were analysed as 50ppb 2% HNO_3 solutions using Nu Instruments DSN-100 desolvating nebuliser. Tanaka's (2000) reference standard JNdi-1 was used with a $^{143}Nd/^{144}Nd$ normalizing value of 0.512115. Nd isotope corrections were done for: (1) Sm and Ce interference using the measured signal for ^{147}Sm and ^{140}Ce along with natural Sm and Ce isotope abundances and; (2) instrumental mass fractionation using the exponential law and a $^{146}Nd/^{144}Nd$ value of 0.7219.

Calculations for the results found in Table 5.1 follow the methods of DePaolo (1988) and Faure and Mensing (2005) as outlined in this paragraph. Following 'bulk planet' evolution curves for $^{143}Nd/^{144}Nd$, their reference values are those that would be found in a reservoir that has had a Sm/Nd ratio equal to that of the average chondritic meteorite. This standard reservoir has been referred to as CHUR (Chondritic Uniform Reservoir). Following the normalisation of $^{146}Nd/^{144}Nd = 0.7219$, a value of 0.512638 is used to represent the ratio of CHUR at present time $(^{143}Nd/^{144}Nd)_{CHUR}$. From this, ε_{Nd} values are derived by deviation of the $^{143}Nd/^{144}Nd$ value of the sample from that of $CHUR^{(t=o)}$ in units of parts in 10^4. Depleted mantle model ages, referred to as T_{DM}, are used to signify the importance of crustal involvement in continental magmatism and are calculated using average 'depleted mantle' evolution curves.

5.2. PAAS-Normalization

In a comprehensive detrital zircon study, Van Niekerk (2006) found that the catchment area for where he placed the Gamagara/Mapedi Formation (see section 1.3.1) was Paleoproterozoic with minor Neoarchean contributions. REE profiles from Paleoproterozoic shales are distinct from Archaean counterparts in that a compositional shift is suggested due to a major period of growth and differentiation of continental crust at ~2.6 Ga (Taylor and McLennan, 1985). Based on this, the study

approaches the geochemistry of the Gamagara Formation shales using PAAS as average reference values for the original precursor sedimentary package after large scale mixing and possibly recycling.

5.2.1. Major Elements

Variations in PAAS-normalized major element oxides with corresponding tables of their averaged weight percentages (including error and range) through the major lithofacies of the Gamagara are made available in Figure 5.1. In almost all units, the shales predominantly consist of SiO_2, TiO_2, Al_2O_3, Fe_2O_3 and K_2O (see corresponding tables in Figure 5.1). With the exception of K_2O, the low field strength elements Na_2O, MgO and CaO show strong to moderate depletion values through the entire Gamagara stratigraphy.

Aluminous shales have enriched values of TiO_2 and Al_2O_3 (average of 1.7 times and 1.8 times PAAS respectively), moderate depletions in Fe_2O_3, K_2O and P_2O_5 and strong depletions in all other major elements. SiO_2 and Al_2O_3 of the black shales fit close to that of PAAS with minor enrichments in TiO_2 and Fe_2O_3, however note the high standard deviation and range for Fe_2O_3. Depletions in all other major elements occur in the black shale unit.

Ferruginous shales have a considerable enrichment in Fe_2O_3 with an average of 6.5 times (maximum 11 times) that of PAAS. Minor depletions in SiO_2, TiO_2, Al_2O_3 and MnO with strong to moderate depletions in the low field strength elements (LFSE) occur in the ferruginous shale unit. The red shales of the Sishen Member have considerable enrichments in TiO_2, Fe_2O_3 and P_2O_5, while K_2O shows a moderate enrichment. The remaining elements in this unit show moderate to strong depletions.

Shales/quartzites of the Marthaspoort Member were sampled in the transitional upward coarsening sequence, as such they capture the quartzites interbedded with the red shales. With higher quartz input in the sequence, a corresponding relative enrichment in SiO_2 occurs. The red shales influence is seen with enriched Fe_2O_3 content along with signatures of only moderately depleted Al_2O_3, TiO_2, K_2O and P_2O_5. Pure quartzites of Marthaspoort consist of ca. 98 wt. % SiO_2 (Kalumbu, 2006).

The green and red shales of the Paling Member have values similar to that of PAAS for SiO_2, TiO_2, Al_2O_3 and Fe_2O_3 with moderate enrichments in K_2O and P_2O_5. Moderate depletions in MnO and MgO and strong depletions in CaO and Na_2O occur in the Paling Member.

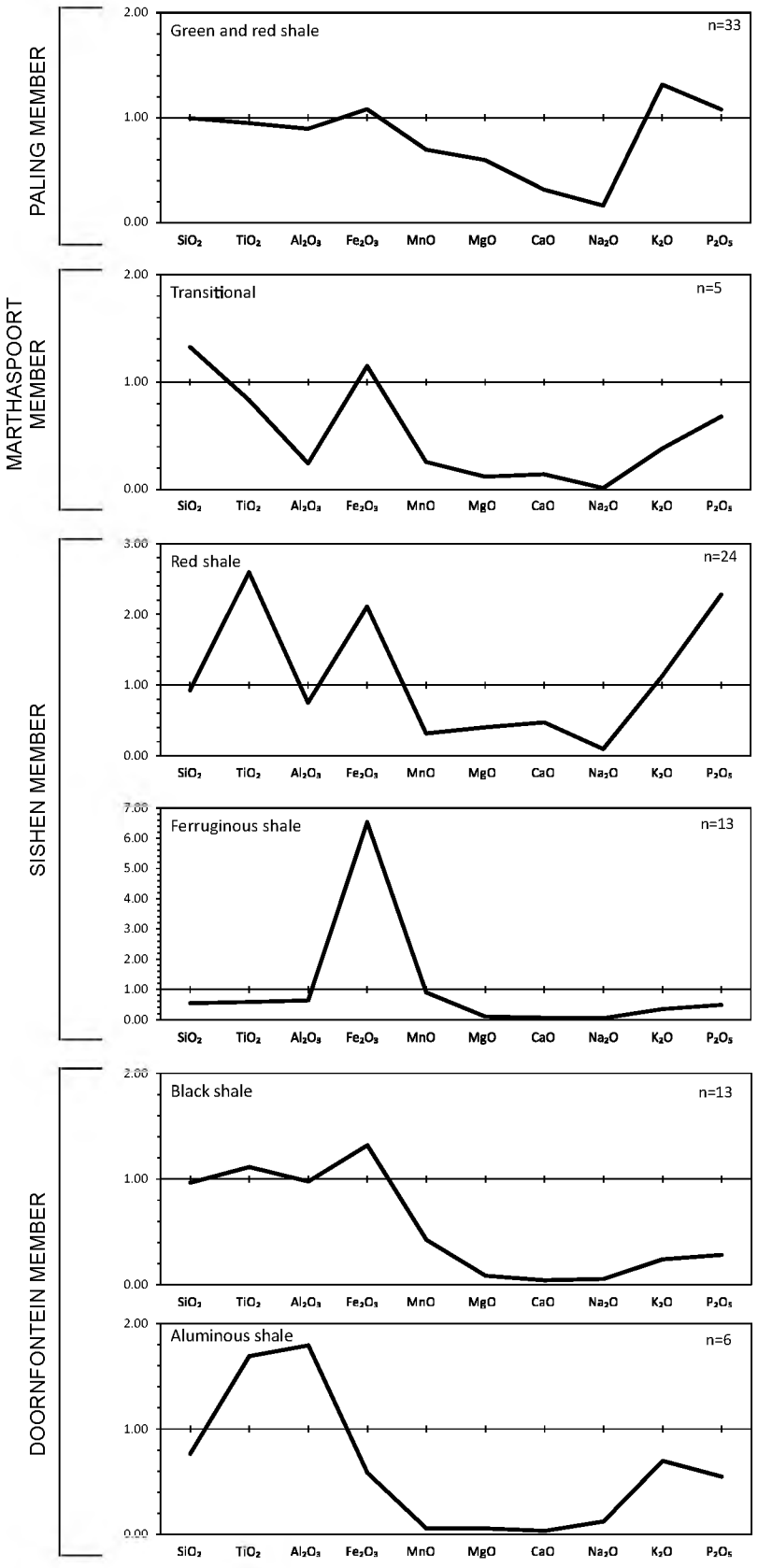

	Ave.	St. Dev.	Min	Max
SiO_2	62.46	3.94	53.26	68.68
TiO_2	0.95	0.22	0.54	1.43
Al_2O_3	16.89	2.18	11.23	20.84
Fe_2O_3	7.78	3.19	2.61	14.50
MnO	0.08	0.14	0.01	0.84
MgO	1.31	0.40	0.67	2.04
CaO	0.41	0.75	0.08	4.22
Na_2O	0.19	0.18	0.05	0.65
K_2O	4.87	0.95	2.97	6.82
P_2O_5	0.17	0.21	0.03	1.04
LOI	4.08	1.08	2.87	6.86

	Ave.	St. Dev.	Min	Max
SiO_2	83.29	6.94	75.13	92.36
TiO_2	0.83	0.58	0.16	1.50
Al_2O_3	4.64	2.33	1.64	7.31
Fe_2O_3	8.29	2.72	3.65	12.16
MnO	0.03	0.01	0.01	0.05
MgO	0.27	0.17	0.02	0.50
CaO	0.19	0.10	0.07	0.35
Na_2O	0.02	0.01	0.00	0.04
K_2O	1.42	0.71	0.49	2.21
P_2O_5	0.11	0.05	0.04	0.18
LOI	0.76	0.50	0.18	1.41

	Ave.	St. Dev.	Min	Max
SiO_2	58.18	7.34	36.84	71.04
TiO_2	2.60	1.24	0.57	4.33
Al_2O_3	14.18	1.95	9.73	18.90
Fe_2O_3	15.19	5.08	2.23	24.69
MnO	0.03	0.05	0.01	0.25
MgO	0.89	0.36	0.17	1.56
CaO	0.61	0.53	0.05	2.56
Na_2O	0.11	0.26	0.02	1.33
K_2O	4.17	0.77	2.49	5.96
P_2O_5	0.36	0.19	0.05	0.78
LOI	2.81	0.47	1.72	4.05

	Ave.	St. Dev.	Min	Max
SiO_2	33.84	12.80	8.80	50.40
TiO_2	0.58	0.27	0.12	1.11
Al_2O_3	11.98	5.62	3.69	23.31
Fe_2O_3	47.02	14.82	23.07	81.71
MnO	0.10	0.21	0.01	0.83
MgO	0.22	0.34	b.d.l.	1.38
CaO	0.08	0.06	0.03	0.26
Na_2O	0.05	0.07	b.d.l.	0.29
K_2O	1.28	0.83	0.05	2.95
P_2O_5	0.08	0.02	0.03	0.11
LOI	4.26	4.12	0.83	16.61

	Ave.	St. Dev.	Min	Max
SiO_2	60.66	10.09	39.13	76.44
TiO_2	1.11	0.25	0.74	1.45
Al_2O_3	18.46	3.64	11.21	23.90
Fe_2O_3	9.50	8.91	0.58	24.21
MnO	0.05	0.06	b.d.l.	0.20
MgO	0.19	0.16	b.d.l.	0.56
CaO	0.05	0.06	0.01	0.22
Na_2O	0.07	0.03	0.02	0.11
K_2O	0.89	0.45	0.01	1.48
P_2O_5	0.05	0.03	0.02	0.16
LOI	8.28	3.29	3.81	16.46

	Ave.	St. Dev.	Min	Max
SiO_2	48.06	8.79	40.17	66.15
TiO_2	1.69	0.32	1.34	2.09
Al_2O_3	33.88	4.22	24.83	38.02
Fe_2O_3	4.20	3.23	0.77	10.29
MnO	0.01	0.00	b.d.l.	0.01
MgO	0.13	0.09	b.d.l.	0.23
CaO	0.05	0.03	0.01	0.10
Na_2O	0.15	0.20	0.01	0.58
K_2O	2.58	2.74	0.01	7.36
P_2O_5	0.09	0.05	0.04	0.19
LOI	8.36	2.73	5.04	12.22

Figure 5.1: Plots of average major element oxides according to the Gamagara stratigraphy normalized to PAAS with corresponding tables of averages, standard deviations and ranges for each shale type. Tabulated data is in wt. %; b.d.l. = below detection limit

5.2.2. Trace Elements

Variations in PAAS-normalized trace elements through the units of the Gamagara are made available in Figure 5.2 and are discussed from the base upwards. According to Rollinson (1993), geochemical groupings of the trace elements may be categorised follows: Low field strength elements (LFSE) including Rb, Ba and Sr; High field strength elements (HFSE) including Th, U, Nb, Zr, Y, Pb and Sc; Transition metals including V, Cr, Co, Ni, Cu and Zn. Results will be discussed according to such categories. Although not displayed on the plots of Figure 5.2, S and Cl data are included in the corresponding tables. References to enrichments and depletions in the discussion are made relative to PAAS values.

For the Doornfontein Members' average aluminous shale, LFSE are strongly depleted except for Sr which is a close fit to PAAS. Moderate enrichments of HFSE (average of 1.7 times PAAS) occur in the aluminous shales. Large variations in transition metals occur, notably highly enriched Cr and highly depleted Cu and Zn.

Average black shales show strongly depleted LFSE and a close fit to HFSE (average of 1.25 times PAAS). Variations in transition metals include strongly enriched Cr and moderate to strongly depleted Co and Zn respectively.

Ferruginous shales LFSE are strongly depleted except for Sr which is a close fit to PAAS. Excepting Th and Sc which are close fit to PAAS, moderate depletions occur in all other HFSE. Variations in transition metals occur, most of which are moderately depleted except highly enriched Cr and highly depleted Zn.

Red shales of the Sishen Members' LFSE closely fit PAAS values. Strong enrichments occur in the HFSE's of these red shales (Nb and Zr values can be up to 9-fold and 4-fold that of PAAS respectively). Moderate to strong enrichment of transition metals occur with the exception of moderately depleted Cu and strongly depleted Zn.

Shales/quartzites of the Marthaspoort Member were sampled in the transitional upward coarsening sequence, as such they capture the quartzites interbedded with the red shales and record somewhat diluted signals of the red shales below (where data is available).

From the data available in the Paling Members' green and red shales, a closely fitting PAAS profile is evident with the exception of moderately depleted Sr and Pb and moderately enriched Cr values.

PALING MEMBER

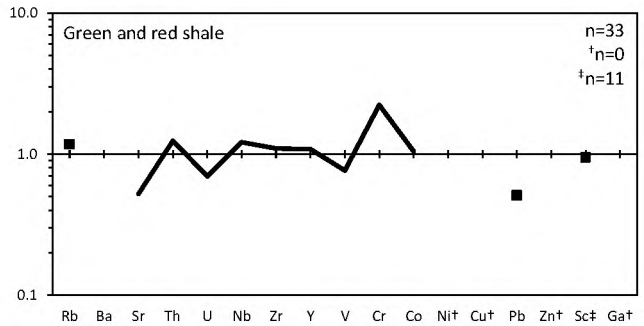

	Ave.	St. Dev.	Min	Max
Rb	188	34	106	239
Ba	n.d.	n.d.	n.d.	n.d.
Sr	104	93	28	403
Th	18	4	11	26
U	2	1	1	6
Nb	23	7	11	42
Zr	230	80	117	464
Y	29	7	21	50
V	115	22	80	171
Cr	246	99	67	483
Co	24	16	6	77
Ni†	n.d.	-	-	-
Cu†	n.d.	-	-	-
Pb	10	7	2	32
Zn†	n.d.	-	-	-
Sc†	15	2	11	19
Ga†	n.d.	-	-	-
S†	n.d.	-	-	-
Cl†	n.d.	-	-	-

MARTHASPOORT MEMBER

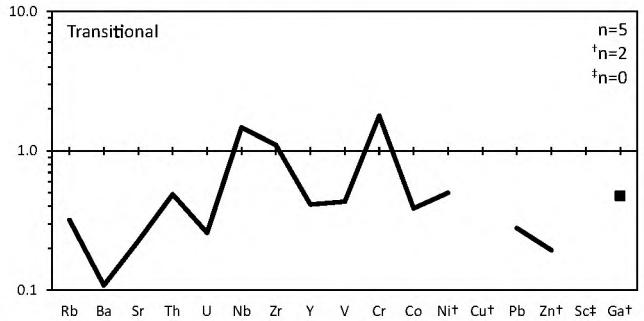

	Ave.	St. Dev.	Min	Max
Rb	51	27	18	83
Ba	71	24	47	94
Sr	45	31	17	85
Th	7	4	1	13
U	1	1	b.d.l.	2
Nb	28	18	6	53
Zr	231	117	73	351
Y	11	7	3	20
V	65	36	22	106
Cr	197	105	68	303
Co	9	7	b.d.l.	21
Ni†	28	15	13	42
Cu†	b.d.l.	-	-	-
Pb	6	3	b.d.l.	8
Zn†	17	13	4	29
Sc†	n.d.	-	-	-
Ga†	10	5	5	14
S†	195	195	b.d.l.	390
Cl†	69	18	51	86

SISHEN MEMBER

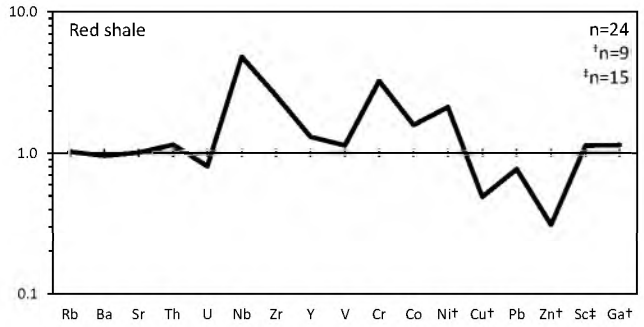

	Ave.	St. Dev.	Min	Max
Rb	163	30	78	200
Ba	620	520	183	1549
Sr	201	67	118	370
Th	17	3	10	22
U	2	1	1	6
Nb	91	50	11	177
Zr	535	219	153	926
Y	35	10	20	59
V	169	47	88	289
Cr	355	117	152	627
Co	36	16	8	71
Ni†	116	40	65	181
Cu†	24	19	b.d.l.	64
Pb	15	5	6	25
Zn†	26	11	12	50
Sc†	18	4	12	25
Ga†	23	4	16	29
S†	810	356	78	1382
Cl†	43	31	18	107

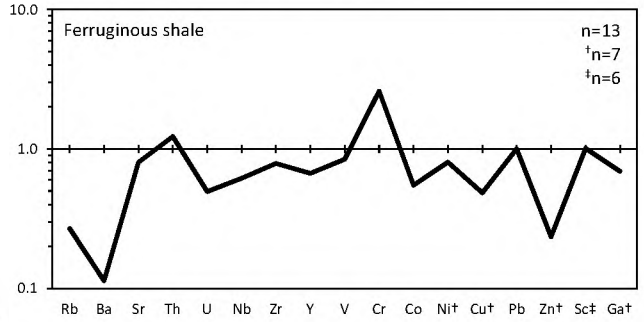

	Ave.	St. Dev.	Min	Max
Rb	43	25	3	91
Ba	74	23	32	102
Sr	161	99	28	322
Th	18	6	10	29
U	2	3	b.d.l.	9
Nb	12	4	5	20
Zr	166	73	39	319
Y	18	8	7	37
V	127	47	52	190
Cr	286	239	52	1001
Co	13	10	b.d.l.	30
Ni†	44	69	b.d.l.	206
Cu†	24	19	b.d.l.	43
Pb	20	11	9	46
Zn†	20	11	8	41
Sc†	16	3	12	21
Ga†	14	7	5	26
S†	130	104	b.d.l.	303
Cl†	55	31	26	114

DOORNFONTEIN MEMBER

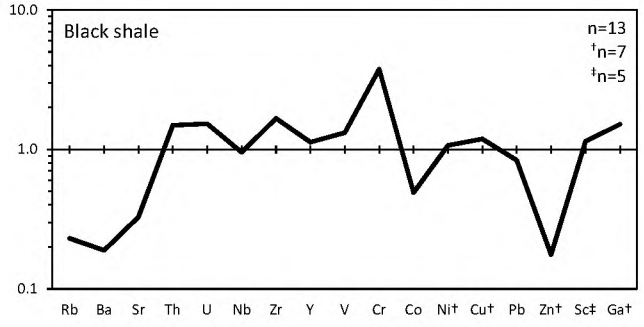

	Ave.	St. Dev.	Min	Max
Rb	37	19	4	60
Ba	123	69	16	219
Sr	66	21	26	105
Th	22	5	13	29
U	5	3	b.d.l.	10
Nb	18	3	13	22
Zr	351	92	177	503
Y	30	7	20	47
V	198	63	122	311
Cr	414	111	192	611
Co	11	9	b.d.l	32
Ni†	59	69	b.d.l.	218
Cu†	59	93	b.d.l.	272
Pb	17	14	5	62
Zn†	15	23	3	71
Sc†	18	5	11	22
Ga†	30	5	21	35
S†	4065	8540	31	24893
Cl†	74	42	15	147

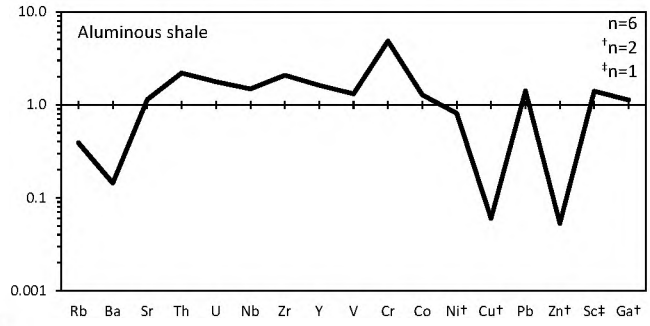

	Ave.	St. Dev.	Min	Max
Rb	62	62	b.d.l.	170
Ba	94	83	11	176
Sr	227	144	85	453
Th	32	4	26	38
U	5	2	3	8
Nb	28	3	24	32
Zr	436	106	302	562
Y	44	11	25	56
V	197	64	132	312
Cr	533	188	255	792
Co	29	48	b.d.l.	135
Ni†	45	3	42	47
Cu†	3	3	b.d.l.	6
Pb	28	29	7	92
Zn†	5	2	3	6
Sc†	22	-	-	-
Ga†	23	1	22	23
S†	1259	1097	162	2356
Cl†	53	31	22	84

Figure 5.2: Plots of average trace elements according to the Gamagara stratigraphy normalized to PAAS with corresponding tables of averages, standard deviations and ranges for each shale type. Tabulated data in ppm; b.d.l. = below detection limit; n.d. = no data.

5.2.3. Rare Earth Elements

Stratigraphic variations of the PAAS normalized REE values are shown in Figure 5.3. Four REE patterns emerge according to each stratigraphic unit of the Gamagara and will be discussed from the base upwards. A line drawn through La and Lu are termed 'baselines' and their slopes are used in the following discussion.

Aluminous and black shales are plotted together as they invariably display similar patterns of relative depletions in LREE compared with HREE imparting a gently inclined baseline trend. The average LREE PAAS-normalized value ranges between 0.68 and 0.96, compared to average HREE PAAS-normalized value, ranging between 0.73 and 1.32. The average ∑LREE/∑HREE ratio is 11, compared to 13 for PAAS. Eu/Eu* ranges between 1.03 and 1.06 and Ce/Ce* ranges between 0.93 and 1.05 with one outlier in sample HR9 (Ce/Ce* = 0.85).

Ferruginous shales are characterised by an essentially flat baseline, although a relatively slight enrichment in LREE compared to HREE exists in three of the samples. Positive Ce anomalies exists in most samples (Ce/Ce* ranges between 1.06 and 1.31) with one outlier for sample HR16 (Ce/Ce* = 0.90). The average ∑LREE/∑HREE ratio is 18 with a standard deviation of 6 due to the variations present in this litho-unit.

Red shales of the Sishen Member display a steeply declined baseline characterised by strong LREE enrichments and average PAAS-normalized values ranging between 1.3 and 3.5. Relative to PAAS, the HREE's may still be enriched with average PAAS-normalized values ranging between 0.9 and 1.9. All samples display positive Eu anomalies with Eu/Eu* ranging between 1.20 and 1.48 while Ce/Ce* ranges between 1.03 and 1.06 with one outlier for sample SAC7 with Ce/Ce* = 1.20. The average ∑LREE/∑HREE ratio is 24.

Green and red shales of the Paling Member display a gently declined baseline characterised by weak to moderate LREE enrichments relative to HREE. Relative to PAAS, LREE's display slightly depleted to slightly enriched trends with PAAS-normalized values ranging between 0.8 and 1.3. The HREE are invariably depleted with PAAS-normalized values ranging between 0.6 and 0.9. All samples display positive Ce anomalies with Ce/Ce* ranging between 1.09 and 1.49. Weak to moderate positive Eu anomalies exist with Eu/Eu* ranging between 1.03 and 1.18 with two outliers in samples PO13 and QK14 (Ce/Ce* is 0.97 and 0.86 respectively). The average ∑LREE/∑HREE ratio is 19.

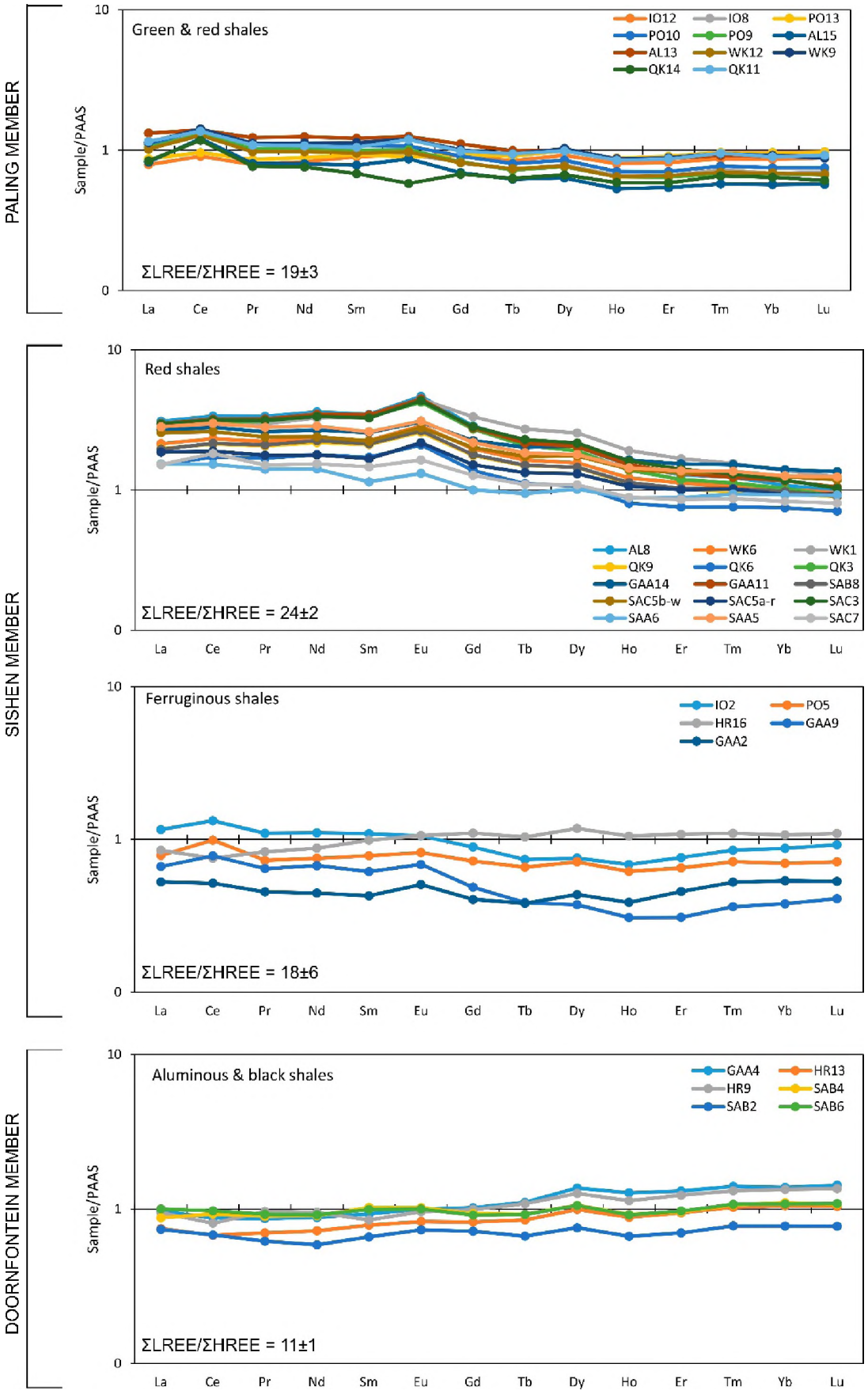

Figure 5.3: PAAS-normalized REE plots according to the Gamagara stratigraphy (excluding Marthaspoort Member). Errors on ∑LREE/∑HREE are standard deviations.

5.3. Chemical Index of Alteration

The contents of alkali and alkaline earth metals in shales are affected by the degree of chemical weathering in their source rocks. A quantitative approach to evaluate chemical weathering in shales was developed by means of the chemical index of alteration (CIA; Nesbitt and Young, 1982). Shale averages for each unit are plotted in Figure 5.4 as molar proportions within Al_2O_3, CaO* + Na_2O, K_2O (A-CN-K) compositional space, where CaO* represents CaO in silicate-bearing minerals only (Nesbitt and Young, 1982).

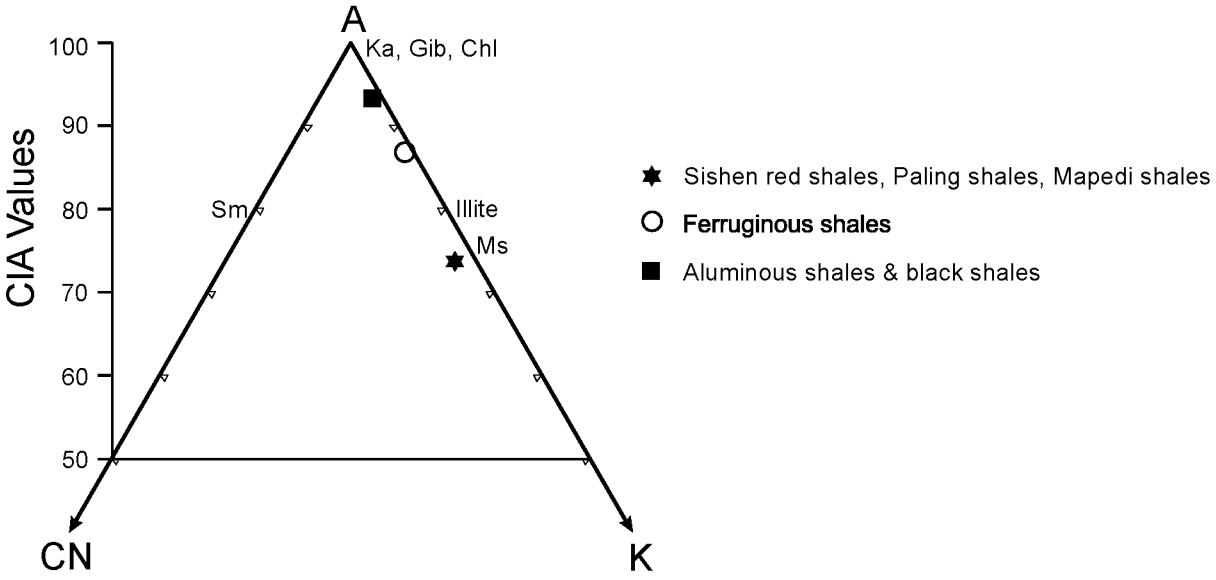

Figure 5.4: Ternary A-CN-K plot indicating the average CIA values for the Gamagara Formation.

Averages for the Doornfontein Members' black and aluminous shales record a CIA value of 94.1 (n=19; st. dev. 4.7) and have the lowest molar proportions of K of all the shales in the Gamagara. Ferruginous shales have an average CIA value of 84.3 (n=13; st. dev. 8.41) while the Sishen red and Paling shales together have the lowest average CIA value of 74.4 (n=57; st. dev. 5.3) and share the highest molar proportion of K of all the shales in the Gamagara. Molar proportions of CaO*+Na_2O record low averages for all shale types. The difference in CIA values of the Gamagara suggest either large variations in the degree of chemical weathering or changes in provenance during sedimentation. An alternate explanation involves processes of K-metasomatism which ultimately obscures CIA values (Fedo *et al.*, 1995).

5.4. Nd Isotopes

Neodymium isotopic data of the Sishen and Paling members are reported in Table 5.1. All samples for the Sishen Member were taken from the red shale lithofacies. The relative enrichment of LREE's are represented by the ratios of ∑LREE/∑HREE (Table 5.1). For visual comparison, PAAS-normalized REE diagrams for these samples are displayed in Figure 5.3. The present day ε_{Nd} compositions of the Sishen Member range from -16 to -19 and correspond to the higher LREE-enrichment ratios (ranging between 22 and 28). The present day ε_{Nd} compositions of the Paling Member range from -23 to -26 and correspond to the lower LREE-enrichment with ratios ranging between 18 and 19. The Paling Member shales have a T_{DM} model age ranging between 2.27 to 2.39 Ga while the Sishen Member shales' T_{DM} model ages range between 1.73 to 1.86 Ga. Mapedi's ε_{Nd} values for its HFSE enriched sample (N27) and unenriched sample (N8) correspond to the (enriched) Sishen and (unenriched) Paling shales respectively.

Table 5.1: Neodymium isotopic compositions with calculated T_{DM} model ages.

Member	Sample	∑LREE/ ∑HREE	$^{143}Nd/^{144}Nd$	±2s internal	ε_{Nd}	Sm (ppm)	Nd (ppm)	$^{147}Sm/^{144}Nd$	T_{DM} (Ga)
Paling	WK9	17.9	0.511430	12	-23.6	6.33	35.89	0.1061	2.29
	QK11	17.8	0.511396	12	-24.2	5.87	34.36	0.1028	2.27
	AL13	19.0	0.511298	11	-26.1	6.81	39.88	0.1028	2.39
	N8*	n.d.	0.511466	11	-22.9	n.d.	n.d.	n.d.	n.d.
Sishen	WK6	23.7	0.511701	10	-18.3	12.60	75.02	0.1011	1.84
	QK3	28.0	0.511813	10	-16.1	18.54	107.40	0.1039	1.73
	AL8	28.7	0.511784	7	-16.7	19.32	114.90	0.1012	1.73
	SAC 5B	22.8	0.511642	11	-19.4	12.45	76.39	0.0981	1.86
	SAC 5A	22.1	0.511676	10	-18.8	9.34	56.87	0.0988	1.83
	N27*	n.d.	0.511754	8	-17.3	n.d.	n.d.	n.d.	n.d.

*Mapedi Samples (Land et al., in review)
n.d.=no data

5.5. Geochemical Characteristics

5.5.1. Mineralogical Controls

Titania

As titania is found to be an important mineral in the Sishen red shale unit, TiO_2 is plotted against other HFSEs in order to determine whether or not mineralogical controls exist. In the surrounding lithofacies, the elements used were based on the strength of their correlation with TiO_2.

Figure 5.5 shows plots of TiO_2 *versus* Nb, Zr, P_2O_5 and Al_2O_3 differentiating four lithofacies of the Gamagara Formation. Note the moderate to strong correlations between TiO_2 and Nb in all lithofacies ($R^2 \geq 0.75$), suggesting that Nb is chiefly hosted in the titania minerals. Zr has the strongest correlation with TiO_2 in the Sishen red shale lithofacies ($R^2 = 0.86$), moderate correlations in the ferruginous and Paling shale units ($R^2 = 0.69$ and 0.66 respectively) and a weak correlation in the black shale unit ($R^2 = 0.41$). Plots of P_2O_5 and Al_2O_3 against TiO_2 were swopped out according to where correlations were strongest in each lithofacies. Only in the Sishen red shales did a moderate correlation exist between TiO_2 and P_2O_5 ($R^2 = 0.60$). In the black, ferruginous and Paling shale lithofacies, moderate to poor correlations existed rather with Al_2O_3 ($R^2 = 0.54$, 0.56 and 0.37 respectively).

The nature of mineralisation in the Sishen red shale unit is the probable cause for the relationship seen with P_2O_5. In this unit authigenic titania and fluorapatite ($Ca_5[PO_4]_3F$) are found to coexist in almost all instances. Furthermore, the strong to moderate correlations with TiO_2 *versus* Nb, Zr and P_2O_5 in this lithofacies suggests that the titania and fluorapatite are chiefly responsible for the enriched HFSE values found in this unit.

In units without the HFSE enrichment, P_2O_5 takes either a non-existent correlation (e.g. in the black and ferruginous units, plots not shown) or a poor anticorrelation with TiO_2 ($R^2 = -0.35$ in the Paling shale; plot not shown). Instead, moderate to weak correlations exist with Al_2O_3 in these units which may suggest that clays have a more dominant control on TiO_2 distribution when the HFSE enrichment is absent. The aluminous shale unit has been purposefully left out of the plots in Figure 5.5 as weak to non-existent correlations existed between TiO_2 and all the aforementioned elements except Zr ($R^2 = 0.72$), and a larger data set is required to obtain meaningful relationships.

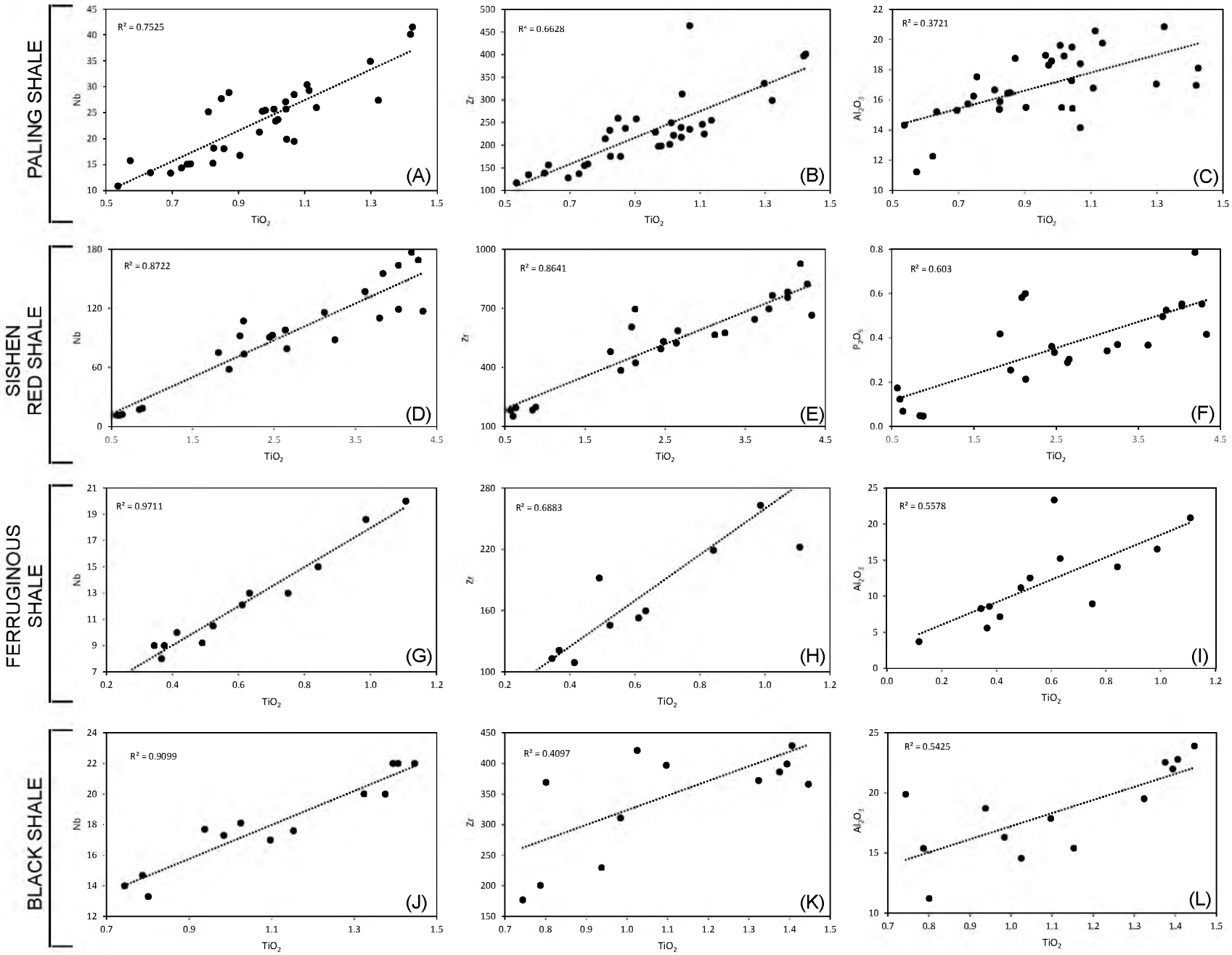

Figure 5.5: Plots for TiO_2 *versus* Nb, Zr, P_2O_5 and Al_2O_3 for individual lithofacies in the Gamagara Formation

REEs

REE distributions in cratonic shales are widely used to characterize source compositions of detrital sediments (Taylor and McLennan, 1985). During erosion and sedimentation, REEs are carried largely as suspended rather than dissolved loads; and hence, they may be transferred nearly in bulk from source to sediment (Condie, 1991). Other variables such as tectonic setting, chemical weathering, hydraulic sorting, and adsorption play roles in controlling REE distributions (Condie, 1991).

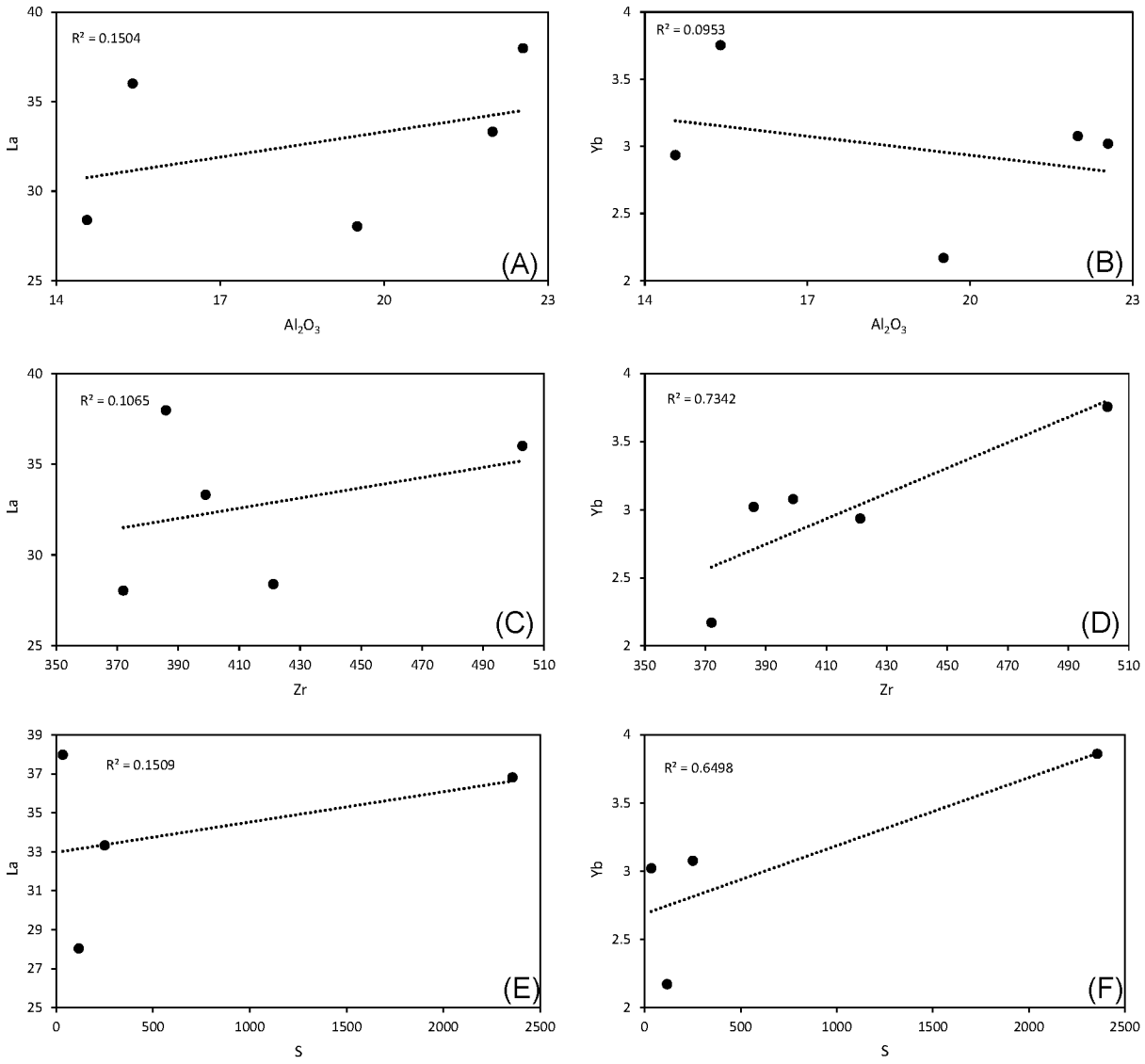

Figure 5.6: Binary plots showing elemental relationships in the black shale lithofacies

Due to the difficulty of mineral separations in fine-grained sediments, Condie (1991) constrained mineralogical controls from linear regression between elements. Condie (1991) paired whole rock Zr, Al_2O_3 and P_2O_5 values (representing zircon, clay and rare-earth bearing phosphates respectively) to REEs values (represented by La and Yb) in average cratonic shales of various ages to determine the importance these elements may have on the overall REE content. This exercise is repeated here with elements of importance for each lithofacies in order to determine whether or not important mineralogical controls exist (Figure 5.6 to Figure 5.10). The element S is used in the black shale unit as abundant pyrite was available in this lithofacies. Aluminous shales have not been included due to the lack of REE data for the unit.

Figure 5.6 shows Al_2O_3, Zr and S plotted against La and Yb in the black shales lithofacies. The lack of correlation in Al_2O_3 with both La and Yb suggests clay minerals do not play a role in the REE patterns in this lithofacies. The most interesting observation are the correlations between the pairs of Zr - La and Zr – Yb. The weak correlation with La ($R^2 = 0.11$) and moderate correlation with Yb ($R^2 = 0.73$) could suggest zircon plays an important role in the inclined nature of the REE baseline trend in Figure 5.3. As pyrite plays a pivotal role in this lithofacies, La and Yb is compared with S (n=4). It is found that pyrite could possibly play a major role in the HREE enrichment, as La - S pairs showed little correlation ($R^2 = 0.15$), compared with the moderate correlation in the Yb - S pair ($R^2 = 0.65$).

Figure 5.7 shows Al_2O_3, TiO_2 and Zr plotted against La and Yb as well as Fe_2O_3 plotted against total LREE and HREE. For ferruginous units weak to moderate correlations exist between Al_2O_3, TiO_2 and Zr with Yb, however weak to non-existent correlations exist between the same elements and La. The abundance of clay, titania and zircon minerals along with their respective ratios of heavy to light REEs could play an important role in the relatively flat REE baseline trend in this lithofacies. Fe_2O_3 has a non-existent correlation with LREEs but a strong anti-correlation with HREEs ($R^2 = -0.81$), and, as hematite increased so did the HREEs decrease in this unit, leaving behind the flat REE trend that is observed (Figure 5.3). As the ferruginous unit overlies the black shale lithofacies, it is suggested that the change in REE trend occurs between these two units as they are genetically linked. On average, a 31-fold decrease in S is evident between the carbonaceous shales and overlying ferruginous unit (tables in Figure 5.2). It was shown that S correlated moderately with Yb in the black shale unit and, under the assumption that black shales are the precursor to ferruginous shales, it may suggest that the removal of S in pyrite to form hematite may have lowered the HREEs.

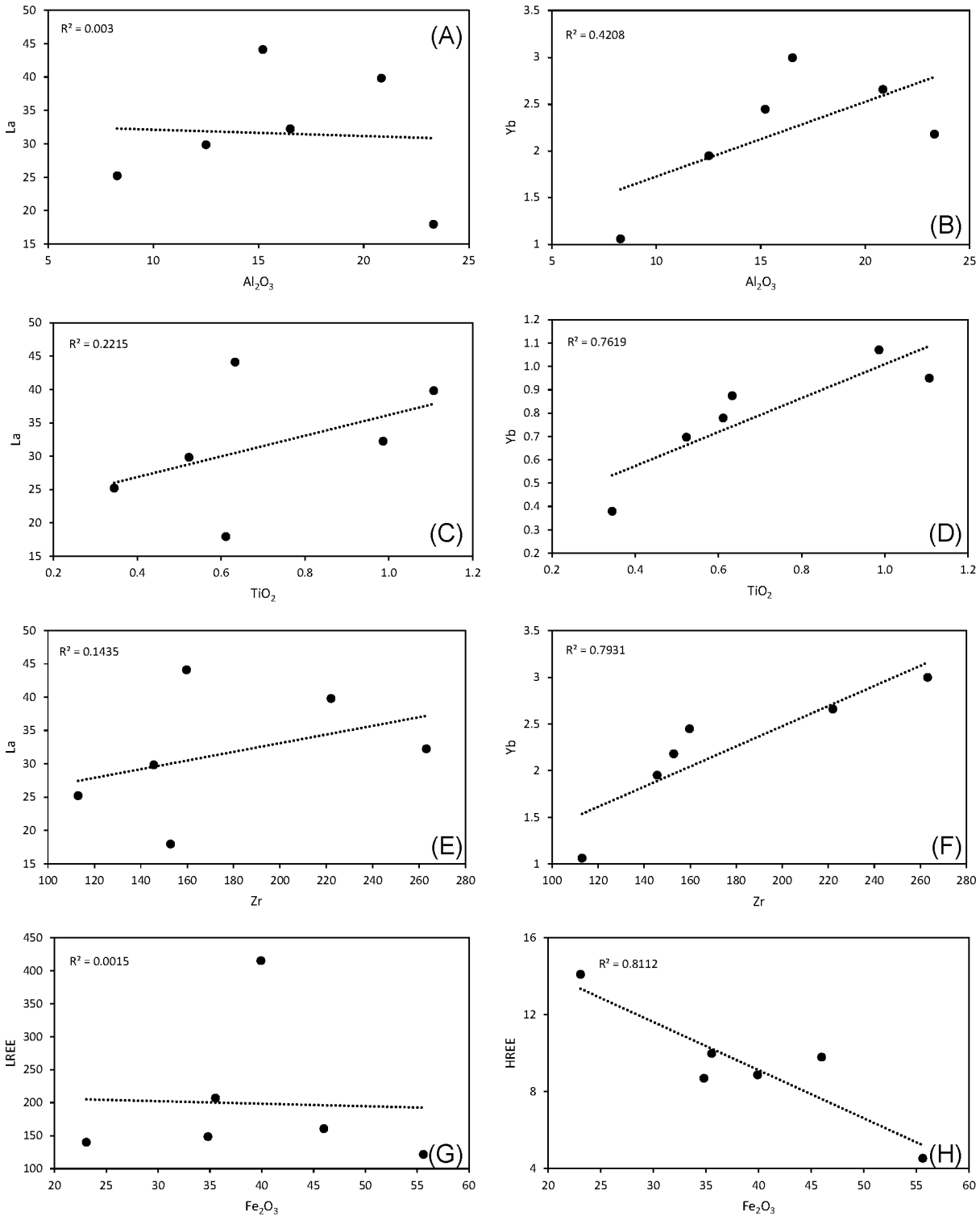

Figure 5.7: Binary plots showing elemental relationships in the ferruginous lithofacies.

Figure 5.8 shows Al_2O_3, TiO_2, P_2O_5 and Zr plotted against La and Yb in the Sishen red shale lithofacies. Moderate correlations exist between Al_2O_3 with La and Yb ($R^2 = 0.60$ and 0.71 respectively) suggesting that clay minerals do have a control on the total REE contents in the shales. HFSEs TiO_2 and Zr are

strongly enriched in this lithofacies and correlate better with La (R^2 = 0.56 and 0.71 respectively) than they do with Yb (R^2 = 0.10 and 0.49 respectively), suggesting that titania and zircon have a control on the steeply declining baseline trend observed in this unit. Moderate correlations exist between P_2O_5 with La and Yb (R^2 = 0.62 and 0.78 respectively) and may suggest that phosphates (apatite/fluorapatite/monazite) have a strong control on the total REE content of these shales and thus its overall relative enrichment to PAAS.

Figure 5.9 shows Al_2O_3, TiO_2, P_2O_5 and Zr plotted against La and Yb in the Paling shale lithofacies Non-existent correlations exists with Al_2O_3 and Zr *versus* La and Yb. For TiO_2, a weak correlation exists with La (R^2 = 0.24) and no correlation with Yb (R^2 = -0.02). For P_2O_5, a weak correlation exists with La (R^2 = 0.34) and a moderate correlation exists with Yb (R^2 = 0.57). These weak to non-existent correlation may suggests that REE distribution is not dominantly controlled by any one of the minerals hosting these elements but rather by a combination thereof.

Nd-Sm

Nd and Sm are compared to TiO_2 and P_2O_5 in both the Sishen red shale and the Paling shale as these two units were compared by means of a Nd isotope study (Figure 5.10). Note how both Nd and Sm have strong correlations with TiO_2 and moderate (to weak) correlations with P_2O_5 in the red shales of the Sishen Member. In the Paling shales, non-existent correlations exist with TiO_2, however moderate (to strong) correlations with P_2O_5 exist. This suggests that titania must provide an important control on the concentrations of Sm and Nd in the Sishen red shale but not in the Paling shale. Phosphates (apatite/fluorapatite/monazite) must also have moderate to strong controls on the Nd and Sm concentrations in both lithofacies. Observations of authigenic titania and fluorapatite minerals may very well question the reliability of the Nd-Sm systematics in the red shales of the Sishen Member and this will be carefully considered in the following section.

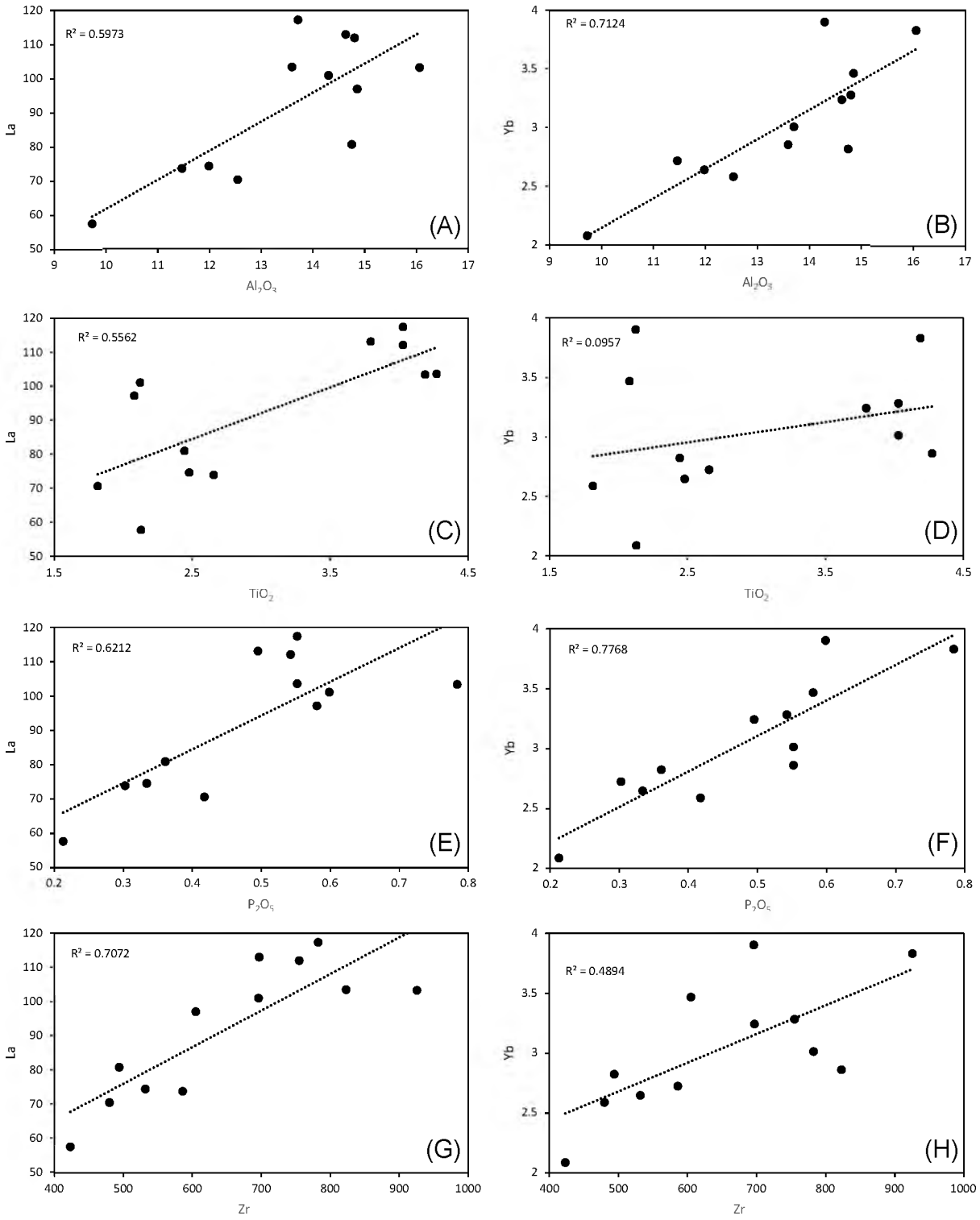

Figure 5.8: Binary plots showing elemental relationships in the Sishen red shale lithofacies

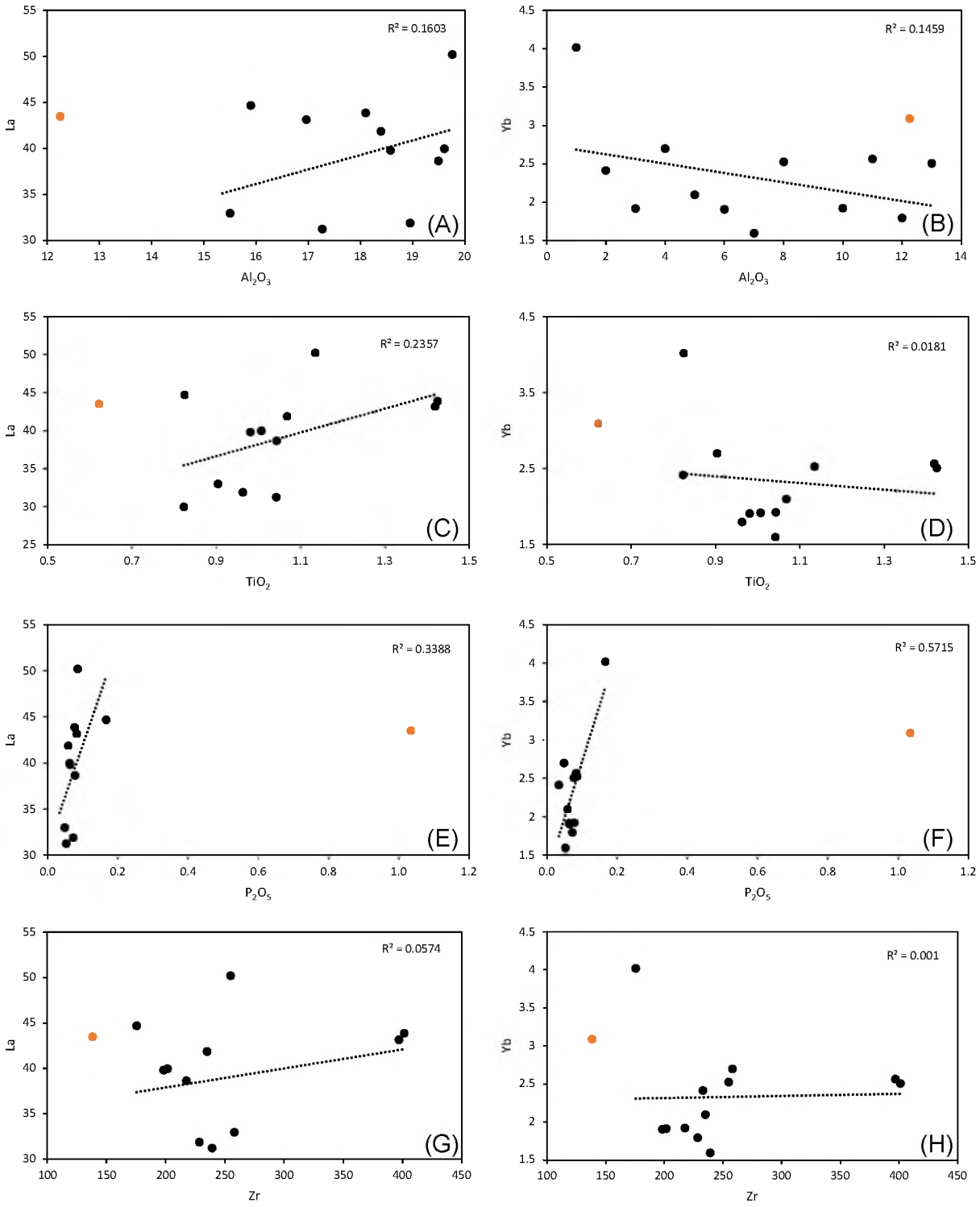

Figure 5.9: Binary plots showing elemental relationships in the Paling shale lithofacies. The orange dot was excluded in linear regression trends as it displayed anomalous levels of P_2O_5 (14-fold higher than average P_2O_5; sample WK16).

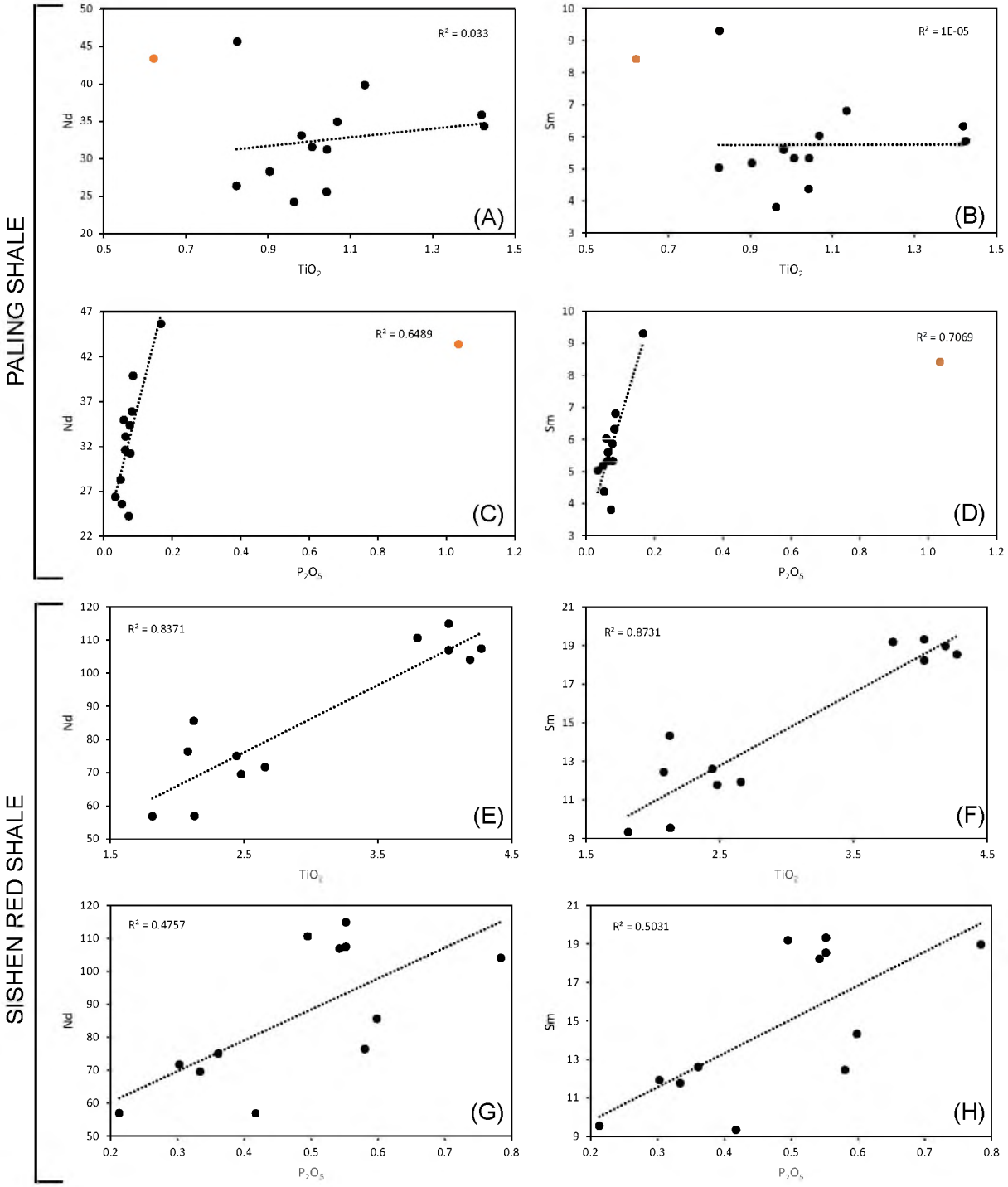

Figure 5.10: Plots of TiO_2 and P_2O_5 *versus* Nd and Sm for the Sishen red shale and paling shale lithofacies used in the Nd-isotope study. The orange dot was excluded in linear regression trends in the Paling shale as it displayed anomalous levels of P_2O_5 (14-fold higher than average P_2O_5; sample WK16).

5.5.2. Chemostratigraphy

Chemostratigraphic plots were constructed using average values for each lithofacies of the Gamagara Formation (Figure 5.11). Six major elements SiO_2, TiO_2, Al_2O_3, Fe_2O_3, K_2O and P_2O_5, three HFSEs Nb, Zr and Y, and the total REE contents were selected to show the vertical compositional variation in the Gamagara Formation.

Based on the PAAS normalised geochemistry (section 5.2) certain anomalies became apparent, most notably the HFSE enrichment in the Sishen red shale unit and, to a lesser extent, in the aluminous shale unit. It has been previously shown that titania and fluorapatite are likely to have the highest control in the Sishen red shales, a relationship which is not seen in the aluminous shale unit (also note the low P_2O_5 content in the aluminous unit). This may suggest that these anomalies are not linked as the chemistry and style of mineralization differs. In the sampled cores, the Sishen red shale unit may be up to ~21m thick and this HFSE anomaly can serve as a good geochemical marker for the Gamagara Formation as it occurs along the N-S strike on the Maremane dome.

It is noteworthy to mention that the red shales and underlying ferruginous unit of the Sishen Member both show higher bulk-rock Fe-oxide. This was first seen in the mineralogy where abundant hematite existed in these units as well as in their petrographic observations and as such Fe-addition was suggested. Lastly, anomalously high bulk-rock K_2O content is observed in both the Sishen red shale as well as in the overlying Paling shale. The excessive potassium has been noted in the literature not only in these units, but also in the paleoweathering profile of the Ongeluk lavas, with the most likely explanation being attributed to metasomatic alteration (Wiggering and Beukes, 1990; Land *et al.*, in review). If this is indeed true, the addition of K would have affected the CIA of these units (section 5.3) and thus requires re-evaluation.

5.5.3. Fe-addition

After evidence of abundant Fe mobilization in the ferruginous and the Sishen red shale units (Figure 4.10c,e and Figure 4.11c), a red and white band of the Sishen red shale lithofacies were sampled individually in order to determine the systematics of the Fe-addition and associated alteration. These results are graphically displayed in Figure 5.12.

Figure 5.11: Chemostratigraphic profile of selected elements and ∑REE for the Gamagara Formation. Each value represents the average as indicated in Figure 5.1 and Figure 5.2. Orange and red highlighted zones indicate HFSE enrichments for aluminous shale and Sishen red shale respectively.

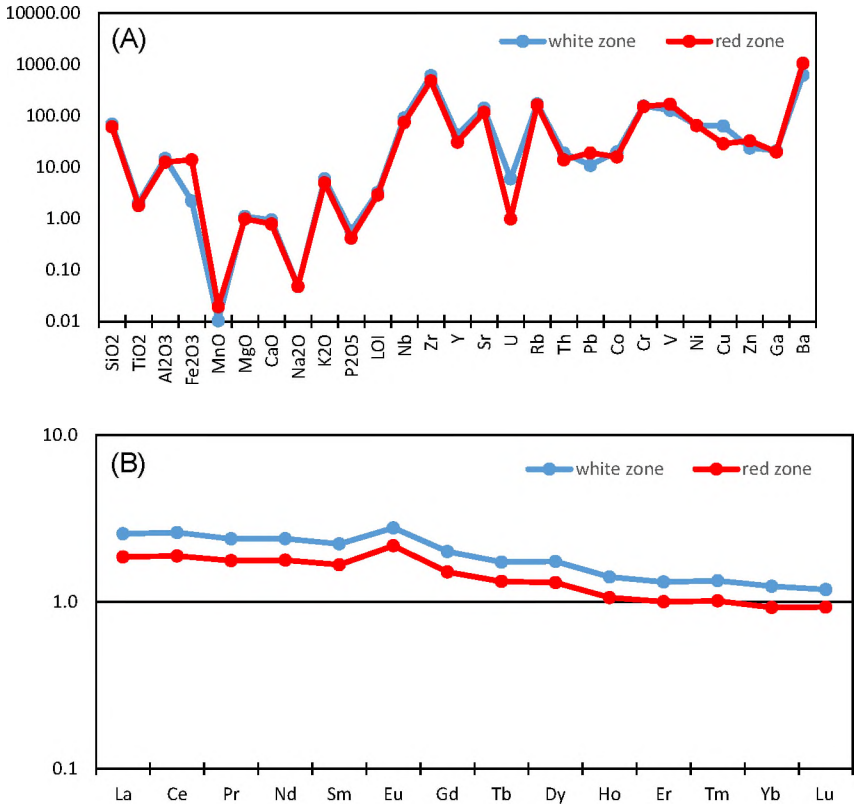

Figure 5.12: Red and white band in the Sishen red shale member. (a) Major and trace element geochemistry. (b) PAAS-normalized REE contents.

In the major and trace element data the largest gains in the red zone have occurred with Fe_2O_3 (6.3-fold), MnO (1.9-fold), Pb (1.7-fold), Zn (1.4-fold) and Ba (1.7-fold), while the largest losses have occurred in U (0.2-fold) and Cu (0.5-fold). In the REE data, a constant loss of between 0.7-to-0.8-fold is observed in the red zone and may be as a result of a closure effect with increasing Fe_2O_3 content. It is difficult to define a hydrothermal system for the Fe-addition event based on the limited petrographic information, however, the geochemical indication of Pb, Zn and Ba with Fe addition is curious and as such will be discussed in the next section.

6. DISCUSSION

6.1. Lithostratigraphic Model

The setting of the Gamagara Formation is summarized in a model stratigraphic profile displaying as many of the representative geological variations that could be encountered in the examined drill-cores (Figure 6.1).The sedimentary response to changes in sea-level are easily recognised by facies changes in the Gamagara Formations' stratigraphy (Figure 6.1).

The lithofacies with the greatest differences between cores occurs in the Doornfontein Member. At the scale of this study (drill-core sections) conglomerate beds appear massive. Texturally, the conglomerates are sub-mature with moderate to poor sorting and are oligomictic with BIF, chert and hematite pebbles. The conglomerates are matrix supported and pebbles range from well-rounded to angular shapes with variable mud content from core to core. Transgression and upward fining produces the gritstone facies, followed by tidal flats forming the muds that make up the black and white shales. The thickness and presence of these shales vary from core to core and thinning and pinching out along strike is attributed to the paleotopographic changes developed along the unconformity. The above mentioned features along with open pit observations and field studies of Van Schalkwyk and Beukes (1986) suggest that the Doornfontein Member represents a braided alluvial fan deposit with proximal and distal sediment supply mostly derived from the iron formations.

The white and black shales display upward coarsening with the increase of wavy silt-to-sand lenses particularly associated with pyritic laminae in the black shales. An upward transition into a cross-laminated, fine-grained (ferruginous) quartzite best fits modern-day analogues of progradational delta lobes (Figure 6.1) as described, for example, by Nichols (2009) and Stow (2010). In such a delta model the shales represent the muds with lenticular and wavy bedded mud/silt and mud/sand couplets as prodelta deposits, grading into cross-laminated fine-grained sands (ferruginous quartzites) which represent the tidal sand bars of a delta front. Common mud drapes and flaser lamination in the well sorted Marthaspoort quartzite lithofacies (essentially a well-rounded, well-sorted orthoquartz arenite) is an indication of more effective reworking by tidal currents in the delta front setting. The deltas are interpreted to be tide-dominated as indicated by: tidal influence with the speculated microbial mat growth; intertidal deposition in the delta top (silt/sand laminae); and flaser laminations (mud drapes) identified in the upward coarsening red shales of the Sishen Member and basal units of the Marthaspoort quartzites (Figure 6.1).

A particular response to sea-level rise on sandy shelves is the deposition of a thin layer of gravel known as transgressive lags (Nichols, 2009). They form during periods of low sea level as sediment deposited on the shelf is reworked by wave action resulting in thin (usually only a few centimetres) conglomerate/gravel beds within the succession. Such contacts are developed between the ferruginous quartzites and red shales of the Sishen Member (Figure 4.4b,c) and again between the Marthaspoort quartzite and Paling shale Member (Figure 4.6 c) as transgression takes place between these units.

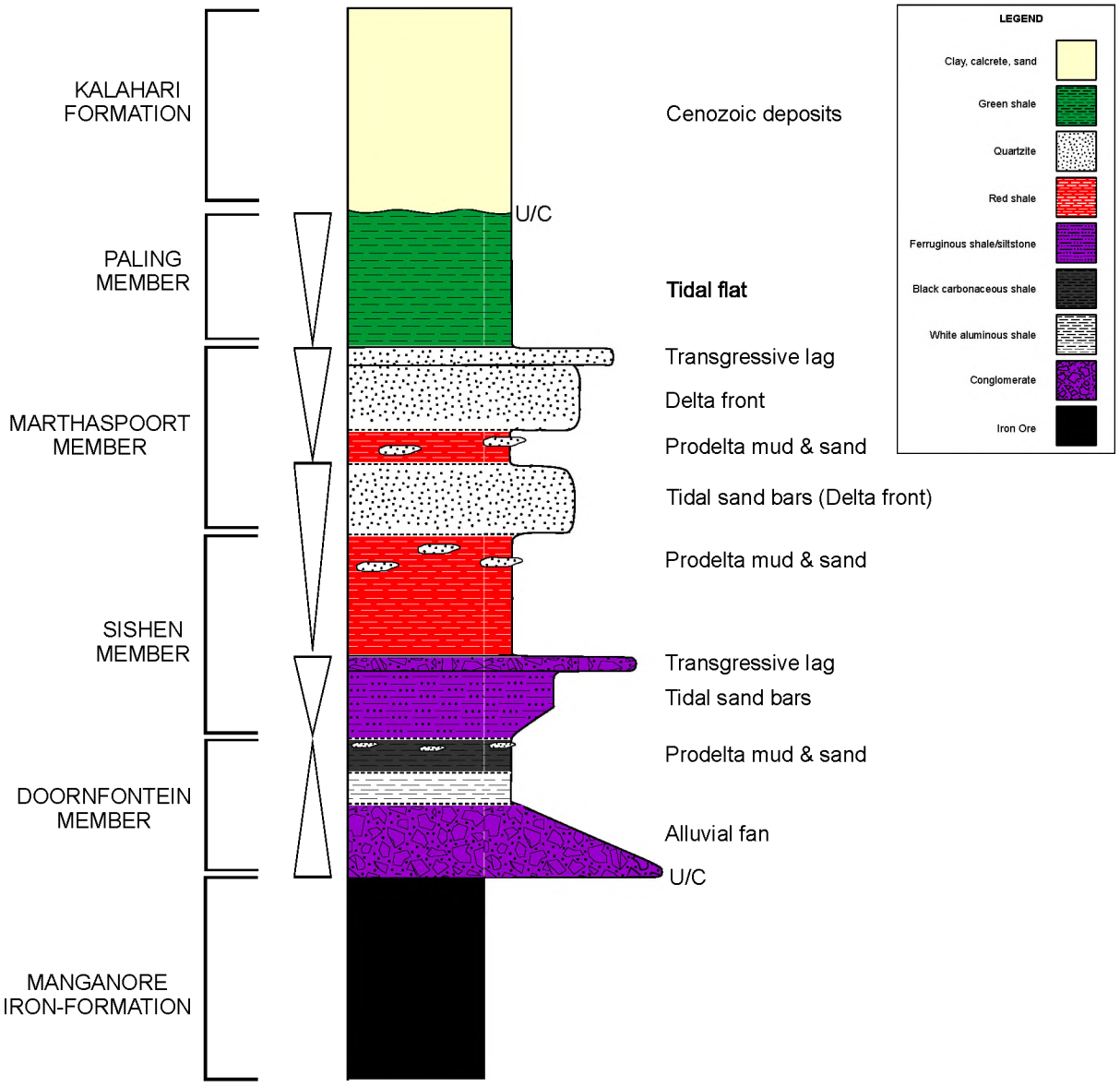

Figure 6.1: Sedimentary log produced from observations made in this study implies a tide dominated delta setting formed the shales and sands the Gamagara Formation.

6.2. Aluminous shales

Van Schalkwyk and Beukes (1986) attribute the white shales derivation from the leaching of iron in red shales (of the Doornfontein Member) which lie adjacent to the black shale unit. They described the processes to produces the white high-alumina shales from early diagenesis with acidic, reducing groundwater solutions derived from stagnant anaerobic waters required to produce the black shales (Van Schalkwyk and Beukes, 1986). In later work with the aid of BSE photomicrographs and SEM-EDS spectrum, Schalkwyk (2005) noted recrystallized diaspore, pyrophyllite and anatase crystals occurring as clays and silt size particles. The diaspore and pyrophyllite are always closely associated, forming dense crystalline aggregates with hematite. Anatase is always associated with this crystallisation occurring as small (≤10 μm) euhedral grains, disseminated inclusions (≤1 μm) along cleavage planes of pyrophyllite, and as a dispersed 'dusty' matrix between crystallised pyrophyllite and diaspore. He concluded that the crystallisation occurred in low-grade metamorphic conditions and crystallization formed at the expense of primary aluminous clays (Schalkwyk, 2005).

From field evidence and petrographic studies in this work, the intimate relationship between aluminous shales and black shales is shown not only by their spatial proximity, but more notably by the mineralisation which occurs in both units (Figure 4.3). Hall (1978) described hypogene replacement processes in a geological survey paper on the Worlds' non-bauxite aluminium resources. The mineralisation involves hot sulphuric-acid charged fluids during late fumarolic stages of a volcanic episode in which leaching of soluble alkaline constituents (Na, K, Ca, Mg) and destruction of feldspar, mica and any other primary minerals in the original rock occurs (Hall, 1978). The process entails volume-for-volume metasomatic replacement of these minerals in such a way that the texture of the original rock may be surprisingly well preserved in spite of the profound change in chemical and mineral compositions (Hall, 1978). Quartz may be left in-tact, except for corroded edges, but silica is liberated during the breakdown of the primary alumina-silicate minerals and is recrystallized as a very fine-grained quartz mosaic (microquartz) with interstices filled with fine grained flakes and shreds of alunite (Hall, 1978). The replacement deposits are characteristically zoned, one worth mentioning is the quartz-alunite zone, in which a grayish-white to pink bleached rock consisting of microquartz intimately mixed with flakes and shreds of alunite and accessory phases which include hematite, anatase and rutile (Hall, 1978).

Although the mineral alunite is not present in these shales today, the metasomatic processes involved in Halls' (1978) descriptions leave behind textures and a style of mineralisation remarkably similar to what is seen in the aluminous and black shales of the Gamagara. Evidence of such textures are seen in Figure 4.3c,d and Figure 4.9c,d by the presence of the bleached black shale unit (Figure 4.3d), corroded quartz grains rimmed by diaspore and pyrophyllite, partially and fully replaced quartz and chert by

pyrophyllite, diaspore and muscovite (Figure 4.9c) and the apparent recrystallized microquartz mosaic texture with interstices filled with euhedral muscovite, pyrophyllite and diaspore (Figure 4.9d and Figure 4.3c). The cross-cutting vein in the bleached black shale unit (Figure 4.3d) further promotes a hydrothermal origin to this unit. The geochemistry provides evidence of Ti and associated HFSE enrichment in the aluminous shales unit (Figure 5.1 and Figure 5.2) and Schalkwyk' (2005) evidence of anatase always being associated with the aluminous minerals is also in agreement with such a style of mineralisation. This mineralogy may suggest that low temperature hydrothermal fluids (<200°C) are responsible for the formation of the aluminous shale unit.

6.3. Carbonaceous Shales and the Ferruginous Unit

The black carbonaceous shales provides strong evidence for the presence of microbial mats in that they preserve a combination of features indicating their presence as discussed in section 4.4. One of the most revealing signs is that of the preserved pyritic wavy laminae. The mechanisms for the pyrite formation are important to note and are discussed in the next paragraph using the Mid-Proterozoic Newland Formation as a proxy.

Laminated pyrite beds (mm to cm thick) are found to occur in distinct horizons of the Newland Formation (Helena embayment of the Belt Basin, Montana, USA; Schieber, 2004). The pyritic laminations are separated by dolomitic clayey shale forming silt/mud couplets with irregular wavy-crinkly internal laminae interpreted as fossil benthic microbial mats (Eriksson *et al.*, 2007). Intercalated storm deposits (silt/ mud couplets) give this type of shale its characteristic striped appearance (Schieber, 2004). Pyritic shales are thought to accumulate in quiet waters under anoxic conditions, however, such a noting is contradicted by the sedimentary features in the interbedded sandstones in the case of the Newland Formations' pyritic shales (Schieber, 1989). Evidence suggests that in the Proterozoic, strongly reducing shales may have accumulated in shallow aerated environments in the presence of benthic microbial mats (Schieber, 1986). Microbial mats will affect several environmental parameters such as Eh, H_2S concentration, dissolved O_2, and light intensity at the interface (Schieber, 1989) and despite aerated waters above, conditions below a mat may be strongly reducing (Bauld *et al.*, 1980). A model proposed for the formation of the pyritic striped shales includes the introduction of iron into the basin by means of continental runoff in the form of iron hydroxides (Eriksson *et al.*, 2007). These iron hydroxides flocculating in near-shore areas would eventually become trapped on the sticky, gelatinous mat surface and would be transformed into pyrite after incorporation into the buried reducing layers of the mat (Schieber, 1989).

In the black shale lithofacies, microbial mat colonisation continued to flourish with the introduction of prodelta sands and muds in the top most sections of the carbonaceous shales. These observations led investigations for microbial mat evidence higher up in the stratigraphy, into the tidal sand bars of the delta front represented by the ferruginous quartzite unit.

The input of iron in the ferruginous quartzite or 'flagstone' unit has long been interpreted as being primary detrital accumulations (Van Schalkwyk and Beukes, 1986; Van Deventer, 2009; Schalkwyk, 2005). The main reasoning behind this is the presence of rounded silt sized hematite grains abundant in the quartzite, thought to be derived from the high grade ores underlying the Gamagara. Following close inspection of the ferruginous quartzite lithofacies, the author proposes a completely new outlook on this unit.

The BSE image used in Figure 4.10b to display the Ferruginous quartzite is displayed again in Figure 6.2 with further annotations and includes additional element maps along with images of the black shales' pyritic laminae for comparison. The presence of wavy beds, crinkly-wavy anastomosing laminae and domal buildups (on top of clay laminae) strongly suggests the presence of microbial mats in the ferruginous unit. The abundant presence of cubic hematite and rounded hematite crystals (confirmed in WDS maps – only Fe signals were obtained) are found in most laminae excluding the thin sand and clay-rich laminae for the most part.

Aluminous phyllosilicates (possibly muscovite or phengite from observations of the K signal in an element map not shown here) occur in close contact with quartz and chert grains shown in black on the BSE image and element maps. On comparison with the pyritic laminae of the black shale unit (Figure 6.2d,e), the author proposes that the iron in the ferruginous quartzite lithofacies is derived from the pyritic laminae produced in an environment conducive to microbial mat growth. Subsequent to pyrite formation, oxidation to hematite has occurred possibly through weathering processes. The rounded nature of the silt-sized hematite grains are explained simply as pseudomorphs of hematite after pyrite framboids (compare hematite in Figure 6.2a,b with pyrite Figure 6.2e). Figure 6.2a annotates the ferruginous shale with respect to the primary depositional environment after early diagenesis and pyrite formation. The yellow lines follow the traces of ancient benthic microbial mats at laminae interfaces (note the domal build-ups above some clay laminae). Factors which would have determined the rate of pyrite formation and thus the variations in laminae are related to factors including microbial mat growth, Fe supply from continental runoff (weathering of the iron formations must have provided a constant supply), energy levels and O_2 content within the water column, and the rates of reduction below the mat surface. Periods of lower energy may have stimulated growth, allowing more iron hydroxide colloids to settle and trap, and ultimately increased the overall Fe content in this lithofacies. The presence of Al

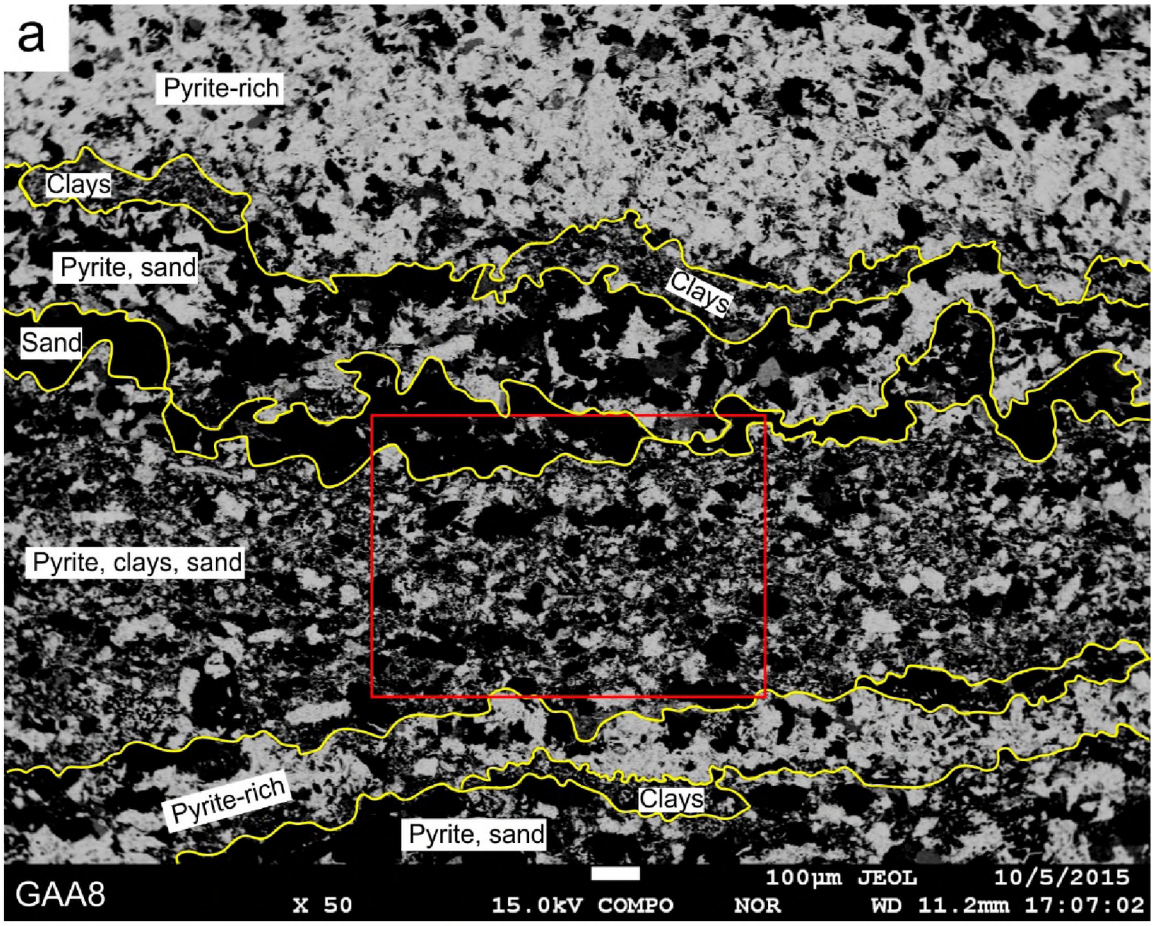
a
Pyrite-rich
Clays
Pyrite, sand
Clays
Sand
Pyrite, clays, sand
Pyrite-rich
Clays
Pyrite, sand
GAA8
X 50
15.0kV COMPO
100µm JEOL
NOR
WD 11.2mm
10/5/2015
17:07:02

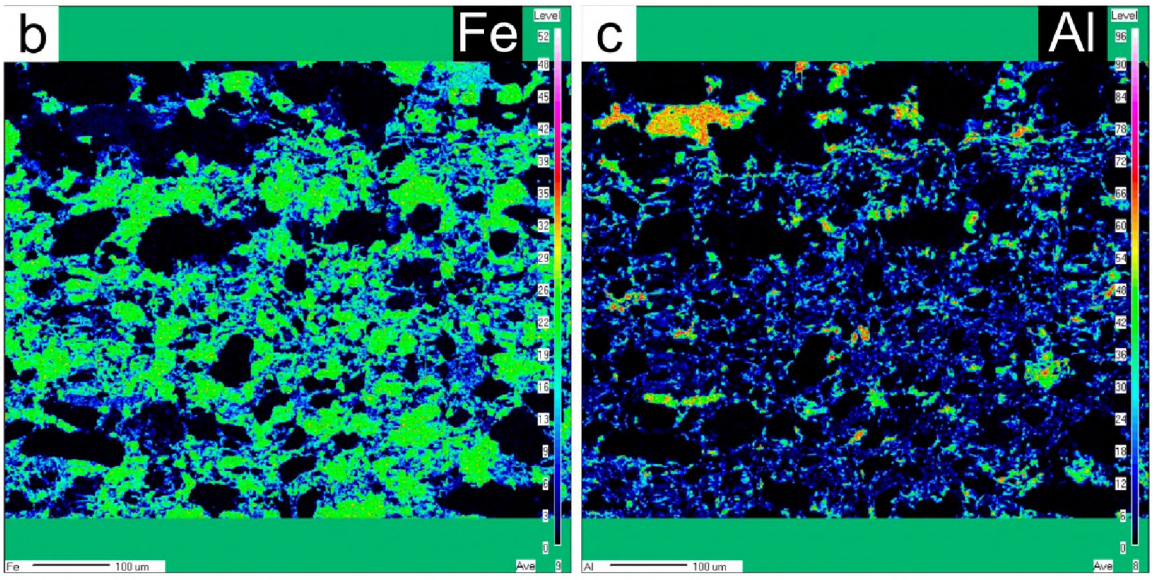
b
Fe
c
Al

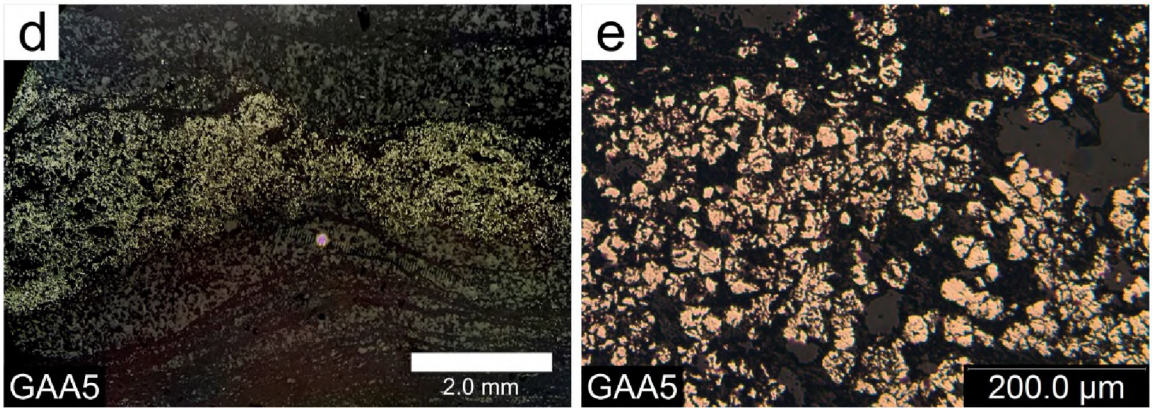
d
GAA5
2.0 mm
e
GAA5
200.0 µm

Figure 6.2: Photomicrographs and element maps explain the genesis of the ferruginous quartzite unit of the Sishen Member. (a) BSE photomicrograph of an iron rich portion of the ferruginous quartzite of the Sishen Shale Member with annotations explained in-text. (b) Element map of Fe displaying the area inside the red box in (a). Note the rounded and cubic habits of hematite crystals (c) Element map of Al displaying the area inside red box in (a) Note alumina minerals flank quartz and chert rims, possibly replacing them (top left of map) in similar reactions that were seen in the aluminous shale unit. (d) Pyrite in the black shale unit forms laminae >2mm thick in a zone where microbial mats once flourished. (e) Close up of pyrite in the black shale unit shows both euhedral and framboidal pyrite crystals are remarkably similar to the hematite crystals in the ferruginous shale unit.

rich phases rimming quartz and chert grains is similar to the style of mineralization seen in the aluminous shale unit and the author speculates that the same event may be responsible for these alterations. The variations in the host rock composition ultimately alter the fluid composition and subsequent mineralisation in each lithofacies. Petrographic evidence also suggests further Fe mobilization in the ferruginous quartzite lithofacies (Figure 4.10c) and in the Sishen red shale unit (Figure 4.11c).

6.4. Provenance Considerations

Taylor & McLennan (1985) recognised that the fundamental motivation in examining chemical compositions of terrigenous clastic sedimentary rocks is to constrain the composition of the provenance or source rocks. Sedimentation involves complex chemical and physical processes which include weathering, chemical and physical erosion, transportation, deposition and lithification (including diagenesis and possibly metamorphism). It is therefore important to attempt to quantify the chemical effects that such processes may have on sedimentary rocks in order to best isolate the elements which preserve a record of the source rock composition (Rudnick and Gao, 2003).

6.4.1. K-addition

The effects of K metasomatism can be elucidated through the use of the A-CN-K diagram as introduced in Fedo *et al.* (1995, 1997; Figure 6.3). Because the source of the Gamagara shales is not clearly defined, comparisons have been made against both the weathering trends of the Ongeluk lavas (following section 1.3.6) and that of Paleoproterozoic upper continental crust (UCC; Condie, 1993) as shown in the ternary diagram in Figure 6.3. Arrows (a) and (b) show the weathering trends for the Ongeluk and UCC respectively which are predicted from kinetic leaching rates (Nesbitt and Young, 1984). If the shales

are weathering products of anything between Ongeluk andesites and UCC, then they are likely to plot in the space between lines (a) and (b) as seen by the aluminous/black and ferruginous units. Added to the data of the Sishen red shales and Paling shales (see section 5.3 for values) is the Mapedi shales and Ongeluk paleo-weathering profile (as found in Land *et al.*, in review). These additions were made as the CIA values are in strong agreement with this data (average = 74.2; standard dev. = 4.3; n = 99). Together, this average plots well below the predicted trends and show considerably more potassium than expected as represented by the black star in Figure 6.3.

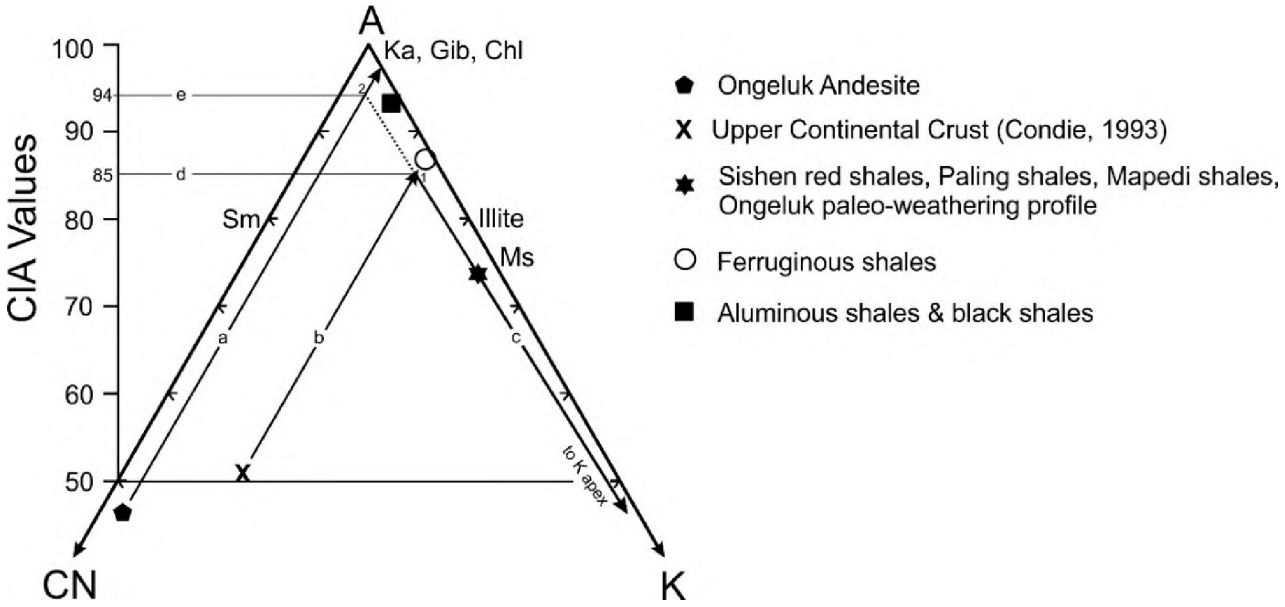

Figure 6.3: CIA ternary diagram including averages from the Gamagara and Mapedi stratigraphy. Mapedi shale average and the Ongeluk paleo-weathering profile (Drakenstein) lie at the same position as the average Sishen red and Paling shale members of the Gamagara. UCC represents a restoration model for average chemical composition of upper continental crust for ages 2.5 – 1.8 Ga (data extracted from Table 4 of Condie, 1993).

Fedo *et al.* (1995) noted that K-metasomatism in shales involves the addition of K_2O to aluminous clays and, as K increases, its trend would follow a path towards the K-apex of the ternary plot. A line drawn from the average composition of the Sishen red/Paling shale towards the K-apex (arrow c) follows the trend of potassium metasomatism. Because both the Ongeluk andesite and UCC were used as potential source rocks for the Gamagara shales, two interceptions at (1) and (2) represent its pre-metasomatised composition. A paleo-weathering index, corrected for K enrichment is determined by lines (d) and (e). A pre-metasomatised CIA value of 85 and 94 indicates the lower and upper limits of K-enrichment for the Sishen red and Paling shales respectively. These values indicate that the shales have gained between 11% and 21% of K_2O during metasomatism. If mixed sources are expected, the pre-metasomatised compositional range for Sishen red/Paling shales may fall anywhere on the dashed line.

6.4.2. Ce Anomalies

The presence of Ce anomalies in REE compositions may suggest the influence of sedimentary processes (e.g. McDaniel *et al.*, 1993 and references therein). Previous studies of soil-protolith profiles have identified fractionation of REE in regolith relative to parent rock and overall, saprolite is generally enriched in total REE (González-Álvarez and Kerrich , 2010 and references therein). In part, there is an enrichment of LREE but depletion in HREE due to preferential removal of HREE by complexation reactions involving inorganic and/or organic ligands (González-Álvarez and Kerrich, 2010). Generally, the REE's exist in the +3 valence state, however, during weathering, Ce may be oxidised to Ce^{4+}, which is more readily incorporated into insoluble oxides (e.g. cerianite) producing a positive Ce anomaly (McDaniel *et al.*, 1993). Such effects are not present in PAAS, Post-Archean Upper Continental Crust (PA-UCC) or North American Shale Composite (NASC) which incorporate all weathering-transport-diagenetic effects over many catchment-basin systems (González-Álvarez and Kerrich, 2010). Due to the fact that the samples are obtained from deep drill core and carefully prepared in laboratory conditions, these Ce anomalies are interpreted under the assumption that redox of Ce is not attributed to modern weathering.

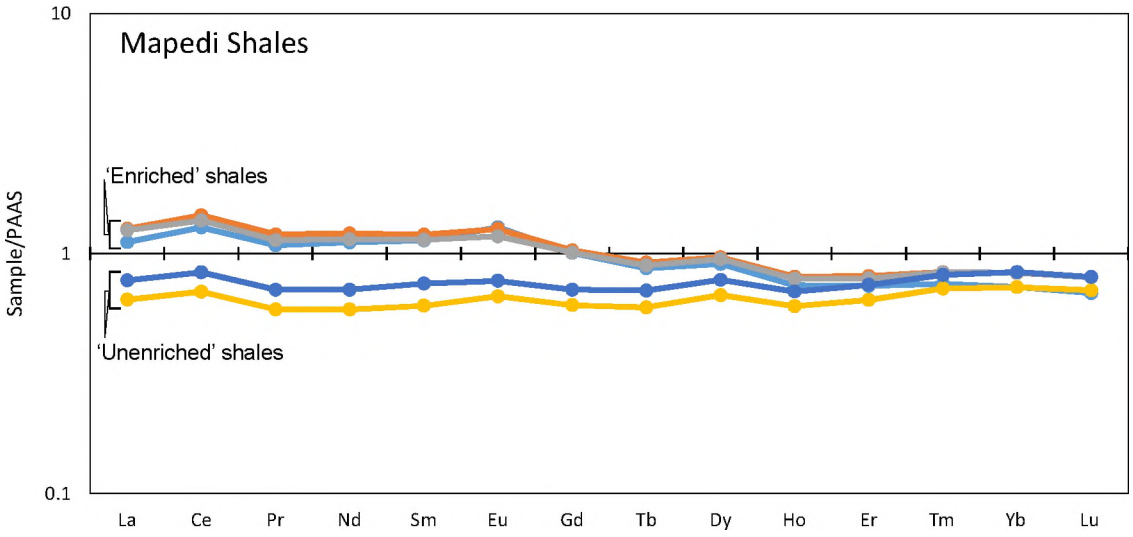

Figure 6.4: REE pattern for 'enriched' and 'unenriched' shales of the Mapedi Formation modified after Land *et al.* (in review). Note the Ce anomalies with Ce/Ce* values ranging between 1.15 and 1.17 in the enriched shales. The unenriched shales have the same Ce/Ce* of 1.13.

In the Gamagara, positive Ce anomalies are invariably present in only the Paling Shale Member which also feature weak to moderate LREE enrichment relative to HREE (Figure 5.3). Interestingly, the Mapedi Formation – a suggested correlative of the Gamagara – overlie extensive lateritic paleosols developed in the Ongeluk andesites. This paleo-weathering profile is described in detail in the works of

Wiggering and Beukes (1990) and more recently in the works of Land *et al.* (in review). The profile records an average Ce enrichment of 1.6 times that of the Ongeluk andesite (n = 10; calculated from data in Wiggering and Beukes, 1990). This suggests that a strong component of the Paling shales of the Gamagara Formation are most likely derived from the paleo-weathering profile developed in the Ongeluk andesites. Furthermore, on comparing the Mapedi Formations' REE pattern obtained from Land *et al.* (in review), positive Ce anomalies exist in both HFSE enriched and HFSE unenriched sections (Figure 6.4) suggesting that the Mapedi may be a lateral correlative of the Paling Member of the Gamagara Formation.

The Ce anomalies recorded in the ferruginous shale unit suggest that the oxidation of pyrite to hematite occurred primarily through weathering processes. This would have also allowed for the preferential removal of HREE by complexation reactions as discussed above and is demonstrated by the relatively flat REE baseline trend observed in this unit compared to that of the lower lying lithofacies which has an enriched HREE profile (Figure 5.3).

The Ce anomalies become not only important provenance indicators, but in this instance, add to pre-existing evidence to help correlate the stratigraphic placement of the Gamagara with the Mapedi Formation, placing the Mapedi as a lateral correlative of the Paling Shale member of the Gamagara Formation. This evidence confirms earlier works of Beukes and Smit (1987) who used petrographic and field observations to correlate these units.

6.4.3. HFSE Enrichment

Authigenic Ti-rich minerals (e.g. titanite, rutile, anatase) are found in mudstones under late diagenetic conditions (e.g. Hole *et al.*, 1992; Rasmussen and Glover, 1994; Pe-piper *et al.*, 2005; Pe-piper *et al.*, 2011). TiO_2 is widely regarded to have low to no mobility in sedimentary systems and is often used as a reference element against which mobile elements are compared (Taylor & McLennan, 1985; Nesbitt and Young, 1982). It is important to understand the conditions in which authigenic titania forms in order to help elucidate a basins history.

In sedimentary systems, fractionation of the HFSE and REE may occur under local conditions including that of (1) diagenesis at the sediment-water interface; (2) by detrital/biogenic dissolution and; (3) during breakdown of unstable detrital facies like volcanic debris (González-Álvarez and Kerrich, 2010). Evidence in the literature addressing HFSE fractionation conclude that the pH and chemistry of the carrier fluid are important and under highly saline oxidising environments with pH levels between 8 and 12, mobility may occur (Jiang *et al.*, 2005; González-Álvarez and Kerrich, 2010). In a study

involving authigenic titanite, Hole (1992) associates hydrothermal circulation in the form of halogen or carbonate complexes to be capable of mobilizing Ti-minerals. Pe-Piper (2011) characterized two varieties of authigenic titania, one occurring under eodiagenetic conditions in the presence of dissolved P to enhance Ti solubility, and the other forming under mesodiagenetic conditions in the presence of organic acids.

Table 6.1: Linear correlation coefficients (R^2) of Gamagara shales. Most values are taken from plots used in section 5.5.1.

Element Pair	DOORNFONTEIN Black	DOORNFONTEIN Ferruginous	SISHEN Red	PALING Green
Al_2O_3 - La	0.15	0.00	0.60	0.16
Al_2O_3 - Yb	-0.10	0.42	0.71	-0.15
TiO_2 - La	0.14	0.22	0.56	0.24
TiO_2 - Yb	-0.09	0.76	0.10	-0.02
P_2O_5 - La	-0.30	0.00	0.62	0.34
P_2O_5 - Yb	-0.70	0.13	0.78	0.57
Zr - La	0.11	0.14	0.71	0.06
Zr - Yb	0.73	0.79	0.49	0.00
S - La	0.15	-	-	-
S - Yb	0.65	-	-	-
Fe_2O_3 - LREE	-0.47	0.00	0.39	0.01
Fe_2O_3 - HREE	-0.69	-0.81	0.34	0.18
TiO_2 - Nb	0.91	0.97	0.87	0.75
TiO_2 - Zr	0.41	0.69	0.86	0.66
TiO_2 - P_2O_5	0.04	-0.01	0.60	-0.35
TiO_2 - Al_2O_3	0.54	0.56	0.05	0.37
TiO_2 - Nd	-	-	0.84	0.03
TiO_2 - Sm	-	-	0.87	0.00
P_2O_5 - Nd	-	-	0.48	0.65
P_2O_5 - Sm	-	-	0.50	0.71

HFSE enrichment occurs in the red shales of the Sishen member and to a lesser degree the aluminous shales of the Doornfontein Member (Figure 5.11). It has been demonstrated that in the red shales Ti has the strongest control over all the HFSEs and LREEs (Table 6.1). The modes of occurrence of titania in Figure 4.15 shows that not only is it authigenic, but more importantly that it is mobile, exploiting cleavage planes of phyllosilicates and precipitating in intergranular pore spaces. Authigenic fluorapatite grains are also always found proximal to the authigenic titania and in the cases where titania is spread along cleavage planes, the two minerals co-exist (Figure 4.15; Table 4.2). Furthermore, P_2O_5 always

correlates well with La, Yb, Ti, Nb and Zr in the Sishen red shale unit, indicating that P was involved during the HFSE enrichment.

The literature on the subject, along with the data provided and petrographic evidence all suggest the HFSE enrichments stem from diagenetic processes that possibly involve highly alkaline, F-bearing brines. As first suggested by Land et al. (in review), carbonates from the underlying Transvaal Supergroup may have buffered diagenetic fluids forming high pH solutions. These solutions in turn may have dissolved fluorine from the carbonates of the Campbellrand Subgroup or the Mooidraai Formation, resulting in a fluorine-rich oxidising brine, capable of transporting high concentrations of HFSE in solution. The evidence supporting microbial mat laminae, may also suggest organic ligands played an important role as dissolution of biogenic material would have occurred during diagenesis. Microbial mats are known to cause steep chemical gradients in the sediment and thus strongly influence diagenetic mineralization (Schieber, 1998 and references therein).

The shales of the Gamagara are by no means the only unit to show the highly enriched nature of HFSE in the stratigraphy. The Mapedi Formation, shown in this thesis to be the lateral correlative of the Gamagara's Paling Member shows the same anomalous HFSE enrichment (e.g. Land *et al.*, in review). The Paling Member of the Gamagara, however, does not show signs of this enrichment and such a notion is contradictory if this enrichment was interpreted as a primary 'source-to-sink' signature. In the study of Land *et al.* (in review) it was realised that, if this signal was indeed primary, this enriched unit was only possible if the provenance of the shales were dominated by Si-undersaturated alkali igneous rocks such as alkali basalt, nephelinite or basanite, a possibility which remains unfounded on regional geological grounds. As such, the enrichments were interpreted as metasomatic occurring under similar processes which are suggested above (Land *et al.*, in review).

At this point it must be reiterated that the Gamagara and Mapedi Formation lie directly above the regional unconformity separating the Manganore Formation in the south and the Hotazel Formation in the north respectively. It is now established that this HFSE signature is found on a regional scale in the Griqualand West basin and runs from Beeshoek (on the southern margin of the Maremane dome) through King/Sishen (on the northern margin of the Maremane dome) and up to Black Rock, some 70km further north of the Maremane dome (~140km N-S strike; Figure 1.2) The author suggests that the metasomatic processes involving HFSE mobility may have possibly exploited the unconformity as a fluid pathway, affecting the red shale unit of the Sishen Member in the south and the lateral correlative Paling Member (Mapedi) in the north.

6.4.4. Fe-addition

Grant's (2005) isocon analysis was selected for evaluating the chemical gains and losses in the samples by graphically plotting the altered shale (red band) against the original composition (white band; Figure 6.5). The graph shows the constant mass isocon at 45° while the immobility isocon was defined by linear regression passing through the origin. Gains in Fe_2O_3 (84%), MnO (46%), Ba (42%), Pb (42%), Zn (27%) and V (24%) along with losses of U (-500%) and Cu (-120%) were associated with the Fe mobilization. Immobile species include the remaining elements of which the REEs and Y (playing a large role in defining the immobility isocon), HFSEs, K_2O, P_2O_5 and ε_{Nd} are noteworthy as they indicate that the Fe-addition event occurred after the K and HFSE enrichment in these shales.

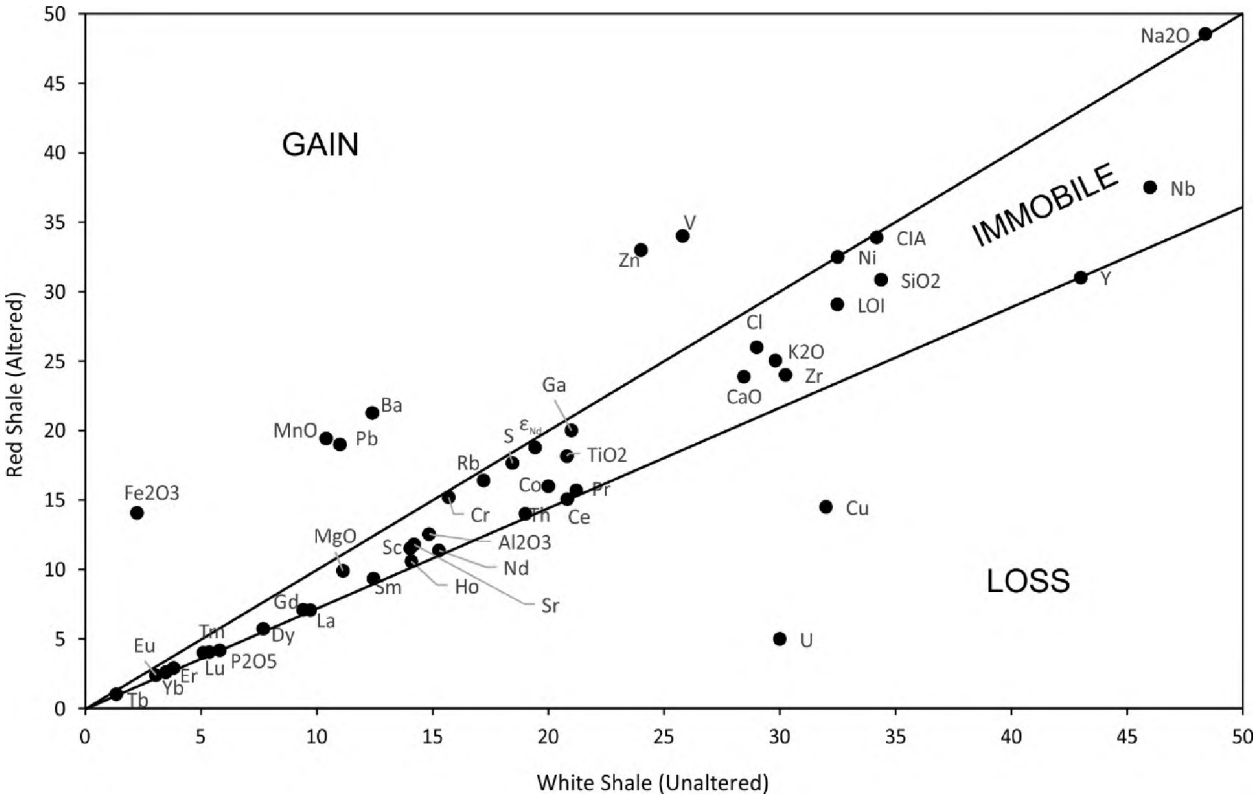

Figure 6.5: Isocon diagram for a red and white band of the Sishen Members' red shale. The constant mass isocon lies where x=y and indicates complete immobility of species. The immobility isocon was determined using linear regression. Elements plotting on or between the two isocons are defined as immobile in the system.

Robb (2005) outlines a model for Mississippi Valley-type (MVT) deposits, whereby oxidized fluids carrying Pb and Zn encounter organic matter and precipitation of the metals occur by means of sulphate reduction. In relatively low temperature environments (< 150°C), such as those related to the formation

of MVT deposits, considerable attention has been given to the roles that metal-organic complexes might have played in hydrothermal ore-forming processes (Robb, 2005). Given that microbial mats play a vital role in the creation of the red beds and ferruginous units of the Sishen Member, the involvement of organo-metallic complexes may be important controls of Pb, Zn and ultimately Fe mobilization. Furthermore, the strong correlation of U with organics is well known and has been exploited for many years as it may be used to estimate TOC content of shales with the use of gamma-ray logs (Potter, 2005). The author speculates that change in U levels occurred as the fluids carrying the metals were capable of oxidizing immobile U^{4+} into mobile U^{6+} and thus simultaneously removed it from the unaltered host rock.

6.4.5. Nd Isotopes

Diagenetic modifications involving trace phosphatic phases (e.g. diagenetic apatite, monazite, xenotime etc.) especially in organic-rich sedimentary rocks have been shown to have a profound influence on REE abundances and the Sm-Nd isotope system on mineralogical and whole-rock scale (McLennan *et al.*, 2003). If open-system conditions persist (on a scale greater than a hand sample), REE and U will take on non-conservative behaviours and affect the primary sedimentary signal (McLennan *et al.*, 2003). It has been noted that addition of about 10% apatite phase will create a significant change in the whole-rock REE patterns and as little as 0.1% addition of monazite would bring about a change in the whole-rock REE pattern that would not be mistaken for unaltered shale (McLennan *et al.*, 2003)

A consequence of altered REE patterns in shale is that the $^{147}Sm/^{144}Nd$ is changed and effects the evolution of the Sm-Nd isotopic system and the Nd model age (T_{DM}) used in provenance studies (Bock *et al.*, 1994). The relation allows diagenetically altered shales to be identified when compared with unaltered shales from a related sequence (McLennan *et al.*, 2003). The addition/subtraction of diagenetic apatite/monazite will cause rocks to follow a predictable pathway in a T_{DM} *versus* $^{147}Sm/^{144}Nd$ space, originating from the initial unaltered position of the shale (McLennan *et al.*, 2003). Such processes have been documented well in the literature and demonstrate the importance of diagenetic phases (common in shales). The recognition of which, allows the shales to be evaluated in the context of their diagenetic history and provides additional information about the history of the sedimentary rock (McLennan *et al.*, 2003). It must be said that in sediments with complex provenance, bulk rock Nd isotopes may be representative of the provenance as a whole. A source with high concentrations of an element may drown out the signal of a source with low concentrations of that same element and one technique may be inadequate for reliable provenance information (McLennan *et al.*, 2003).

With the recognition of the altered shales of the Gamagara having already been establish and discussed above, its isotopic information may provide us with valuable information about the age of alteration while the unaltered Paling Member shales may rather refer to an original provenance age. Whole rock Pb-Pb ages of the Ongeluk lavas are calculated at ~2.22 Ga (Cornell *et al.*, 1996), however, based on the minimum age determinations at ca. 2394 Ma on the overlying Mooidraai Formation dolomites, controversy surrounds this age and older ages for the Ongeluk have been suggested before (Moore *et al.*, 2001, 2012; Bau *et al.*, 1999). This however requires a challenging revision of stratigraphic correlations between the basins preserving the Transvaal Supergroup (Kampmann *et al.*, 2015).

Table 6.2: Nd isotopic compositions and calculated T_{DM} ages for the Ongeluk Formation.

Formation	Sample*	Type*	$^{143}Nd/^{144}Nd$*	ε_{Nd}*	Sm* (ppm)	Nd* (ppm)	$^{147}Sm/^{144}Nd$	T_{DM} (Ga)
Ongeluk	77394	Pillow Core	0.511539	-21.4381	3.39	16.89	0.12082771	2.46
	77395	hyaloclastite	0.511525	-21.7112	2.975	15.38	0.11644668	2.38
	77397	Massive lava	0.511532	-21.5747	3.666	18.9	0.11676889	2.37

*Data obtained from Cornell et al., 1996

Table 6.2 shows whole rock Sm-Nd data for the Ongeluk Formation derived from Cornell *et al.* (1996) with new T_{DM} model ages calculated based on the information provided. Interestingly, the ages fall close to or within range of the calculated T_{DM} model ages obtained in the Paling Member shales (2.27 - 2.39 Ga; Table 5.1). Furthermore, in a recent geochronological and paleomagnetic study by Kampmann *et al.* (2015), a suite of dolerite sills intruding into the Kuruman Iron Formation were sampled and precise U–Pb baddeleyite ages of 2441 ± 6Ma and 2426 ± 1 Ma were obtained. The study speculates that the dolerites, named the Westerberg Sill Suite, may be stratigraphically deeper intrusive equivalents of the Ongeluk volcanic rocks. If such information is correct, it could suggest that the Ongeluk may contribute towards a likely provenance

The differences in the REE patterns combined with the Nd isotope characteristics of the Sishen Members red shales indicates Sm-Nd were fractionated. The age of the isotopic disturbance is indicated by the T_{DM} ages provided in Table 5.1 (1.73 – 1.86 Ga). It is noteworthy to mention that the only age close to this within a regional context is the 1.92 Ga felsic volcanics of the Neylan-Hartley succession of the Olifantshoek Supergroup (Table 1.1), an age which defines the upper limit of Gamagara Formation. Unfortunately, no ages have been determined on the volcanic units overlying the red shales of the Sishen Member (previously described as Ongeluk thrust lavas – see section 3.2.3) as such an event may provide further insight into this alteration.

7. CONCLUSIONS

All conclusions are inferred by the author following the evidence provided in the sections above.

(1) The shales of the Gamagara Formation represent a tide-dominated delta which provided an environment conducive to microbial mat growth.

(2) Lavas overlying the Sishen red shale unit represent a period of mafic volcanism following the outflow of the Ongeluk lavas and are not thrust emplaced as previously suggested.

(3) Hydrothermal fluids are responsible for the mineralization evident in the aluminous shale unit. The fluids involved were capable of mobilizing Al and Ti and slightly enriched HFSEs in this lithofacies.

(4) Black pyritic shales provide good evidence for microbial mat growth and formed the precursors to the ferruginous lithofacies. Ce anomalies and preferential HREE removal indicate the ferruginous lithofacies underwent weathering following the replacement of pyrite by hematite.

(5) Based on Ce anomalies and REE patterns, the Mapedi Formation is likely to be the lateral correlative of the Paling Member of the Gamagara Formation. REE patterns and Nd-isotopes suggest both units are primarily derived from the underlying Ongeluk paleoweathering profile.

(6) Highly alkaline F-bearing brines altered the red shales of the Sishen Member and shales of the Mapedi Formation. The fluids had the ability to mobilize titania and fluorapatite, reset Nd isotope systematics and ultimately enrich HFSE concentrations in this unit. This event possibly represents unconformity related fluid flow on a regional scale.

(7) K-metasomatism affected the red shales of the Sishen Member, Paling Member and Mapedi Formation. This event also affected the underlying paleoweathering profile of the Ongeluk Formation.

(8) Fe-addition occurred as a separate event following the HFSE enrichment by epigenetic mechanisms similar to those of MVT-type deposits.

(9) Nd-isotopes record an isotopic disturbance concurrent with the HFSE enrichment. T_{DM} model ages suggest disruption (and enrichment) occurred between 1.73 and 1.86 Ga.

7.1. Concluding Remarks

A significant conclusion reached here is the proposal of microbial mat growth in the Gamagara Formation. It has been noted by Schieber (1998) that to have any chance of conclusively proving the existence of organosedimentary structures in Precambrian terrigenous clastics, one will first have to

identify localities where such a quest has a chance to succeed. The Griqualand West basin is host to some of the World's best preserved Proterozoic cover successions and as such may help to tighten sedimentological and textural criteria for mat recognition. Furthermore, the number of features pointing to microbial traces that are encountered simultaneously in the same sediment layer, lends to an increasingly attractive microbial mat interpretation.

Although at the moment the evidence available for microbial mats in the Proterozoic terrigenous sediments may not satisfy the stringent criteria for palaeomicrobiologists, it should not detract one from seriously entertaining the possibility in their investigations (Schieber, 1998 and references therein). Ignoring the indications of microbial mats could significantly handicap sedimentological interpretations and lead to erroneous conclusions as its structure significantly decreases erosion resistance in sediment layers, traps a variety of grain sizes in its gelatinous texture, and causes steep chemical gradients that influences diagenetic mineralisation. The indications that microbial mat deposits exist in the Gamagara gives future research the option of an alternate working hypothesis that may eventually lead to more comprehensive interpretations of ones data.

Hydrothermal modifications in various units of the Gamagara seem to have occurred at different stages rather than as one single event. This is true particularly for the Sishen red shale unit which records HFSE, K and Fe enrichments. The presence of K-enrichment in the Paling Member (without HFSE enrichment) perhaps suggests it was the earliest alteration episode. As the HFSE enrichment occurs in both the Fe-rich and Fe-poor bands of the Sishen red shale, one can assume that the HFSE enrichment occurred prior to Fe-addition. The link between the alteration seen in the aluminous shale unit and overlying units remains elusive. This unit is the lowest lying shale facies so if the unconformity played a major role in fluid migration, speculation arises that this alteration may be casually linked to the overlying sediments. In this scenario, the primary (pre-metasomatic) shales responded differently to fluids as they circulated through the stratigraphy, leaving behind the resultant lithologic variations encountered today.

Regardless of the gaps in the current understanding, a key implication in the present study relates to South Africa's largest iron ore reserve which is typically found at the unconformity that separates the shales of the Gamagara Formation from the Transvaal Supergroup: If the Gamagara indeed records large scale fluid metasomatism, the possibility then arises that the genesis and/or epigenetic modification of the iron ores of the Transvaal Supergroup may at least be casually linked to the same fluid-migration event/s.

7.2. Recommendations

There is scope for additional geochemical and petrographic work to be conducted on the aluminous shale unit, particularly on core HR4/98 which preserves the thickest encountered package of intercalated black and aluminous shales. The presence of fine-grained microquartz (chert) occurring both as nodules and as rhythmic beds intercalated with black shales is tantalising and requires more detailed examination (refer to Boggs, 2009, pg. 474 and Maliva *et al.*, 2005). As the data set in the black and ferruginous lithofacies is scarce, additional geochemical work is recommended to locate more meaningful statistical relationships where they may occur. The aforementioned lithofacies are particularly important as they are the lowest lying argillaceous units, occurring closest to the unconformity.

8. REFERENCES

Assmang. (2005). Beeshoek Iron Ore Report 12/04/2005. Retrieved from: http://www.arm.co.za/im/files/presentations/2005/black_rock_beeshoek_visit12apr05_ii.pdf. (Accessed February 2014).

Bau, M., Romer, R.L., Lüders, V., Beukes, N.J. (1999). Pb, O, and C isotopes in silicified Mooidraai dolomite (Transvaal Supergroup, South Africa): Implications for the composition of Paleoproterozoic seawater and dating the increase of oxygen in the Precambrian atmosphere: Earth and Planetary Science Letters, v. 174, p. 43–57.

Bauld, J., Johns, I.A., Plumb, L.A., Reed, M.R., Skyring, G.W. (1980) Sulphate reduction in algal mat sediments. Baas Becking Geobiol. Lab. Annu. Rep. 1980, pp. 21-25.

Beukes, N.J. and Smit, C.A. (1987). Evidence for thrust faulting in Griqualand West, South Africa: Implications for stratigraphy and the age of the red beds. *Geol. Soc. S. Afr. Trans.*, **90**, 378-394.

Beukes, N.J., Dorland, H.C., Gutzmer, J., Nedachi, M. and Ohmoto, H. (2002) Tropical laterites, life on land and the history of atmospheric oxygen in the Paleoproterozic. Geology, 30, 491-494.

Beukes, N.J., Gutzmer, J., Mukhopadhyay, J. (2003). The geology and genesis of high-grade hematite iron ore deposits. Trans. Inst. Min Metall. B, 112(April).

Boggs, S., Jr. (2009). Petrology of Sedimentary Rocks. Cambridge University Press. London. 600 pp.

Cairncross, B. and Beukes, N.J. (2013). *The Kalahari Manganese Field, The Adventure Continues.* Struik Nature, Cape Town, 384 pp.

Condie, K. C. (1991). Another look at rare earth elements in shales. *Geochemica et Cosmochimica Acta,* 55, pp. 2527-2531.

Condie, K. C. (1993). Chemical composition and evolution of the upper continental crust: Contrasting results from surface samples and shales: Chemical Geology, v. 104, p. 1–37.

Cornell, D.H., Schutte, S.S., and Eglington, B.L. (1996). The Ongeluk basaltic andesite formation in Griqualand West, South Africa: Submarine alteration in a 2222 Ma Proterozoic sea: Precambrian Research, v. 79, p. 101–123.

Da Silva, R. (2011). Distribution and Geochronology of Unconformity-Bound Sequences in Paleoproterozoic Elim-Olifantshoek Red Beds : Implications for Timing of Formation of Sishen-Type Iron Ore and Heavy Carbonate Carbon Isotope Excursion. M.S. thesis (unpub.), University of Johannesburg, 103 pp.

De Villiers, J.E. (1967). New stratigraphic correlation and interpretation of the geological structure of the Postmasburg-Sishen area. *Annals geol. Surv. S. Afr.*, **2**, 280pp.

DePaolo, D.J. (1988). Neodymium Isotope Geochemistry, An Introduction. Springer-Verlag, Berlin, 187 pp.

Dorland, H. (1999). Paleoproterozoic laterite, red beds and ironstone of the Pretoria Group with reference to the history of atmospheric oxygen [M.S. thesis]: Johannesburg, Rand Afrikaans University, 147 p.

Eriksson, P.G., Altermann, W. and Hartzer, F.J. (2006). *In*: Johnson, M.R., Anhaeusser, C.R. and Thomas, R.J. (Eds.) (2006). *The Geology of South Africa.* Geological Society of South Africa, Johannesburg/Council for Geoscience, Pretoria, p. 237-260.

Eriksson, P.G., Schieber, J., Bouougri, E.,.Gerdes, G., Porada, H., Banerjee, S., Bose, P.K. and Sarkar, S. (2007). Classification of Structures Left by Microbial Mats in Their Host Sediments. *In* Eriksson, P.G., Banerjee, S., Sarkar, S., Altermann, D.N., and Catuneanu, O., (Eds.) Schieber *et al.* (Eds.), *Atlas of Microbial Mat Features Preserved within the Siliciclastic Rock Record*. Elsevier, Amsterdam, p. 39-52.

Faure, G. and Mensing, T.M. (2005). *Isotopes: Principles and Applications*. John Wiley & Sons. 897 pp.

Fedo, C. M.; Nesbitt, H. W. and Young, G. M. (1995). *Unraveling the effects of potassium metasomatism in sedimentary rocks and paleosols, with implications for paleoweathering conditions and provenance*: Geology, v. 23, p. 921–924.

Fedo, C. M.; Young, G. M., Nesbitt, H. W. and Hanchar, J.M. (1997). *Potassic and sodic metasomatism in the Southern Province of the Canadian Shield: Evidence from the Paleoproterozoic Serpent Formation, Huronian Supergroup, Canada*. Precambrian Research v. 84, p. 17-36, Elsevier Science B.V.

Fralick, P. (2003). *Geochemistry of clastic sedimentary rocks: ratio techniques*, in, Lentz, D.R., ed., Geochemistry of Sediments and Sedimentary Rocks: Evolutionary Considerations to Mineral Deposit-Forming Environments. Geological Association of Cananda. Geotext 4, p. 85-103.

González-Álvarez, I., & Kerrich, R. (2010). *REE and HFSE mobility due to protracted flow of basinal brines in the mesoproterozoic Belt-Purcell Supergroup, Laurentia. Precambrian Research*. v. 177, p. 291-307.

Grant, J.A. (2005). *Isocon analysis: A brief review of the method and applications*. Physics and Chemistry of the Earth v. 30, p. 997–1004.

Grobbelaar, W., Burger, M. and Pretorius, A. (1995). *Stratigraphic and structural setting of the Griqualand West and the Olifantshoek Sequences at Black Rock, Beeshoek and Rooinekke Mines, Griqualand West, South Africa*. Mineralium Deposita, v. 161, p.152–161.

Gutzmer, J. and Beukes, N.J. (1998). *Earliest laterites and possible evidence for terrestrial vegetation in the Early Proterozoic*. Geology. v. 23, p. 263-266.

Gutzmer, J., Chisonga, B.C., Beukes, N.J. and Mukhopadhyay, J. (2008). *The Geochemistry of BIF-hosted High-Grade Hematite-Martite Iron Ores*. Reviews in Economic Geology, v. 15, p. 157-184.

Gutzmer, J., Chisonga, B.C., Beukes, N.J. and Mukhopadhyay, J. (2008). *The Geochemistry of BIF-hosted High Grade Hematite-Martite Iron Ores*. Reviews in Economic Geology, v. 15, p. 157-184.

Hall, R.B. (1978). *World non-bauxite Al-resources-alunite*. U.S. Geol. Surv. Prof. Pap., v. 1076A, 35 pp.

Hole, M.J., Trewin, N.H. and Still, J. (1992). *Mobility of the high field strength, rare earth elements and yttrium during late diagenesis.* Journal of the Geological Society of London.

Holland, H.D. and Beukes, N.J. (1990). *A paleoweathering profile from Griqualand West, South Africa: evidence for a dramatic rise in atmospheric oxygen between 2.2 and 1.9 bybp*. Am. J. Sci, v. 290-A, p.1–34.

Jiang, S., Wang, R., Xu, X., and Zhao, K. (2005). *Mobility of high field strength elements (HFSE) in magmatic-, metamorphic-, and submarine-hydrothermal systems*. Physics and Chemistry of the Earth v. 30, p. 1020-1029.

Kalumbu, J. (2006). *Geochemistry, mineralogy and petrography of Paleoproterozoic red and green shales of the Mapedi Formation, Olifantshoek Group, South Africa*. Hons Thesis (unpub.), Rhodes Univ., Grahamstown.

Kampmann, T.C., Gumsley, A.P., de Kock, M.O. and Söderlund, U. (2015). *U–Pb geochronology and paleomagnetism of the Westerberg Sill Suite, Kaapvaal Craton – Support for a coherent Kaapvaal–Pilbara Block (Vaalbara) into the Paleoproterozoic?* Precambrian Research, v. 269, Elsevier, p. 58-72.

Kirschvink, J. L., Gaidos, E. J., Bertani, L. E., Beukes, N. J., Gutzmer, J., Maepa, L. N., and Steinberger, R. E. (2000). *Paleoproterozoic snowball earth: extreme climatic and geochemical global change and its biological consequences.* Proceedings of the National Academy of Sciences of the United States of America, v. 97(4), p. 1400–5.

Land, J. (2010). *The Geochemistry of paleosols and "red beds" in the Transvaal and Olifantshoek Supergroups: provenance versus metasomatism.* Hons Thesis (unpub.), Rhodes Univ., Grahamstown.

Land, J.S., Tsikos, H., Cousins, D.P., Luvizotto, T.Z. and Beukes, N.J. (In review). *Origin of paleosols and red beds in the Palaeoproterozoic Transvaal and Olifantshoek Supergroups of South Africa: provenance versus metasomatic controls*. Geological Journal, Wiley.

Maliva, R.G., Knoll, A.H. and Simonson, B.M. (2005). *Secular change in the Precambrian silica cycle: Insights from chert petrology.* GSA Bulletin; July/August 2005; v. 117; no. 7/8; p. 835–845.

McDaniel, D.K., Hemming, S.R., McLennan, S.M. and Hanson, G.N. (1993). *Resetting of neodymium isotopes and redistribution of REEs during sedimentary processes: the early Proterozoic Chelmsford Formation, Sudbury basin, Ontario, Canada*. Geochim. Cosmochim. Acta v. 58, p. 931–941.

McLennan, S. M., Bock, B., Hemming, S. R., Hurowitz, J. A., Lev, S. M. and McDaniel, D. K. (2003). *The roles of provenance and sedimentary processes in the geochemistry of sedimentary rocks, in Lentz, D.R., ed., Geochemistry of Sediments and Sedimentary Rocks: Evolutionary Considerations to Mineral Deposit-Forming Environments*. Geotext v. 4, p. 7-38.

Míková, J. and Denková, P. (2007). *Modified chromatographic separation scheme for Sr and Nd isotope analysis in geological silicate samples*. J Geosci. v. 52: p. 221–226.

Moen, H.F.G. (2006). *The Olifantshoek Supergroup*. In: Johnson, M.R., Anhaeusser, C.R. & Thomas, R.J. (Eds.) (2006). The Geology of South Africa. Geological Society of South Africa, Johannesburg/Council for Geoscience, Pretoria, p. 319-24.

Moore, J. M., Polteau, S., Armstrong, R. a., Corfu, F., and Tsikos, H. (2012). *The age and correlation of the Postmasburg Group, southern Africa: Constraints from detrital zircon grains.* Journal of African Earth Sciences, v. 64, p. 9–19.

Moore, J., Tsikos, H. and Polteau, S. (2001). *Deconstructing the Transvaal Supergroup, South Africa: implications for Palaeoproterozoic palaeoclimate models.* Journal of African Earth Sciences, v. 33 (2001), p. 437–444.

Nel, T. (1929). *The geology of the Postmasburg manganese deposits and surrounding country. An explanation of the geological map.* Spec. Publ. geol. Surv. S. Afr., v. 7, 109 pp.

Nesbitt, H. W. and Young, G. M. (1982). *Early Proterozoic climate and plate motions inferred from major element chemistry of lutites.* Nature v. 299, p. 715-717.

Nesbitt, H. W. and Young, G. M. (1984). *Prediction of some weathering trends of plutonic and volcanic rocks based on thermodynamic and kinetic considerations*. Geochim. Cosmochim. Acta v. 48, p. 1523-1534.

Nichols, G. (2009). *Sedimentology and Stratigraphy*. Wiley-Blackwell, Oxford, UK, 432 pp.

Norrish K. and Hutton J. T. (1969). *An accurate X-ray spectrographic method for the analysis of a wide range of geological samples.* Geochim. Cosmochim. Acta v. 33, 43 I 454 pp.

Pe-Piper, G., Karim, A. and Piper, D.J.W. (2011). *Authigenesis of Titania Minerals and the Mobility of Ti: New Evidence from Pro-deltaic Sandstones, Cretaceous Scotian Basin, Canada.* Journal of Sedimentary Research, v. 81, p. 762–773.

Pe-Piper, G., Piper, D.J.W., and Dolansky, L.M. (2005). *Alteration of ilmenite in the Cretaceous sands of Nova Scotia, southeastern Canada*: Clays and Clay Minerals, v. 53, p. 490–510.

Polteau, S., Moore, J.M. and Tsikos, H. (2006). *The geology and geochemistry of the Palaeoproterozoic Makganyene diamictite*. Precambrian Research, v. 148(3-4), p. 257–274.

Potter, P.E., Maynard, J.B. and Depetris, P.J. (2005). *Mud and Mudstones: Introduction and Overview*. Springer. New York. 297 pp.

Rasmussen, B., and Glover, J.E. (1994). *Diagenesis of low-mobility elements (Ti, REEs, Th) and solid bitumen envelopes in Permian Kennedy Group sandstone, Western Australia.* Journal of Sedimentary Research, v. 64, p. 752–783.

Robb, L. (2005). *Introduction to Ore-Forming Processes*. Blackwell Publishing, London. 373 pp.

Rollinson, H.R. (1993). *Using Geochemical Data: Evaluation, Presentation and Interpretation*. Longman, Harlow, 352 pp.

Rudnick, R.L. and Gao, S. (2003). *The composition of the continental crust.* In: Rudnick, R.L., Holland, H.D., Turekian, K.K. (Eds.), The Crust. Treatise on Geochemistry, v. 3. Elsevier, Oxford, New York, p. 1–64.

Schalkwyk, G.A.C. (2005). *Genesis and characteristics of the Wolhaarkop breccia and associated Manganore iron formation*. M.S. thesis (unpub.), University of Johannesburg, 97 pp.

Schieber, J. (1986). *The possible role of benthic microbial mats during the formation of carbonaceous shales in shallow Proterozoic basins*: Sedimentology, v. 33, p. 521-536.

Schieber, J. (1989). *Facies and origin of shales from the Mid-Proterozoic Newland Formation, Belt basin, Montana, U.S.A.*: Sedimentology, v. 36, p. 203-219.

Schieber, J. (1998). *Possible indicators of microbial mat deposits in shales and sandstones: Examples from the Mid-Proterozoic Belt Supergroup, Montana, U.S.A.* Sedimentary Geology, v. 120, p. 105-124.

Schieber, J. (1999). *Microbial Mats in Terrigenous Clastics: The Challenge of Identification in the Rock Record*. Palaios, v. 14, p. 3-12.

Schieber, J. (2004). *Microbial Mats in the Siliciclastic Rock Record: A Summary of Diagnostic Features*. In: Eriksson, P.G., Altermann, D.N., Mueller, W.U., Catuneanu, O. and Strand, K., Eds., The Precambrian Earth: Tempos and Events. Developments in Precambrian Geology, Elsevier, p. 663-672.

Schütte, S.S. (1992). *Ongeluk volcanism in relation to the Kalahari manganese deposits*. M.S. thesis (unpub.), University of Johannesburg. Retrieved from https://ujdigispace.uj.ac.za (Accessed: February 2014).

Shivute, F.M. (2006). *Mineralogy, Petrography and Geochemistry of the Shales of the Gamagara Formation, Postmasburg area, Northern Cape Province, South Africa*. Hons Thesis (unpub.), Rhodes Univ., Grahamstown.

Stow, D.A.V. (2005) *Sedimentary Rocks in the Field: A colour guide*. Manson Publishing Ltd., London. 318 pp.

Strauss, C.A. (1964). T*he iron deposits of Sishen area, Cape Province*, 393-403. In: Haughton, S.H., Eds., The Geology of Some Ore Deposits in Southern Africa, II. Geol. Soc. S. Afr., Johannesburg, 793 pp.

Sumner, D.Y. and Beukes, N.J. (2006). *Sequence Stratigraphic Development of the Neoarchean Transvaal carbonate platform, Kaapvaal Craton, South Africa*. South African Journal of Geology, v. 109, p. 11-22.

Tanaka T, Togashi, S., Kamioka, H. and Et, M. (2000). *JNdi-1: a neodymium isotopic reference in consistency with LaJolla neodymium*. Chemical Geology, v. 168, p. 279–281.

Taylor, S. R., and McLennan, S. M. (1985). *The continental crust: Its composition and evolution.* Oxford: Blackwell.

Tsikos, H., Beukes, N.J., Moore, J.M. and Harris, C. (2003). *Deposition, Diagenesis, and Secondary Enrichment of Metals in the Paleoproterozoic Hotazel Iron Formation, Kalahari Manganese Field, South Africa.* Economic Geology, v. 98, p. 1449-1462.

Van Deventer, W.F. (2009). *Textural and geochemical evidence for a supergene origin of the Paleoproterozoic high-grade BIF-hosted iron ores of the Maremane Dome, Northern Cape Province, South Africa.* M.S. thesis (unpub.), University of Johannesburg. Retrieved from https://ujdigispace.uj.ac.za (Accessed: October 2014).

Van Niekerk, H.S. (2006). *The origin of the Kheis Terrane and its relationship with the Archean Kaapvaal Craton and the Grenvillian Namaqua Province in southern Africa*. Ph.D. thesis (unpub.), University of Johannesburg.

Van Schalkwyk, J. F. and Beukes, N.J. (1986). *The Sishen iron ore deosit, Griqualand West*, p. 931 – 956, in Mineral Deposits of Southern Africa, I. Eds: CR Anhaeusser and S Maske. 1020 pp. Geological Society of South Africa: Johannesburg.

Van Schalkwyk, J.F. (1984). *Die Geologie van die Sishen-Ysterertsmyn*. M.S. thesis (unpub.), University of Johannesburg. Retrieved from https://ujdigispace.uj.ac.za (Accessed: October 2014).

Visser, D.J.L. (1944). *Stratigraphic features and tectonics of portions of Bechuanaland and Griqualand West*. Trans. Geol. Soc. S. Afr., v. 47, p. 197-254.

Wiggering, H., and Beukes, N.J. (1990). *Petrography and geochemistry of a 2000–2200 Ma-old hematitic paleo-alteration profile on Ongeluk basalt of the Transvaal Supergroup, Griqualand West, South Africa*: Precambrian Research, v. 46, p. 241–258.

Yamaguchi, K. and Ohmoto, H. (2006). *Geochemical and isotopic constraints on the origin of Paleoproterozoic red shales of the Gamagara/Mapedi Formation, Postmasburg Group, South Africa*. South African Journal of Geology, v. 109, p.123–138.

Zimmerman, U., Lamprecht, A., Beukes, N.J., Gutzmer J. and Miyazaki, T. (2008). *Provenance of the paleoproterozoic Gamagara/Mapedi red bed succession and its implication for the evolution of the Kaapvaal Craton.* International Geological Congress 33, Oslo.

APPENDIX A BULK ROCK XRF DATA

CORE IO2/85

Sample	IO17	IO16	IO15	IO14	IO12	IO11	IO10	IO9	IO8	IO5	IO3	IO2	IO1
Depth (m)	175.02	177.75	188.15	198.73	219.7	237.5	243.9	260.5	270.21	288.4	294.25	298.08	311.7
SiO_2	65.758	63.949	65.222	61.843	66.957	58.092	53.257	59.363	58.193	57.448	61.684	44.274	51.397
TiO_2	0.856	0.825	0.728	0.695	0.823	0.871	0.809	1.107	1.007	0.843	0.568	0.633	0.607
Al_2O_3	16.470	15.900	15.725	15.310	15.359	18.755	16.664	16.780	19.606	17.251	14.332	15.206	14.554
Fe_2O_3	3.845	7.272	5.449	8.915	4.945	11.216	14.499	9.998	11.053	16.360	16.018	35.535	26.166
MnO	0.095	0.026	0.036	0.015	0.074	0.010	0.023	0.093	0.017	0.017	0.015	0.026	0.048
MgO	2.044	1.546	1.675	1.791	1.390	1.147	1.286	1.364	1.019	0.515	0.455	0.093	0.460
CaO	0.357	0.444	0.949	0.457	0.108	0.212	0.337	0.208	0.076	0.081	0.175	0.038	0.145
Na_2O	0.578	0.626	0.581	0.361	0.226	0.082	0.087	0.098	0.110	0.083	0.027	0.028	0.026
K_2O	6.514	6.261	6.587	6.821	5.223	4.664	5.341	4.648	5.169	3.783	3.610	0.674	3.732
P_2O_5	0.180	0.167	0.640	0.262	0.034	0.116	0.167	0.082	0.063	0.049	0.174	0.101	0.131
LOI	3.700	2.930	3.490	3.690	4.030	3.890	6.860	5.690	3.340	3.140	2.620	2.830	2.490
H_2O^-	0.570	0.480	0.670	1.000	1.200	1.050	1.010	1.160	1.030	0.990	0.670	0.440	0.670
Total	100.967	100.426	101.752	101.160	100.369	100.105	100.340	100.591	100.683	100.560	100.348	99.878	100.426
Nb	18.1	18.2	14.4	13.4	15.3	28.9	25.2	30.4	25.7	17.3	11.6	13.0	11.1
Zr	175.3	175.5	137.0	127.8	232.9	237.2	214.1	246.1	201.7	184.7	182.9	159.7	146.3
Y	41.4	42.0	49.7	26.3	27.3	36.7	30.7	25.3	22.1	23.1	21.7	22.6	21.3
Sr	50.0	54.2	43.2	32.7	37.5	40.2	51.5	63.6	148.7	146.8	209.2	300.0	197.3
U	1.8	2.3	1.9	2.4	2.1	1.0	1.4	2.8	1.4	2.3	0.8	0.9	1.8
Rb	238.0	233.3	203.8	210.1	139.7	166.0	198.1	201.6	214.0	166.3	137.1	25.8	129.5
Th	18.8	17.8	15.1	12.8	11.6	25.2	21.3	18.3	21.1	15.8	15.0	20.0	20.7
Pb	3.3	4.8	7.1	3.3	19.5	2.8	32.2	7.1	15.8	15.7	18.5	20.4	32.6
Co	8.8	5.8	27.5	10.9	32.2	15.4	76.7	15.4	16.5	35.8	28.6	2.8	21.9
Mn	732.1	168.6	268.4	103.1	613.0	77.3	156.8	660.0	95.4	49.4	75.8	142.3	322.0
Cr	66.5	68.7	128.9	194.4	424.6	390.8	476.0	289.2	198.4	360.1	291.1	416.5	169.7
V	97.6	96.4	87.3	82.7	88.3	114.5	115.8	139.2	118.4	180.2	87.8	102.5	189.1
CIA	66.7	65.9	65.5	65.2	71.4	78.0	73.1	75.7	77.3	80.2	78.8	96.2	78.3
CIW	93.4	91.7	93.2	95.0	96.9	98.7	97.9	98.0	99.1	99.0	100.4	100.8	100.0
Al/Ti	30.1	30.2	33.8	34.5	29.2	33.7	32.3	23.7	30.5	32.1	39.5	37.6	37.6
∑Fe/Ti	4.3	8.6	7.3	12.4	5.7	12.3	16.6	8.5	10.6	18.7	27.4	54.2	41.9
∑Fe/Al	0.1	0.3	0.2	0.4	0.2	0.4	0.5	0.4	0.3	0.6	0.7	1.4	1.1

CORE PO1/48

Sample	PO15	PO19	PO13	PO12	PO11	PO10	PO9	PO7	PO6	PO5	PO1
Depth (m)	215.00	235.00	241.75	275.50	288.50	296.50	302.30	324.35	330.00	332.80	347.70
SiO_2	63.266	59.386	67.830	63.733	66.136	61.091	55.675	62.617	60.941	45.949	42.058
TiO_2	0.745	0.755	0.904	0.848	0.536	1.068	0.981	0.882	0.598	0.523	1.617
Al_2O_3	16.245	17.527	15.505	16.439	14.327	18.393	18.574	18.901	17.039	12.509	34.427
Fe_2O_3	4.990	8.505	4.119	7.987	5.517	7.480	13.182	7.355	14.123	34.805	14.694
MnO	0.035	0.017	0.021	0.010	0.027	0.063	0.069	0.009	0.020	0.044	0.010
MgO	1.689	1.977	1.336	1.057	1.897	1.418	1.218	0.410	0.171	0.112	0.126
CaO	0.615	0.458	0.094	0.159	0.328	0.099	0.106	0.078	0.050	0.049	0.061
Na_2O	0.654	0.455	0.296	0.084	0.089	0.089	0.093	0.096	0.037	0.048	0.077
K_2O	6.519	5.816	5.281	4.476	3.763	4.800	4.700	5.098	2.485	1.455	0.066
P_2O_5	0.419	0.298	0.049	0.098	0.225	0.059	0.064	0.047	0.123	0.080	0.125
LOI	3.540	3.620	3.660	3.380	5.220	4.200	4.490	2.960	3.060	2.200	6.390
H_2O^-	0.760	0.850	0.720	1.060	1.270	1.040	0.640	0.960	0.700	0.290	0.770
Total	99.477	99.664	99.815	99.331	99.335	99.800	99.792	99.413	99.347	98.064	100.421
Nb	15.1	15.2	16.8	27.7	10.9	28.5	25.5	18.5	11.2	10.5	28.8
Zr	155.0	158.4	258.0	259.4	116.8	235.0	198.3	198.9	152.7	145.6	292.2
Y	38.3	33.7	30.7	34.6	27.4	24.1	22.4	22.9	20.3	19.4	30.8
Sr	39.0	28.2	35.3	33.1	30.8	42.1	47.1	127.0	331.2	273.6	496.9
U	1.9	1.6	1.9	0.6	4.0	1.5	1.5	2.6	0.6	1.1	0.4
Rb	217.6	178.1	151.8	164.5	158.7	198.5	198.2	193.3	77.7	49.5	0.8
Th	14.4	12.2	13.7	23.6	13.1	20.0	17.5	17.9	20.5	15.0	32.2
Pb	8.1	1.5	8.4	6.0	9.5	5.0	4.3	9.0	11.1	14.5	12.7
Co	9.8	9.4	31.0	17.6	23.0	23.3	72.5	23.8	8.3	1.1	0.0
Mn	276.9	96.3	159.3	70.8	204.2	480.3	521.8	48.9	118.8	296.9	25.9
Cr	158.6	203.2	482.8	402.4	203.6	223.3	205.4	357.8	247.0	206.6	222.6
V	87.5	80.2	98.8	84.9	127.9	116.1	116.6	152.4	97.3	141.0	99.8
CIA	66.3	71.0	71.2	76.5	77.0	77.4	77.9	76.8	87.0	89.0	100.0
CIW	93.2	95.3	96.6	98.8	98.6	99.0	99.0	99.0	100.8	100.2	100.2
Al/Ti	34.2	36.4	26.9	30.4	41.9	27.0	29.7	33.6	44.6	37.5	33.4
∑Fe/Ti	6.4	10.7	4.3	8.9	9.6	6.6	12.7	8.0	22.6	63.6	8.5
∑Fe/Al	0.2	0.3	0.2	0.3	0.2	0.2	0.4	0.2	0.5	1.7	0.3

CORE ALK3/22

Sample	AL17	AL16	AL15	AL14	AL13	AL12	AL10	AL8	AL7	AL6	AL5	AL3
Depth (m)	223.82	256.06	267.00	272.69	283.67	292.26	323.77	344.43	353.64	360.73	367.35	370.94
SiO_2	61.638	66.572	62.671	57.891	58.204	66.311	81.760	54.064	53.190	51.488	34.062	43.469
TiO_2	0.634	0.573	1.042	0.972	1.135	1.298	0.892	4.029	0.634	2.090	1.343	1.854
Al_2O_3	15.210	11.226	17.269	18.304	19.757	17.044	5.025	13.705	14.740	35.886	27.920	34.903
Fe_2O_3	13.150	4.425	9.329	11.103	10.664	4.941	8.456	18.401	24.692	0.774	23.861	5.730
MnO	0.118	0.223	0.083	0.202	0.015	0.032	0.026	0.031	0.039	0.011	0.012	0.007
MgO	1.891	1.742	1.391	1.880	0.698	1.262	0.372	0.945	0.432	0.234	0.273	0.203
CaO	0.332	4.220	0.133	0.301	0.178	0.229	0.139	0.677	0.081	0.056	0.124	0.104
Na_2O	0.086	0.048	0.126	0.118	0.151	0.105	0.016	0.043	0.194	0.073	0.304	0.577
K_2O	2.966	3.287	4.078	4.275	5.344	4.954	1.622	4.354	3.594	1.162	6.508	7.357
P_2O_5	0.207	0.553	0.053	0.058	0.086	0.093	0.095	0.552	0.069	0.095	0.202	0.096
LOI	3.560	6.690	3.500	4.170	3.230	3.360	0.840	2.470	2.270	8.120	4.530	5.040
H_2O^-	0.350	0.200	0.630	0.780	0.720	0.820	0.300	0.760	0.510	0.600	0.910	0.930
Total	100.142	99.759	100.305	100.054	100.182	100.449	99.543	100.031	100.445	100.589	100.049	100.270
Nb	13.5	15.8	27.1	25.3	26.0	34.9	30.5	163.5	12.2	31.5	22.8	32.4
Zr	156.2	134.8	239.2	197.6	254.8	336.4	292.6	782.4	196.1	557.7	350.3	410.2
Y	20.8	34.2	23.6	23.1	25.5	27.5	10.5	43.5	27.2	56.0	44.1	55.9
Sr	41.3	39.3	52.9	114.2	106.8	51.4	21.2	258.8	370.4	209.4	958.3	452.5
U	0.6	1.4	1.7	1.9	3.4	2.7	1.6	2.6	2.2	7.8	1.6	7.0
Rb	110.9	106.1	178.0	188.1	219.5	196.7	60.7	162.3	129.5	32.7	155.5	170.4
Th	15.0	11.1	18.3	19.5	23.3	19.2	7.1	14.4	15.8	35.2	28.6	37.7
Pb	6.5	28.6	3.1	2.7	9.2	8.8	3.4	5.8	11.9	7.0	20.8	17.9
Co	23.2	15.6	22.6	36.8	12.0	41.3	9.9	52.4	14.9	15.0	4.0	0.0
Mn	938.6	1777.9	654.8	1629.8	90.0	232.2	180.8	161.1	270.4	68.6	36.9	32.2
Cr	245.4	295.5	189.9	196.0	221.2	266.7	255.8	406.8	156.7	575.8	550.6	732.5
V	117.2	122.3	98.6	108.4	129.9	156.1	72.5	186.5	115.5	233.4	317.2	311.5
CIA	81.5	52.9	78.5	77.8	76.3	74.8	73.5	74.5	77.9	96.6	79.3	79.7
CIW	98.4	63.6	98.2	96.8	98.2	97.9	99.0	100.1	98.0	100.0	99.1	97.5
Al/Ti	37.6	30.7	26.0	29.5	27.3	20.6	8.8	5.3	36.4	26.9	32.6	29.5
∑Fe/Ti	20.0	7.2	8.6	10.9	9.0	3.7	9.3	4.4	38.0	0.3	16.8	2.9
∑Fe/Al	0.5	0.2	0.3	0.4	0.3	0.2	1.1	0.8	1.0	0.0	0.5	0.1

CORE WK4/25											
Sample	WK16	WK13	WK12	WK11	WK10	WK9	WK6	WK5	WK3	WK2	WK1
Depth (m)	41.07	59.00	61.50	68.14	76.35	79.11	92.83	97.10	106.50	108.66	112.88
SiO_2	68.678	60.943	57.185	60.369	68.051	67.931	60.702	76.909	58.148	56.074	36.837
TiO_2	0.622	1.113	1.043	1.019	1.068	1.419	2.445	1.503	3.119	3.837	4.189
Al_2O_3	12.253	20.570	19.492	18.900	14.154	16.962	14.746	7.305	12.180	14.238	16.054
Fe_2O_3	3.626	5.455	11.122	9.077	7.841	2.607	11.494	8.939	15.805	13.262	24.377
MnO	0.041	0.020	0.056	0.019	0.066	0.014	0.018	0.052	0.027	0.042	0.252
MgO	1.308	1.205	1.153	0.770	0.668	0.719	1.008	0.497	1.032	1.397	1.561
CaO	1.785	0.158	0.116	0.085	0.091	0.107	0.532	0.347	0.491	0.811	2.558
Na_2O	0.054	0.128	0.104	0.131	0.113	0.125	0.061	0.028	0.058	0.056	1.333
K_2O	3.593	5.415	4.988	5.061	3.802	4.634	4.388	2.210	3.766	4.610	4.453
P_2O_5	1.035	0.065	0.078	0.076	0.049	0.083	0.361	0.153	0.341	0.524	0.784
LOI	5.680	4.020	3.780	3.300	2.870	3.080	2.830	1.410	2.400	3.060	4.050
H_2O^-	0.860	1.070	0.840	0.640	0.870	1.150	1.420	0.540	1.270	1.290	1.830
Total	99.535	100.162	99.957	99.447	99.643	98.831	100.005	99.893	98.637	99.201	98.278
Nb	18.0	29.3	25.7	23.7	19.5	40.1	90.5	53.3	115.8	155.2	176.7
Zr	138.4	224.8	217.6	221.8	463.9	397.0	494.2	330.4	565.0	764.8	925.5
Y	42.0	24.8	24.5	23.7	25.3	29.5	36.1	17.2	33.6	41.7	59.4
Sr	60.5	96.0	156.0	315.0	176.0	402.8	189.3	84.9	174.7	185.5	285.0
U	1.5	2.3	0.9	3.2	2.5	2.8	2.3	1.3	2.6	4.8	2.0
Rb	132.0	238.9	221.4	212.9	158.4	190.5	188.3	83.3	155.1	195.7	193.4
Th	13.9	22.7	20.9	19.7	17.8	19.7	16.8	9.2	15.7	17.1	20.1
Pb	23.6	7.0	11.8	13.9	8.2	9.0	16.7	8.3	15.6	12.3	25.2
Co	10.8	12.8	13.1	16.0	14.0	38.7	48.2	20.6	46.8	41.2	70.9
Mn	350.9	175.1	420.3	115.2	531.5	88.3	113.4	431.7	204.4	309.3	2198.7
Cr	260.2	206.6	189.0	178.8	317.9	291.8	390.4	284.2	414.9	385.7	626.9
V	138.7	129.2	118.1	104.4	136.0	157.2	171.0	99.2	182.7	199.6	93.3
CIA	72.1	76.8	77.7	76.9	76.5	76.5	74.9	73.0	74.1	72.9	62.1
CIW	93.5	98.4	99.0	99.0	98.4	98.8	98.6	95.9	98.6	97.9	76.4
Al/Ti	30.9	29.0	29.3	29.1	20.8	18.7	9.4	7.6	6.1	5.8	6.0
∑Fe/Ti	5.4	4.7	10.2	8.5	7.0	1.7	4.5	5.8	4.8	3.3	5.4
∑Fe/Al	0.2	0.2	0.3	0.3	0.3	0.1	0.5	0.8	0.8	0.6	0.9

CORE QK4/89

Sample	QK15	QK14	QK13	QK12	QK11	QK9	QK7	QK6	QK5	QK4	QK3	QK2
Depth (m)	35.97	41.36	47.39	50.09	52.78	70.72	83.32	85.67	87.27	91.21	96.70	99.40
SiO_2	65.359	59.003	62.834	61.808	65.836	63.734	92.364	70.753	55.266	59.607	50.712	46.144
TiO_2	1.012	0.963	1.322	1.045	1.425	2.479	0.179	2.130	3.616	2.637	4.273	0.490
Al_2O_3	15.481	18.948	20.842	15.428	18.100	11.986	2.268	9.733	14.022	13.990	13.592	11.173
Fe_2O_3	8.654	10.235	3.091	8.576	3.847	13.066	3.654	10.645	16.762	12.977	20.432	36.018
MnO	0.058	0.021	0.068	0.842	0.012	0.023	0.024	0.027	0.035	0.042	0.043	0.085
MgO	0.787	0.931	0.845	1.358	0.801	0.899	0.136	0.722	1.294	1.349	1.204	0.274
CaO	0.113	0.115	0.133	0.164	0.146	0.465	0.072	0.329	0.523	0.441	0.734	0.089
Na_2O	0.091	0.108	0.150	0.117	0.112	0.040	0.004	0.034	0.045	0.042	0.029	0.040
K_2O	3.893	4.588	4.693	3.812	4.709	3.615	0.681	2.917	4.175	4.287	4.065	2.053
P_2O_5	0.058	0.073	0.071	0.061	0.077	0.334	0.039	0.213	0.367	0.289	0.552	0.087
LOI	3.190	3.800	4.490	6.770	3.480	2.520	0.200	1.720	2.710	2.710	2.550	2.450
H_2O^-	1.030	0.790	1.310	0.850	1.180	1.220	0.260	1.130	1.700	1.580	1.540	0.880
Total	99.726	99.575	99.849	100.831	99.725	100.381	99.881	100.353	100.515	99.951	99.726	99.783
Nb	23.4	21.3	27.4	19.9	41.5	92.6	6.1	73.6	137.0	98.0	168.8	9.2
Zr	249.5	228.5	298.7	313.1	401.3	531.9	72.7	423.5	644.0	523.8	822.9	191.8
Y	23.3	23.2	28.6	25.1	28.8	32.6	3.0	22.4	37.1	30.1	41.5	19.3
Sr	202.5	290.6	217.1	169.4	176.8	197.5	17.2	118.8	213.2	137.7	287.3	291.1
U	2.1	0.9	6.0	3.6	3.7	2.0	0.1	1.7	2.8	1.2	3.9	2.0
Rb	166.0	209.2	223.8	163.5	212.6	154.3	19.7	111.0	182.9	177.9	157.9	71.9
Th	17.0	20.1	26.4	17.4	19.9	15.6	1.3	10.0	18.1	14.0	20.1	15.4
Pb	12.2	16.3	15.1	11.0	10.2	16.6	0.2	9.9	17.7	12.4	17.2	15.7
Co	13.4	37.6	31.3	24.5	33.7	32.3	6.0	26.9	32.4	60.3	55.1	16.9
Mn	400.8	142.4	497.8	6905.0	74.2	127.0	158.1	153.6	194.8	359.2	307.6	602.4
Cr	160.4	184.0	258.1	227.2	303.2	414.8	67.8	361.4	527.6	357.9	425.2	257.0
V	88.2	108.8	123.2	122.5	171.1	150.5	24.5	125.8	202.8	164.3	217.6	96.5
CIA	77.8	78.5	79.4	77.5	77.1	74.9	74.4	74.7	75.0	74.4	75.3	83.3
CIW	98.6	98.9	98.5	97.8	98.6	99.1	98.1	98.5	99.0	98.7	99.6	99.8
Al/Ti	24.0	30.8	24.7	23.1	19.9	7.6	19.8	7.2	6.1	8.3	5.0	35.7
∑Fe/Ti	8.2	10.1	2.2	7.7	2.6	5.1	20.3	4.9	4.5	4.7	4.6	70.9
∑Fe/Al	0.3	0.3	0.1	0.3	0.1	0.7	1.0	0.7	0.7	0.6	0.9	2.0

CORE HR4/98

Sample	HR16	HR15	HR14	HR13	HR12	HR10	HR9	HR8	HR7	HR6	HR4	HR3	HR2	HR1
Depth (m)	49.10	53.60	56.60	83.30	106.80	146.80	153.20	154.60	158.70	176.10	185.60	189.26	194.70	197.20
SiO_2	50.402	50.473	39.127	73.342	56.373	55.129	76.436	45.638	64.606	76.210	25.882	40.173	43.238	66.327
TiO_2	0.986	0.938	0.787	1.025	0.984	0.801	1.153	0.750	1.101	1.181	0.611	1.338	1.346	0.406
Al_2O_3	16.514	18.711	15.382	14.561	16.299	11.210	15.397	8.931	14.787	11.111	23.311	34.085	35.529	9.007
Fe_2O_3	23.069	20.249	24.210	1.754	12.200	18.426	0.770	38.682	12.433	5.162	39.909	10.294	4.752	19.365
MnO	0.010	0.015	0.204	0.013	0.045	0.132	0.006	0.023	0.007	0.005	0.043	0.009	0.002	0.023
MgO	0.185	0.189	0.404	0.175	0.256	0.272	0.110	0.089	0.096	0.104	0.117	0.138	0.176	0.062
CaO	0.084	0.046	0.054	0.015	0.052	0.044	0.016	0.056	0.009	0.018	0.067	0.016	0.042	0.026
Na_2O	0.044	0.048	0.053	0.058	0.065	0.040	0.034	0.021	0.035	0.039	0.000	0.005	0.042	0.038
K_2O	1.122	1.237	1.021	1.012	1.308	0.822	0.412	0.429	0.625	0.933	0.116	0.606	5.287	2.546
P_2O_5	0.030	0.043	0.046	0.024	0.027	0.021	0.025	0.040	0.034	0.030	0.100	0.044	0.051	0.025
LOI	5.180	7.020	16.460	5.220	10.660	11.790	3.810	2.470	3.840	2.930	7.700	11.420	8.070	1.000
H_2O^-	0.880	1.020	0.730	0.780	0.800	0.500	0.520	0.450	0.590	0.360	0.820	1.060	0.750	0.370
Total	98.506	99.989	98.478	97.979	99.069	99.187	98.689	97.579	98.163	98.083	98.676	99.188	99.285	99.195
Nb	18.6	17.7	14.7	18.1	17.3	13.3	17.6	13.0	17.9	17.8	12.1	26.5	27.7	8.1
Zr	263.1	229.6	200.6	421.2	310.8	369.0	502.9	319.1	436.0	539.5	152.8	302.1	308.7	97.3
Y	36.7	27.3	29.5	30.2	29.2	30.6	34.7	27.0	29.5	32.7	18.7	36.8	46.4	20.4
Sr	59.3	69.9	78.3	46.5	49.3	25.6	42.3	59.3	73.2	61.9	322.1	84.5	131.9	45.5
U	5.3	4.9	3.9	3.6	4.4	2.8	5.9	8.8	2.0	2.8	1.9	3.6	2.5	1.1
Rb	53.2	57.1	47.8	46.5	57.1	32.6	13.8	15.7	20.8	26.7	2.7	16.1	124.4	68.7
Th	22.9	20.2	16.0	17.4	17.8	13.4	16.9	12.0	15.7	17.8	13.5	32.1	30.0	9.3
Pb	9.3	14.0	9.7	8.2	5.9	4.9	6.6	13.4	8.0	8.3	13.8	17.3	20.8	9.3
Co	0.1	0.0	3.9	4.2	0.4	22.9	32.1	0.0	0.0	2.4	1.5	2.1	3.8	0.0
Mn	21.0	32.1	1702.9	75.1	345.0	1095.4	46.1	47.4	34.5	40.6	275.4	35.3	14.0	133.7
Cr	405.4	366.4	362.1	361.7	371.8	471.5	588.4	1000.6	376.4	236.6	263.8	447.8	392.6	314.2
V	180.6	226.1	205.4	122.4	180.2	145.7	148.0	190.4	113.8	163.3	175.0	151.5	136.2	95.0
CIA	92.4	93.0	92.9	92.6	91.3	91.9	97.0	94.6	95.7	91.5	100.0	98.3	86.1	76.2
CIW	99.1	99.7	99.5	99.6	99.2	99.2	99.8	99.5	100.1	99.8	100.5	100.2	99.9	99.4
Al/Ti	26.2	31.2	30.6	22.3	25.9	21.9	20.9	18.7	21.0	14.7	59.8	39.9	41.4	34.8
∑Fe/Ti	21.6	19.9	25.0	1.6	10.9	20.0	0.6	48.8	10.6	4.1	58.9	6.7	3.2	46.7
∑Fe/Al	0.8	0.6	0.8	0.1	0.4	0.9	0.0	2.6	0.5	0.3	1.0	0.2	0.1	1.3

CORE GA1522E

Sample	GAA14	GAA13	GAA11	GAA9	GAA8	GAA7	GAA6	GAA5	GAA4	GAA3	GAA2	GAA1
Depth (m)	148.65	180.10	186.00	192.15	203.15	207.15	209.30	211.15	213.15	215.00	215.15	227.90
SiO_2	54.62	59.48	51.59	31.40	38.39	26.75	55.19	67.57	66.15	36.01	13.32	30.02
TiO_2	2.12	3.25	3.80	0.34	0.37	0.38	0.74	1.10	2.04	0.67	0.84	1.36
Al_2O_3	14.30	14.73	14.63	8.28	5.58	8.56	19.88	17.86	24.83	14.38	14.06	25.38
Fe_2O_3	17.12	13.26	20.54	55.61	54.05	44.20	13.70	5.04	1.82	35.12	65.50	33.84
MnO	0.02	0.05	0.04	0.04	0.04	0.83	0.13	0.01	0.01	0.26	0.07	0.02
MgO	0.96	0.83	0.80	0.20	0.00	1.38	0.28	0.00	0.00	0.16	0.13	0.00
CaO	1.61	0.56	0.70	0.10	0.06	0.26	0.22	0.01	0.01	0.14	0.05	0.05
Na_2O	0.02	0.04	0.04	0.04	0.03	0.02	0.02	0.03	0.03	0.03	0.02	0.00
K_2O	5.12	4.63	4.59	2.37	1.52	1.63	0.03	0.01	0.01	0.01	0.05	0.07
P_2O_5	0.60	0.37	0.50	0.08	0.08	0.05	0.05	0.04	0.05	1.13	0.11	0.08
LOI	3.46	2.79	2.93	1.53	0.88	16.61	10.46	8.59	5.29	11.58	6.54	9.43
Total	99.94	99.98	100.15	99.99	100.99	100.66	100.69	100.25	100.24	99.48	100.68	100.24
Nb	107	88	110	9	8	9	14	17	27	11	15	8
Zr	696	575	697	113	121	98	177	397	562	159	219	131
Y	51	36	44	9	13	17	37	47	42	11	13	9
Sr	119	174	223	95	126	75	82	51	94	117	154	46
U	4	1	3	0	0	0	3	5	7	5	0	0
Rb	183	193	182	91	42	58	4	4	0	4	8	6
Th	22	16	17	17	13	13	23	20	31	17	29	13
Pb	24	17	18	24	14	12	24	62	15	13	25	17
Co	51	27	38	26	19	30	13	20	135	48	19	9
Cr	172	479	305	96	80	118	258	469	792	414	363	1,755
V	131	179	208	88	62	79	123	145	216	196	176	210
Ni	132	113	143	12	0	38	46	61	47	0	54	84
Cu	41	13	31	37	43	5	272	16	6	24	42	14
Zn	25	24	23	13	14	20	6	4	3	24	41	14
Ga	21	24	26	8	8	14	27	21	23	21	22	19
Ba	1,549	185	183	102	32	73	39	16	11	38	51	57
La	112	96	127	12	10	33	47	46	48	16	19	3
Ce	246	265	271	44	15	27	123	75	82	28	26	0
Nd	97	97	104	12	14	26	45	33	30	23	14	0
S	1,382	797	949	49	170	29	2,449	24,893	2,356	1,774	303	105
Cl	21	42	18	37	86	57	15	34	22	331	114	22
CIA	66.9	73.9	74.1	76.0	77.6	79.9	98.3	100.1	100.2	119.9	100.6	100.1
CIW	90.4	98.7	99.0	99.3	100.6	95.7	98.4	100.2	100.2	120.1	101.0	100.4
Al/Ti	10.6	7.1	6.0	38.2	23.6	35.3	42.1	25.4	19.1	33.6	26.2	29.2
∑Fe/Ti	7.8	4.0	5.3	161.1	146.3	97.8	16.7	4.2	0.8	46.1	73.4	22.6
∑Fe/Al	0.738	0.559	0.872	4.222	6.192	2.771	0.397	0.165	0.044	1.371	2.801	0.773

CORE SA2072E

Sample	SAA6	SAA5	SAA4	SAA3	SAA2	SAA1
Depth (m)	132.30	136.90	152.20	155.60	175.00	181.20
SiO_2	62.29	54.99	90.29	75.13	24.05	8.80
TiO_2	1.31	1.95	0.16	1.43	1.11	0.41
Al_2O_3	15.72	13.82	1.64	6.96	20.84	7.14
Fe_2O_3	11.51	19.44	8.22	12.16	46.00	81.71
MnO	0.01	0.30	0.03	0.01	0.03	0.02
MgO	0.80	0.89	0.02	0.32	0.19	0.00
CaO	0.39	0.95	0.11	0.27	0.03	0.03
Na_2O	0.05	0.01	0.01	0.04	0.29	0.10
K_2O	5.06	4.69	0.49	2.08	2.95	1.29
P_2O_5	0.27	0.56	0.08	0.18	0.09	0.09
LOI	2.69	2.64	0.18	1.19	4.59	1.56
Total	100.11	100.24	101.22	99.76	100.15	101.15
Nb	48	87	9	41	20	10
Zr	361	548	109	351	222	109
Y	25	41	5	20	20	12
Sr	40	93	22	80	167	140
U	1	0	1	0	0	0
Rb	179	167	18	74	72	37
Th	20	21	5	13	28	25
Pb	9	22	8	8	42	46
Co	21	30	0	8	25	9
Cr	179	148	72	303	331	129
V	117	154	22	106	164	144
Ni	80	120	13	42	206	0
Cu	17	5	0	0	3	0
Zn	12	15	4	29	30	14
Ga	23	22	5	14	26	14
Ba	611	854	47	94	90	83
La	55	123	16	41	34	0
Ce	110	290	27	96	58	0
Nd	36	117	11	35	16	3
S	418	807	0	390	235	124
Cl	40	25	86	51	27	26
CIA	73.7	71.6	74.7	74.5	85.6	83.6
CIW	99.1	97.2	98.5	98.2	98.5	100.0
Al/Ti	18.8	11.1	16.1	7.6	29.4	27.3
∑Fe/Ti	8.6	9.7	51.9	8.4	39.6	198.5
∑Fe/Al	0.455	0.877	3.234	1.100	1.347	7.277

CORE SA2093E

Sample	SAB8	SAB7	SAB6	SAB5	SAB4	SAB3	SAB2	SAB1
Depth (m)	198.00	199.70	213.70	219.60	226.80	232.80	237.70	242.45
SiO_2	65.01	71.04	66.97	65.15	67.24	64.86	50.77	43.85
TiO_2	2.66	1.95	1.38	1.45	1.39	1.41	1.32	1.47
Al_2O_3	11.47	11.77	22.54	23.90	21.99	22.79	19.51	38.02
Fe_2O_3	14.51	8.21	1.82	1.78	0.58	0.72	22.30	1.85
MnO	0.01	0.01	0.00	0.01	0.00	0.01	0.04	0.00
MgO	0.48	0.41	0.05	0.00	0.11	0.03	0.56	0.01
CaO	0.42	0.34	0.03	0.02	0.04	0.03	0.14	0.04
Na_2O	0.10	0.14	0.09	0.10	0.09	0.11	0.11	0.17
K_2O	3.27	3.20	0.97	1.07	1.36	1.48	0.83	1.06
P_2O_5	0.30	0.25	0.04	0.04	0.04	0.04	0.16	0.19
LOI	2.33	2.24	6.43	6.67	7.07	8.70	4.74	12.22
Total	100.56	99.56	100.31	100.20	99.91	100.16	100.50	98.89
Nb	79	58	20	22	22	22	20	24
Zr	586	385	386	366	399	429	372	478
Y	32	27	27	22	27	34	20	25
Sr	169	176	72	79	69	83	105	388
U	bdl	4	3	6	9	10	0	5
Rb	133	121	35	39	53	60	29	31
Th	17	11	26	27	27	29	29	26
Pb	13	11	20	19	17	14	12	92
Co	13	46	8	8	17	12	5	20
Cr	391	313	192	446	442	611	441	255
V	289	205	158	279	251	279	311	132
Ni	74	111	0	23	2	62	218	42
Cu	0	1	0	0	104	21	3	0
Zn	13	12	5	8	3	8	71	6
Ga	20	16	30	34	32	33	35	22
Ba	196	1,333	126	147	196	219	117	176
La	83	72	46	56	46	53	39	108
Ce	173	139	77	83	108	113	56	319
Nd	64	54	31	37	44	38	25	56
S	78	375	33	31	250	681	116	162
Cl	107	91	64	58	88	111	147	84
CIA	75.4	76.0	95.1	95.0	93.2	92.9	95.4	97.3
CIW	98.2	97.9	99.5	99.6	99.4	99.4	99.7	100.3
Al/Ti	6.8	9.5	25.6	25.8	24.8	25.3	23.2	40.5
∑Fe/Ti	5.4	4.1	1.2	1.1	0.4	0.5	16.2	1.1
∑Fe/Al	0.793	0.433	0.048	0.044	0.016	0.018	0.699	0.027

CORE 2491E

Sample	SAC8	SAC7	SAC6	SAC5b-w	SAC5a-r	SAC4	SAC3	SAC2	SAC1
Depth (m)	200.90	206.00	212.30	217.50	217.50	232.70	235.30	236.30	242.60
SiO_2	63.86	57.59	64.79	68.74	61.69	51.83	50.63	38.91	25.71
TiO_2	1.17	1.64	1.27	2.08	1.82	4.33	4.03	0.12	0.17
Al_2O_3	16.49	14.61	14.53	14.85	12.54	14.83	14.80	3.69	2.91
Fe_2O_3	9.45	15.92	5.04	2.23	14.08	18.57	20.38	56.14	70.69
MnO	0.15	0.17	0.29	0.01	0.02	0.02	0.02	0.02	0.02
MgO	0.69	1.38	1.85	1.11	0.99	1.22	1.07	0.09	0.01
CaO	0.18	0.22	0.96	0.95	0.80	0.61	0.73	0.12	0.15
Na_2O	0.06	0.04	0.07	0.05	0.05	0.06	0.09	0.03	0.02
K_2O	4.88	4.72	4.91	5.96	5.01	4.68	4.45	0.96	0.73
P_2O_5	0.06	0.12	0.23	0.58	0.42	0.42	0.54	0.08	0.12
LOI	3.28	3.84	4.68	3.25	2.91	3.37	3.15	0.83	0.69
Total	100.27	100.25	98.61	99.81	100.32	99.93	99.87	100.98	101.22
Nb	20	50	33	92	75	117	119	5	6
Zr	405	339	173	605	480	665	755	39	54
Y	32	25	24	43	31	37	48	7	11
Sr	61	102	184	142	118	222	253	28	47
U	2	2	2	6	1	2	2	0	0
Rb	169	193	195	172	164	200	179	33	21
Th	22	15	7	19	14	17	21	10	10
Pb	16	18	9	11	19	21	19	11	7
Co	30	38	151	20	16	48	34	14	13
Cr	222	161	147	157	152	495	336	52	53
V	165	195	162	129	170	222	204	52	53
Ni	52	77	181	65	65	181	160	0	0
Cu	0	14	108	64	29	21	20	40	18
Zn	17	35	46	24	33	50	33	8	15
Ga	22	24	21	21	20	28	29	5	9
Ba	789	399	6,371	620	1,063	231	224	86	34
La	48	65	55	113	78	121	122	0	7
Ce	92	133	57	263	179	293	306	1	49
Nd	30	47	40	97	61	111	115	7	7
S	146	106	1,842	922	883	875	1,027	0	0
Cl	90	78	35	29	26	33	21	41	48
CIA	74.8	73.4	68.7	68.4	67.8	73.8	74.8	76.8	78.3
CIW	98.3	98.8	91.7	97.2	95.9	98.7	98.8	98.0	99.4
Al/Ti	22.1	14.0	17.9	11.2	10.8	5.4	5.8	48.2	26.8
∑Fe/Ti	7.8	9.4	3.7	1.0	7.5	4.1	4.9	468.7	418.1
∑Fe/Al	0.355	0.671	0.208	0.093	0.698	0.772	0.851	9.730	15.593

APPENDIX B

Sample	La	Ce	Pr	Nd	Sm
GAA14	101.1	222.5	23.10	85.60	14.32
GAA11	113.1	254.8	28.51	110.6	19.18
GAA9	25.23	62.50	5.741	21.56	3.450
GAA4	36.82	69.77	7.717	28.15	5.200
GAA2	20.03	41.37	4.037	14.26	2.393
IO16	44.68	92.71	11.68	45.67	9.309
IO12	29.96	72.36	7.041	26.40	5.032
IO8	39.96	104.2	8.887	31.62	5.329
IO2	44.12	106.2	9.759	35.32	6.109
IO1	43.58	122.7	9.462	34.60	6.370
WK16	43.49	74.24	11.03	43.39	8.420
WK12	38.64	102.0	8.682	31.25	5.328
WK9	43.14	113.3	9.939	35.89	6.328
WK6	80.91	184.9	19.66	75.02	12.60
WK1	103.4	232.7	26.29	104.0	18.97
HR16	32.25	60.32	7.390	28.07	5.534
HR13	28.39	54.01	6.225	23.13	4.399
HR9	36.01	64.67	8.570	30.42	4.758
HR4	17.96	365.7	4.221	18.39	4.297
HR1	19.64	39.36	4.235	16.40	3.004

BULK ROCK REE DATA

Eu	Gd	Tb	Dy	Ho	Er	Tm	Yb	Lu
3.356	10.54	1.548	9.017	1.631	4.451	0.606	3.903	0.580
4.888	13.01	1.657	8.968	1.516	3.803	0.491	3.243	0.450
0.755	2.286	0.297	1.648	0.308	0.895	0.145	1.062	0.176
1.101	4.785	0.851	6.020	1.272	3.796	0.561	3.860	0.613
0.557	1.901	0.294	1.915	0.387	1.324	0.210	1.503	0.229
1.704	8.222	1.232	7.429	1.422	4.115	0.598	4.018	0.624
1.020	4.278	0.648	4.039	0.800	2.374	0.347	2.414	0.379
1.021	3.881	0.562	3.449	0.658	1.906	0.290	1.916	0.300
1.160	4.189	0.569	3.327	0.685	2.208	0.340	2.448	0.397
1.264	4.551	0.646	3.760	0.716	2.089	0.303	2.077	0.326
1.781	7.024	0.997	6.000	1.150	3.296	0.463	3.089	0.498
1.069	3.818	0.568	3.382	0.646	1.909	0.278	1.922	0.290
1.316	4.727	0.724	4.511	0.865	2.556	0.378	2.564	0.377
3.148	9.202	1.252	6.860	1.215	3.254	0.422	2.824	0.409
4.862	15.58	2.085	11.18	1.905	4.838	0.617	3.831	0.533
1.168	5.177	0.799	5.190	1.053	3.138	0.439	2.999	0.470
0.913	3.879	0.654	4.370	0.884	2.735	0.410	2.935	0.447
1.056	4.663	0.833	5.542	1.131	3.555	0.524	3.754	0.583
0.958	3.631	0.534	2.966	0.606	1.924	0.301	2.181	0.352
0.617	2.213	0.415	3.031	0.646	2.155	0.344	2.516	0.421

Sample	La	Ce	Pr	Nd	Sm	Eu
QK14	31.88	94.03	6.822	24.26	3.808	0.637
QK11	43.86	109.0	9.669	34.36	5.868	1.308
QK9	74.55	170.1	18.35	69.52	11.77	2.836
QK6	57.65	137.0	14.94	56.97	9.542	2.301
QK3	103.6	242.7	27.57	107.4	18.54	4.638
AL15	31.24	96.58	7.147	25.61	4.373	0.954
AL13	50.20	111.4	10.94	39.88	6.809	1.377
AL10	11.46	26.27	2.822	11.14	2.382	0.724
AL8	117.4	267.9	29.75	114.9	19.32	5.093
AL3	49.65	94.85	11.68	45.14	9.115	2.046
SAA6	58.02	121.7	12.47	45.08	6.380	1.443
SAA5	106.8	238.5	24.83	91.16	14.52	3.408
SAA3	38.06	87.78	9.494	36.49	6.596	1.730
SAA2	39.83	86.85	7.199	20.57	2.936	0.621
SAB8	73.87	171.9	18.61	71.67	11.92	2.897
SAB6	37.98	77.82	8.225	29.33	5.567	1.099
SAB4	33.33	74.26	7.990	28.93	5.718	1.120
SAB2	28.04	54.36	5.501	18.77	3.693	0.805

Gd	Tb	Dy	Ho	Er	Tm	Yb	Lu
3.167	0.485	2.932	0.589	1.692	0.262	1.795	0.261
4.627	0.723	4.347	0.846	2.510	0.381	2.506	0.395
8.256	1.145	6.381	1.105	2.946	0.389	2.648	0.383
6.450	0.853	4.695	0.802	2.191	0.303	2.087	0.304
12.73	1.595	8.349	1.384	3.430	0.447	2.861	0.388
3.245	0.479	2.786	0.531	1.567	0.230	1.595	0.246
5.206	0.764	4.417	0.870	2.537	0.366	2.526	0.393
2.629	0.393	2.218	0.387	1.063	0.150	1.045	0.156
13.39	1.710	8.940	1.493	3.718	0.492	3.014	0.424
8.973	1.348	8.230	1.595	4.725	0.672	4.416	0.687
4.691	0.726	4.449	0.878	2.546	0.374	2.583	0.395
10.23	1.414	7.852	1.434	3.964	0.543	3.523	0.531
5.137	0.679	3.717	0.638	1.710	0.233	1.603	0.230
2.387	0.444	3.080	0.650	2.172	0.351	2.660	0.434
8.368	1.153	6.373	1.127	2.976	0.408	2.725	0.387
4.293	0.709	4.636	0.916	2.813	0.428	3.020	0.466
4.377	0.712	4.646	0.922	2.779	0.425	3.077	0.461
3.377	0.514	3.322	0.666	2.030	0.311	2.170	0.333

Sample	La	Ce	Pr	Nd	Sm	Eu
SAC7	57.48	145.2	13.37	49.02	8.159	1.795
SAC5B	97.14	208.1	21.21	76.39	12.45	3.051
SAC5A	70.59	150.6	15.69	56.87	9.338	2.382
SAC3	112.1	251.3	27.83	106.9	18.22	4.753
SAC1	8.244	20.06	1.680	6.209	1.178	0.290
PO13	32.97	76.93	7.625	28.32	5.181	0.986
PO10	41.86	111.9	9.671	34.96	6.033	1.176
PO9	39.80	103.3	9.077	33.12	5.598	1.107
PO5	29.85	79.20	6.495	24.11	4.374	0.902
PO1	64.88	100.3	12.80	41.45	5.057	0.959

Gd	Tb	Dy	Ho	Er	Tm	Yb	Lu
5.963	0.840	4.774	0.886	2.476	0.347	2.313	0.346
9.400	1.332	7.684	1.408	3.813	0.535	3.468	0.509
7.093	1.020	5.735	1.059	2.905	0.405	2.589	0.400
13.19	1.757	9.470	1.609	4.065	0.520	3.284	0.441
1.162	0.172	1.068	0.236	0.728	0.114	0.799	0.129
4.339	0.697	4.362	0.874	2.611	0.386	2.698	0.418
4.253	0.618	3.734	0.705	2.039	0.308	2.097	0.322
3.879	0.556	3.353	0.646	1.865	0.271	1.906	0.286
3.396	0.507	3.135	0.618	1.885	0.286	1.952	0.307
3.446	0.518	3.726	0.854	2.880	0.445	3.281	0.536

APPENDIX C XRD SPECTRA

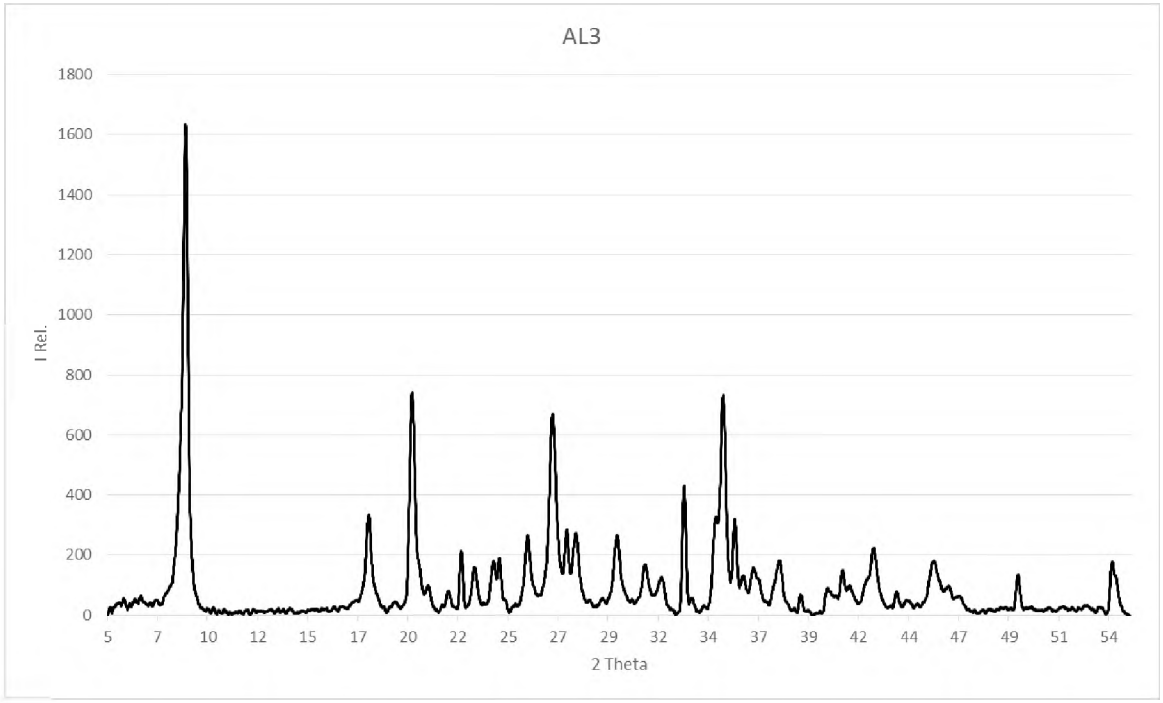

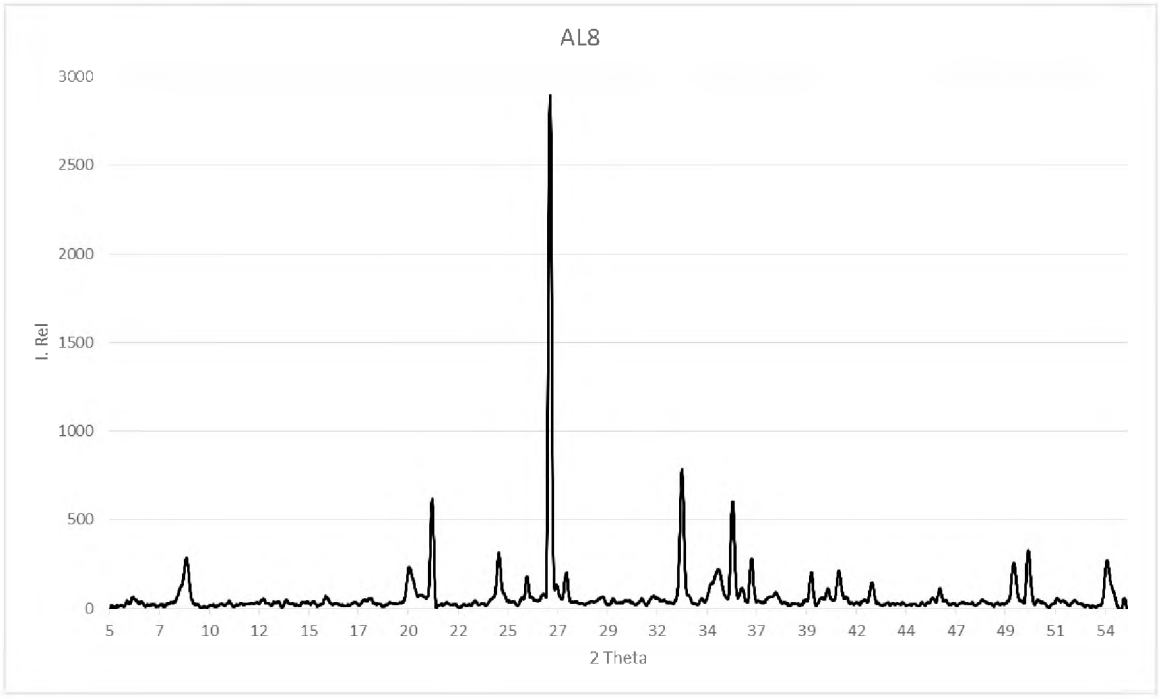

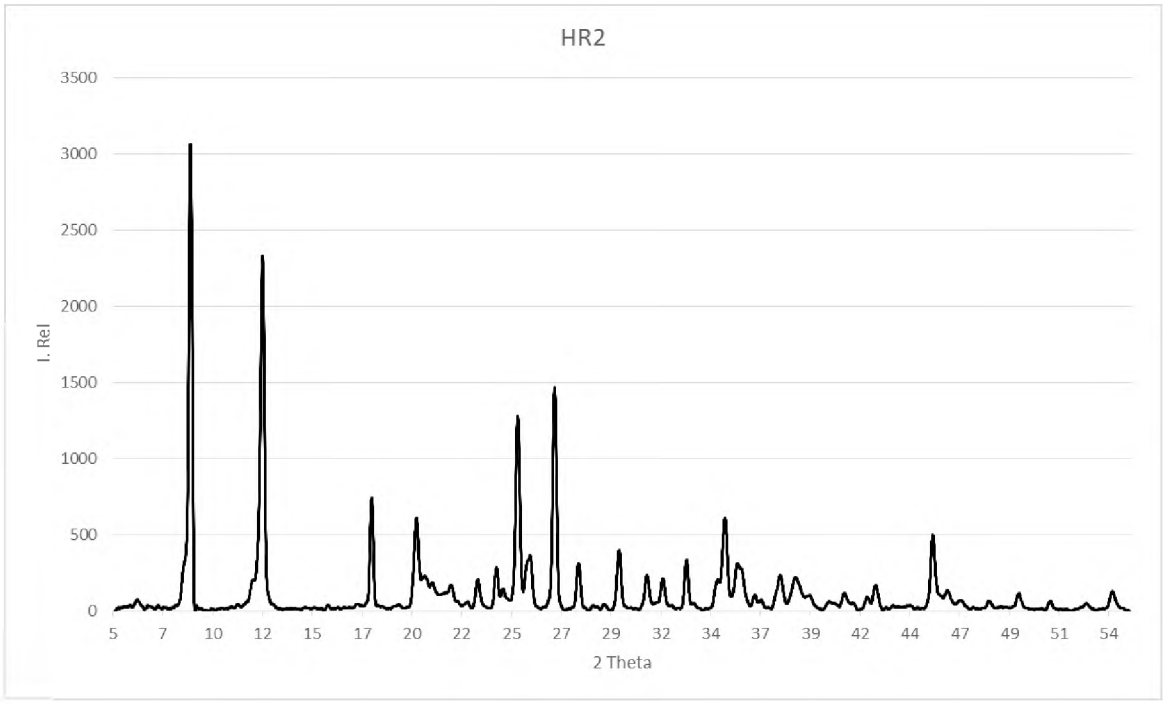
HR2
3500
3000
2500
2000
1500
1000
500
0
I. Rel
5 7 10 12 15 17 20 22 25 27 29 32 34 37 39 42 44 47 49 51 54
2 Theta

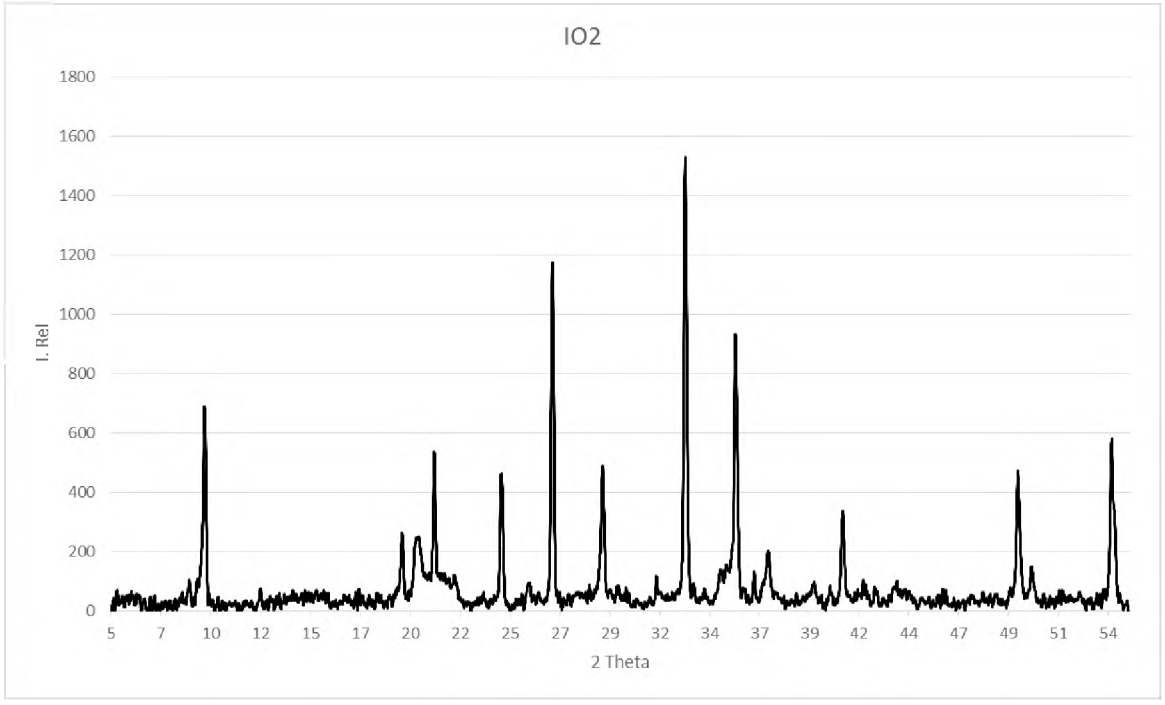
IO2
1800
1600
1400
1200
1000
800
600
400
200
0
I. Rel
5 7 10 12 15 17 20 22 25 27 29 32 34 37 39 42 44 47 49 51 54
2 Theta

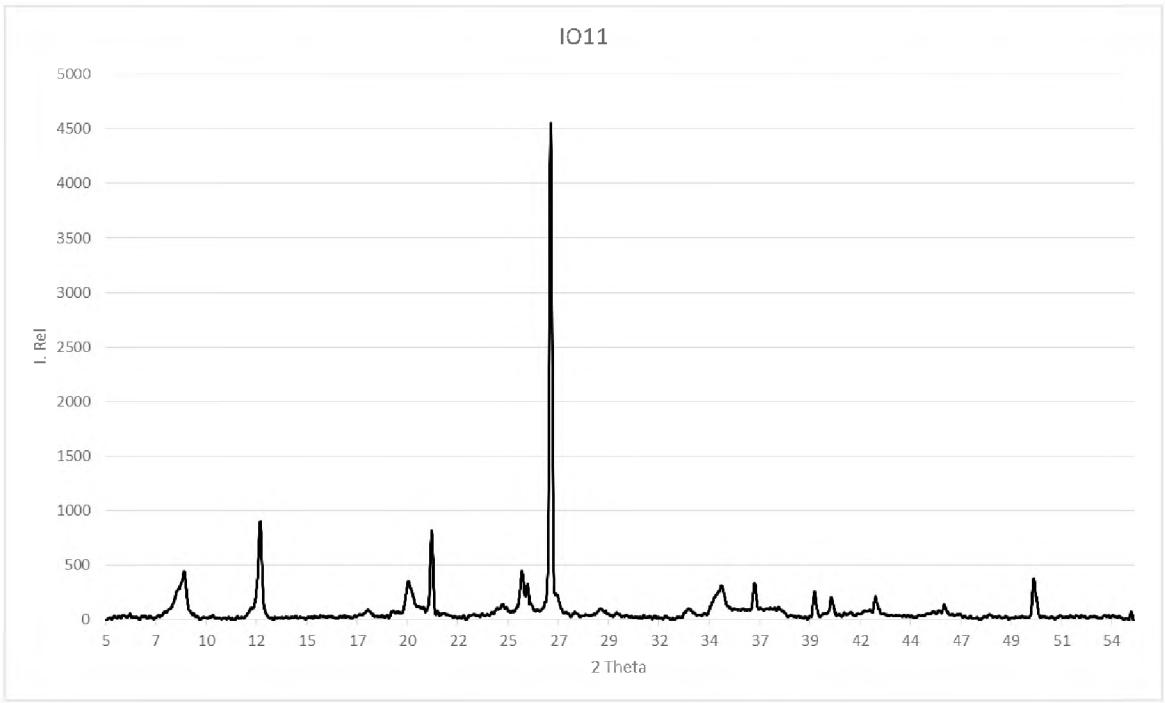
IO11
I. Rel
5000
4500
4000
3500
3000
2500
2000
1500
1000
500
0
5 7 10 12 15 17 20 22 25 27 29 32 34 37 39 42 44 47 49 51 54
2 Theta

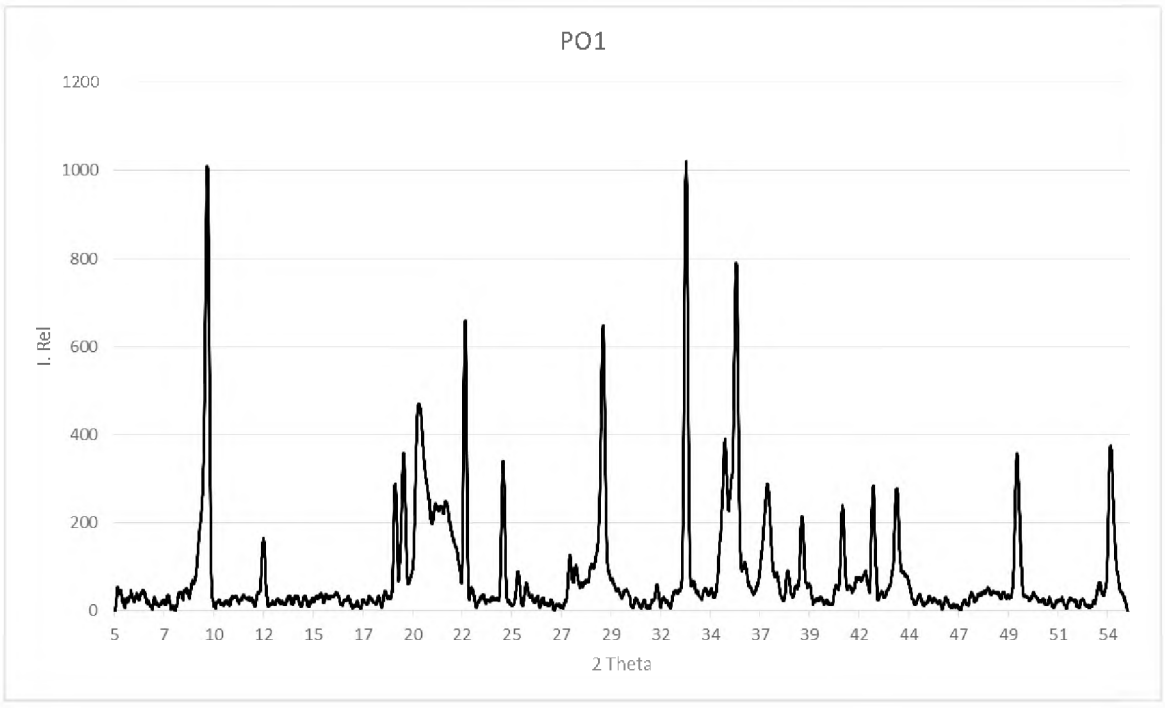
PO1
I. Rel
1200
1000
800
600
400
200
0
5 7 10 12 15 17 20 22 25 27 29 32 34 37 39 42 44 47 49 51 54
2 Theta

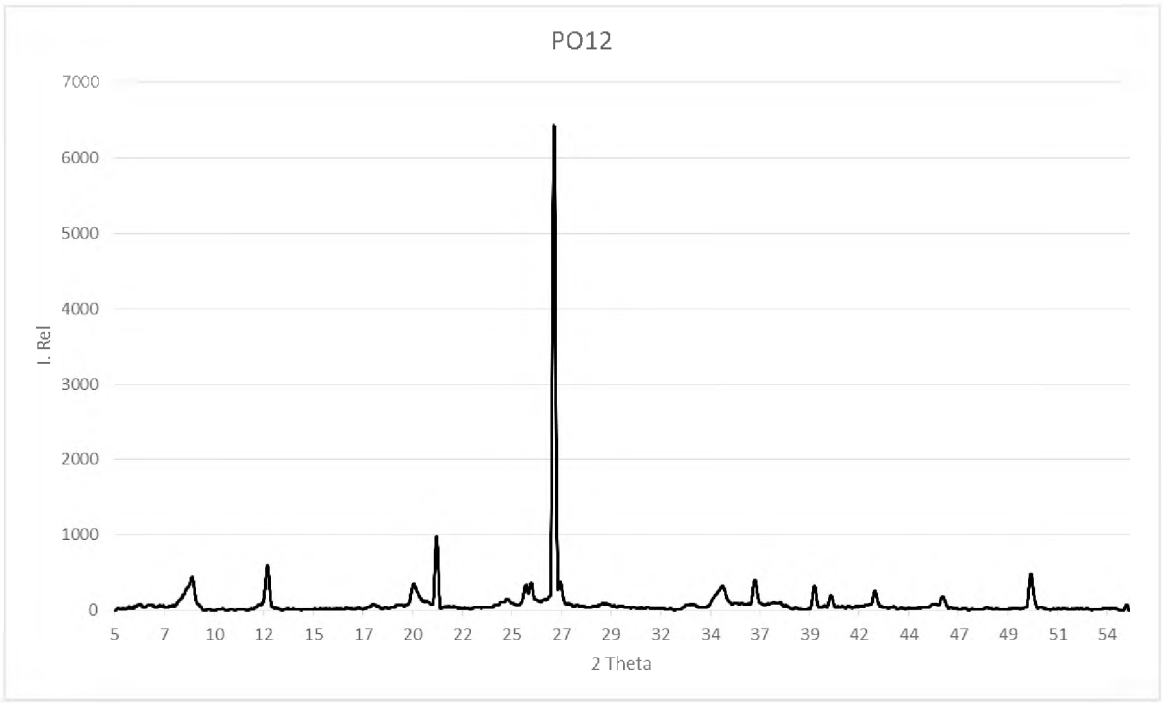
PO12
7000
6000
5000
4000
3000
2000
1000
0
I. Rel
5 7 10 12 15 17 20 22 25 27 29 32 34 37 39 42 44 47 49 51 54
2 Theta

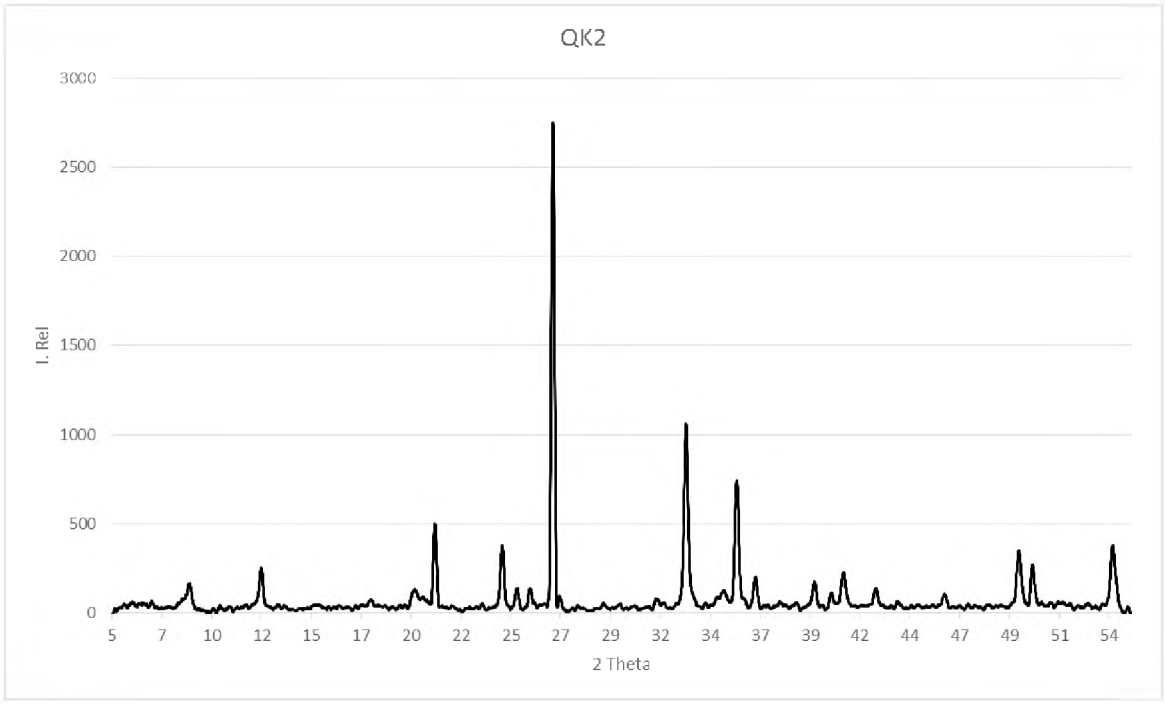
QK2
3000
2500
2000
1500
1000
500
0
I. Rel
5 7 10 12 15 17 20 22 25 27 29 32 34 37 39 42 44 47 49 51 54
2 Theta

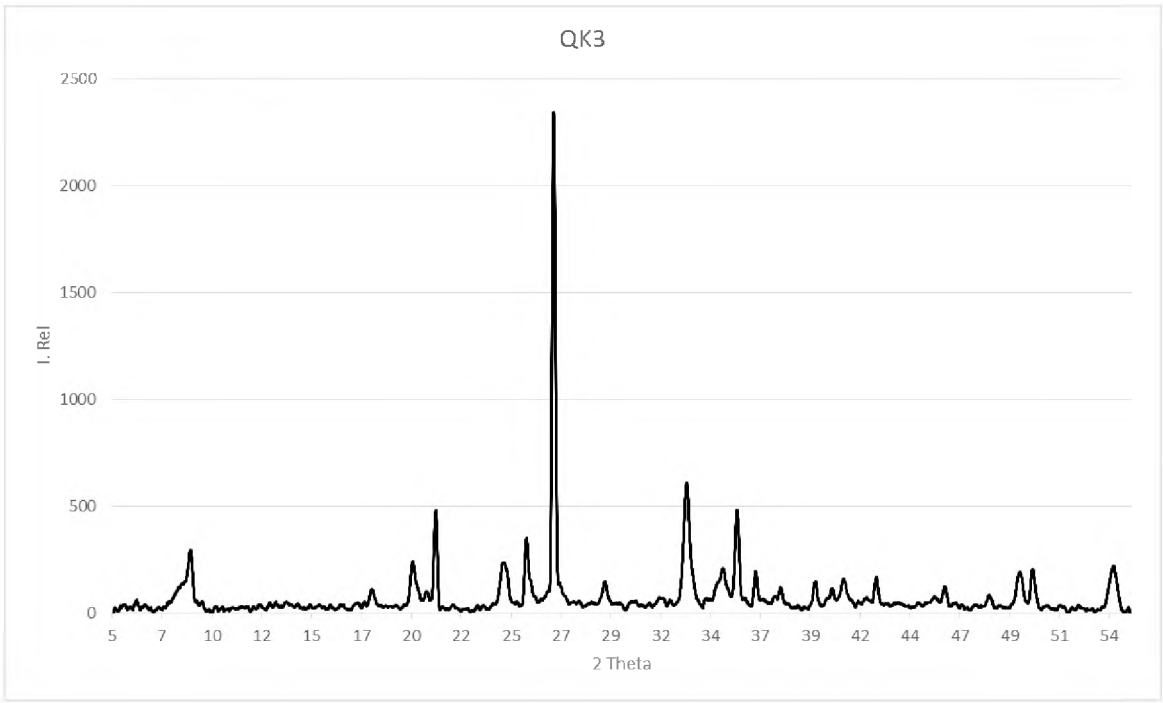
QK3
2500
2000
1500
1000
500
0
I. Rel
5 7 10 12 15 17 20 22 25 27 29 32 34 37 39 42 44 47 49 51 54
2 Theta

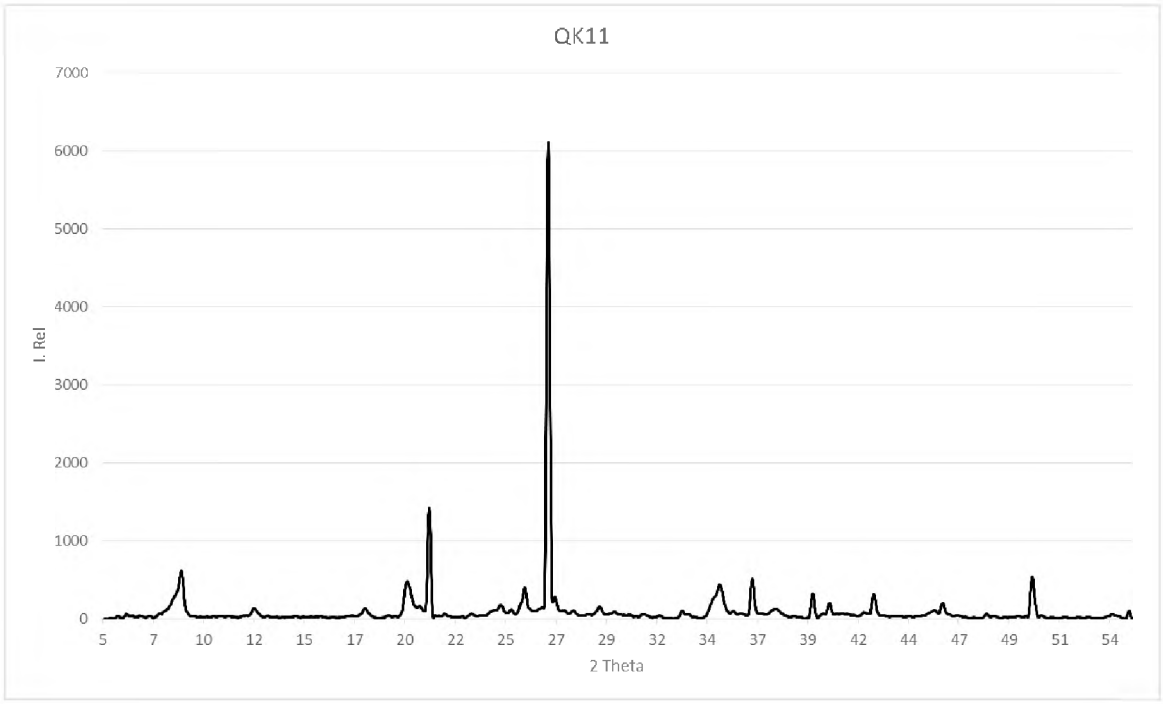
QK11
7000
6000
5000
4000
3000
2000
1000
0
I. Rel
5 7 10 12 15 17 20 22 25 27 29 32 34 37 39 42 44 47 49 51 54
2 Theta

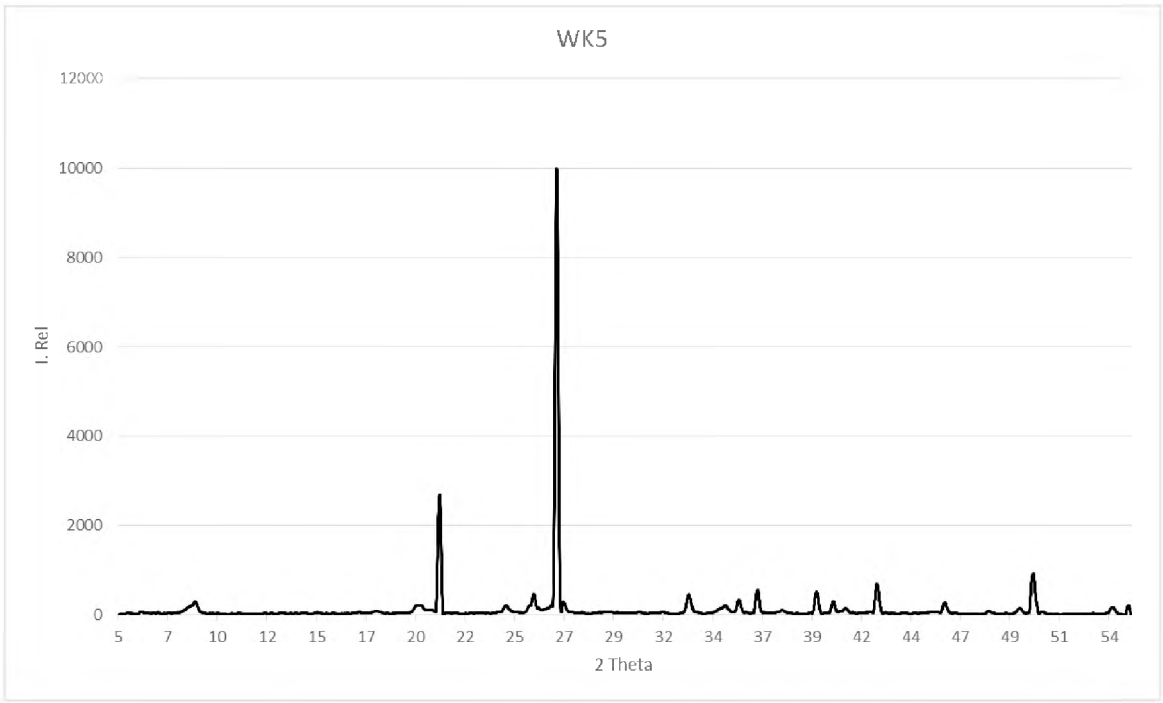
WK5
12000
10000
8000
6000
4000
2000
0
I. Rel
5 7 10 12 15 17 20 22 25 27 29 32 34 37 39 42 44 47 49 51 54
2 Theta

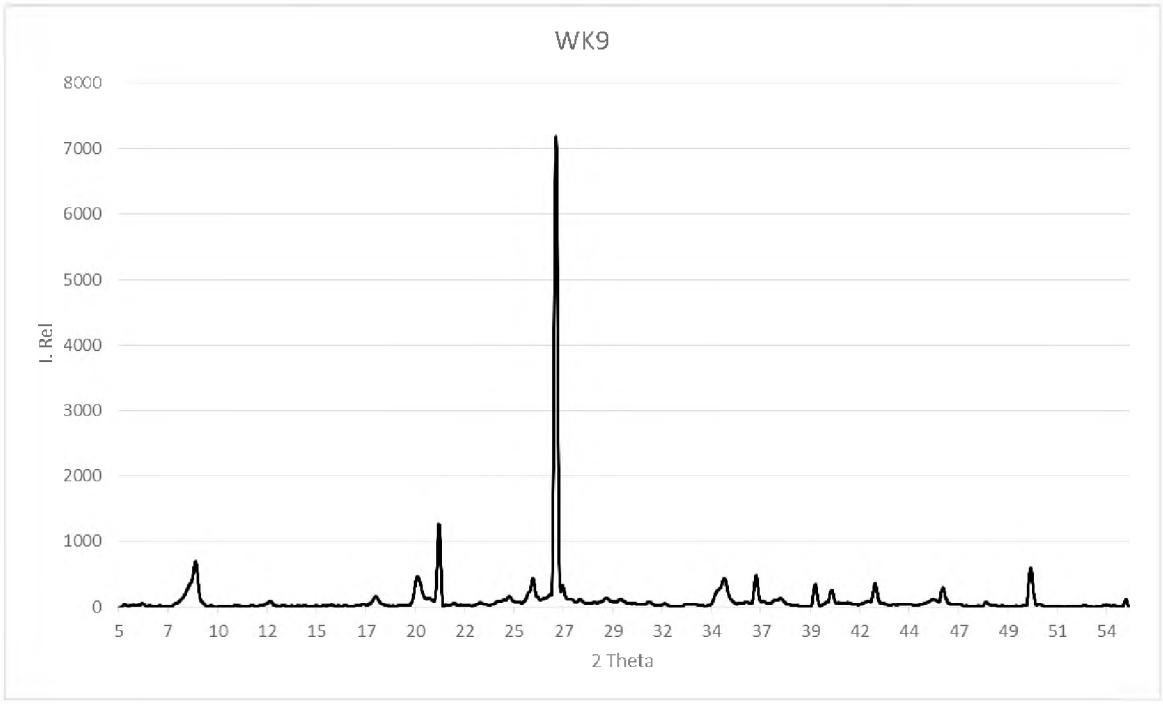
WK9
8000
7000
6000
5000
4000
3000
2000
1000
0
I. Rel
5 7 10 12 15 17 20 22 25 27 29 32 34 37 39 42 44 47 49 51 54
2 Theta

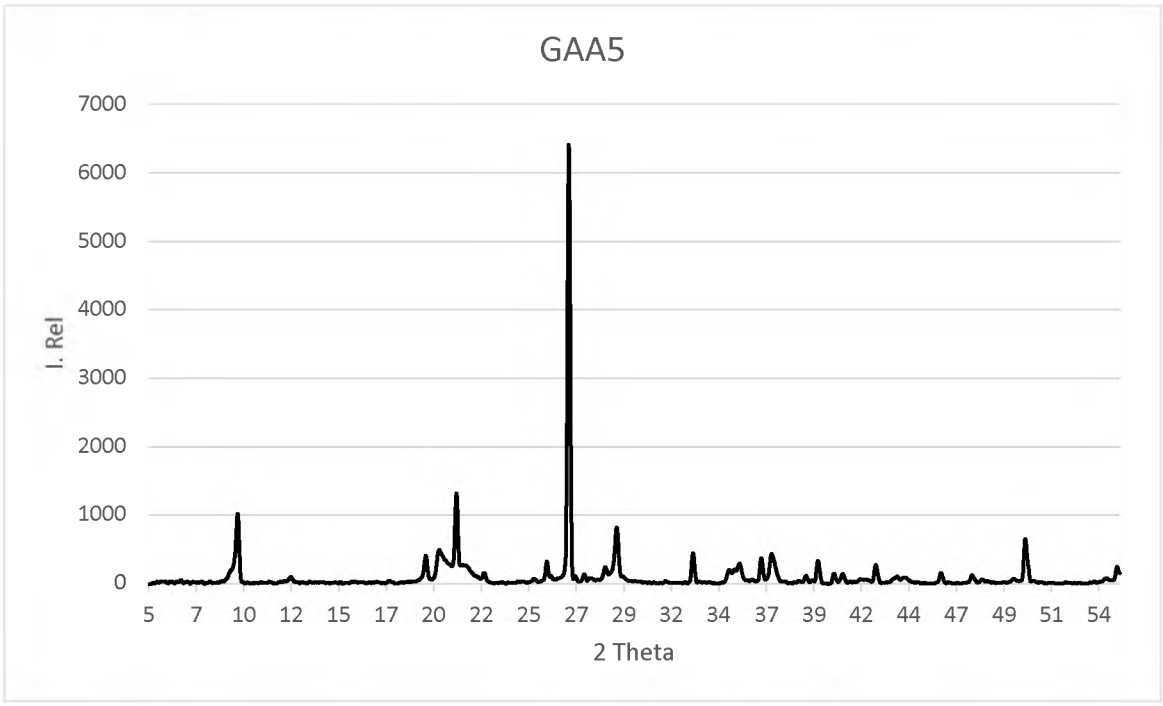
GAA5
I. Rel
7000
6000
5000
4000
3000
2000
1000
0
5 7 10 12 15 17 20 22 25 27 29 32 34 37 39 42 44 47 49 51 54
2 Theta

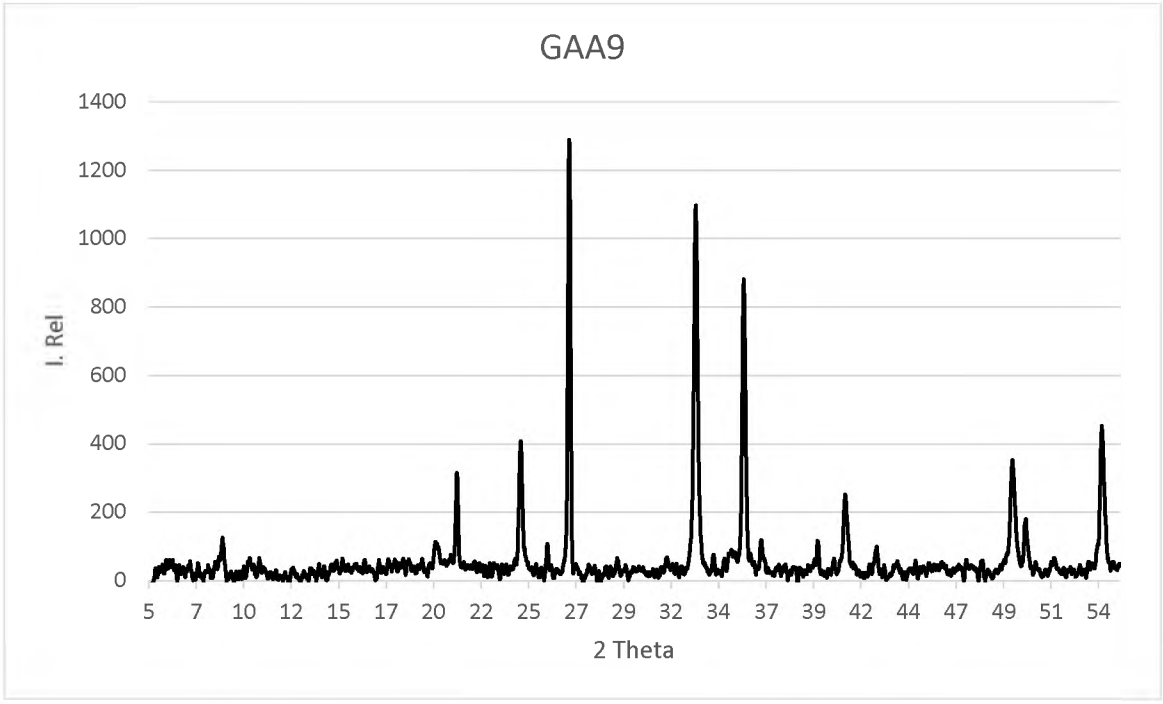
GAA9
I. Rel
1400
1200
1000
800
600
400
200
0
5 7 10 12 15 17 20 22 25 27 29 32 34 37 39 42 44 47 49 51 54
2 Theta

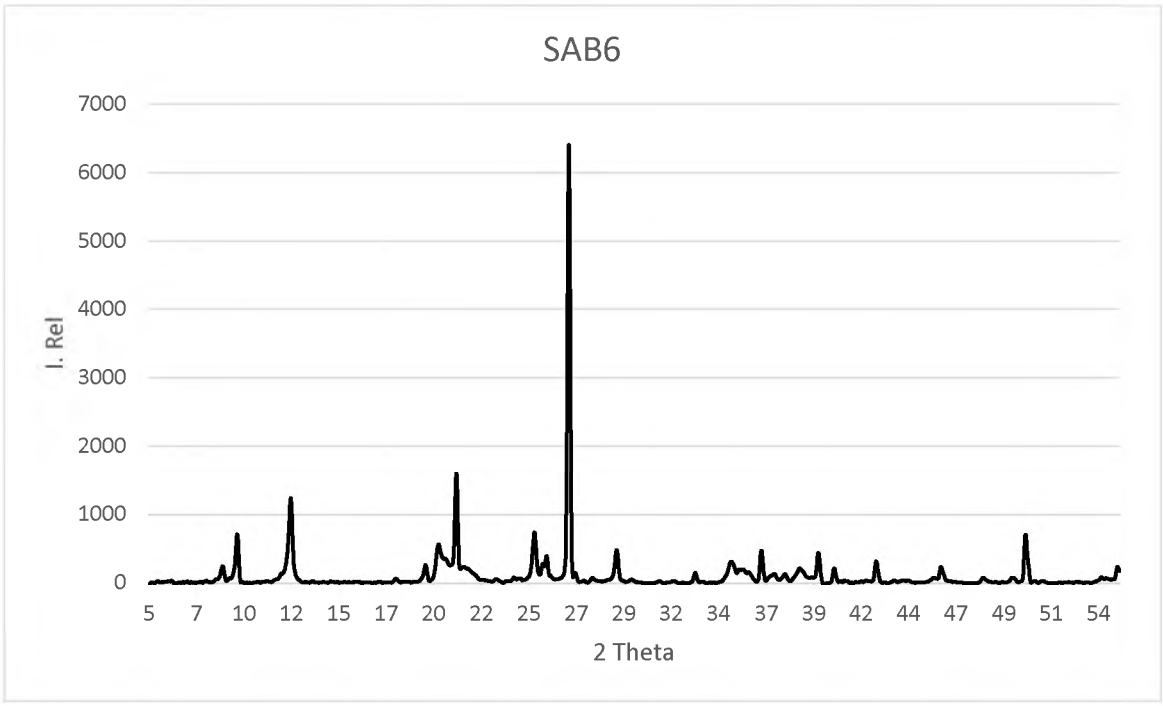
SAB6
7000
6000
5000
4000
3000
2000
1000
0
I. Rel
5 7 10 12 15 17 20 22 25 27 29 32 34 37 39 42 44 47 49 51 54
2 Theta

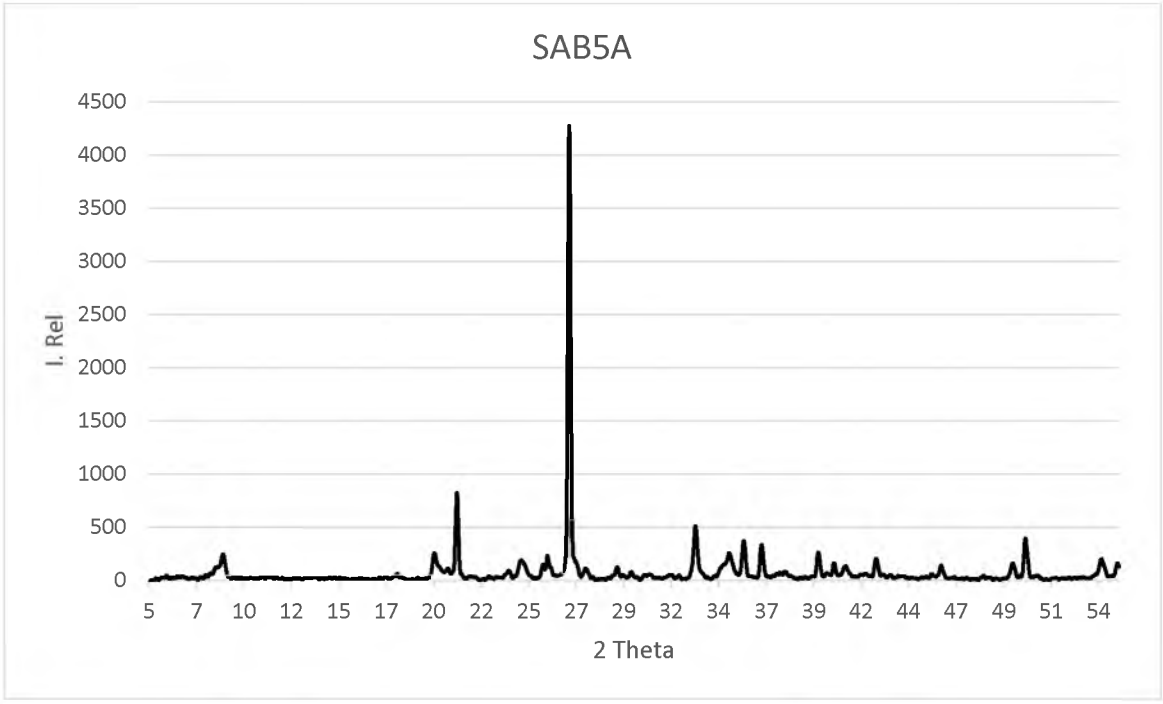
SAB5A
4500
4000
3500
3000
2500
2000
1500
1000
500
0
I. Rel
5 7 10 12 15 17 20 22 25 27 29 32 34 37 39 42 44 47 49 51 54
2 Theta

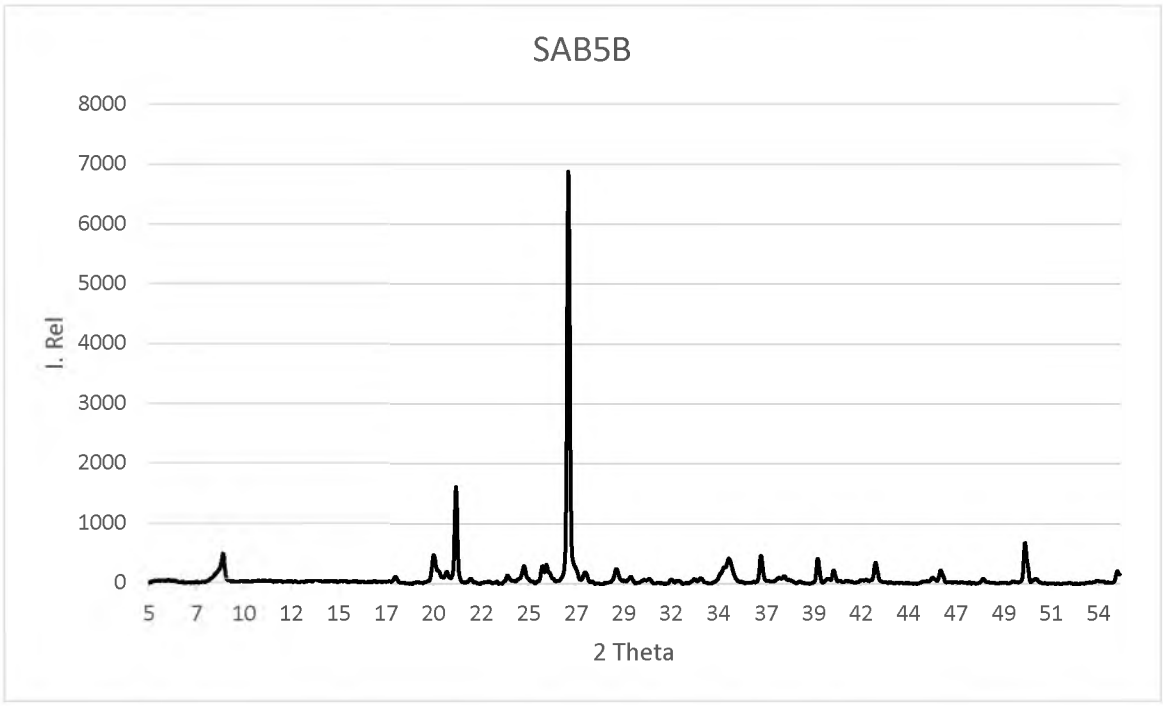
SAB5B
8000
7000
6000
5000
4000
3000
2000
1000
0
I. Rel
5 7 10 12 15 17 20 22 25 27 29 32 34 37 39 42 44 47 49 51 54
2 Theta

APPENDIX D WDS ELEMENT MAP

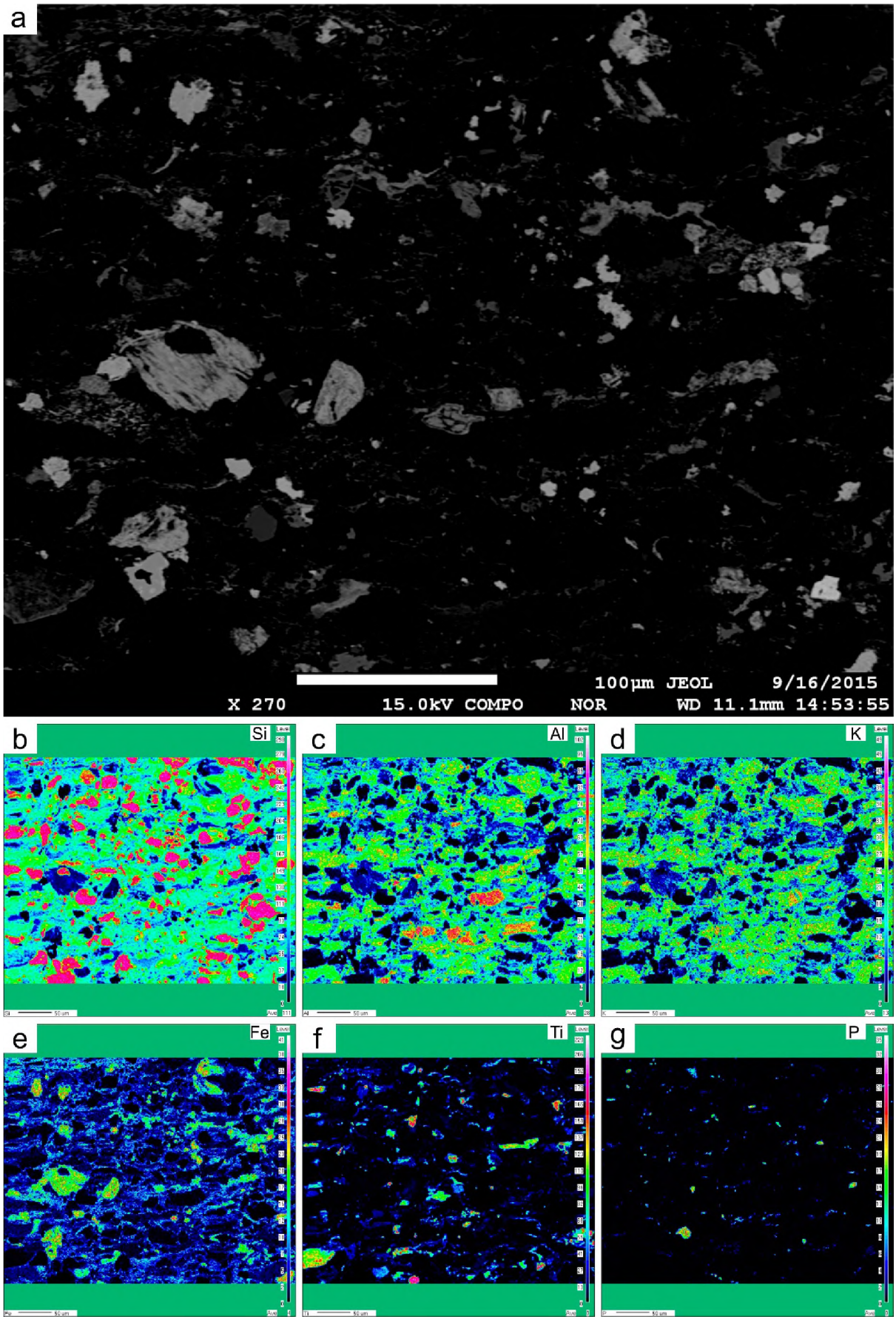

APPENDIX E MICROBIAL MATS